Light Management in Non-Hermitian Systems

A thesis submitted for the degree of Erasmus Mundus Doctorate in

Photonics Engineering, Nanophotonics and Biophotonics

Waqas Waseem Ahmed

Universitat Politècnica de Catalunya (UPC), Spain

European Laboratory for Nonlinear Spectroscopy (LENS), Italy

Directors:

Prof. Ramon Herrero Simon

Prof. Muriel Botey i Cumella

Prof. Diederik S. Wiersma

Prof. Kestutis Staliunas

March, 2018

Acknowledgements

I am deeply grateful to my advisors Ramon Herrero, Muriel Botey, Kestutis Staliunas and Diederik Wiersma for their endless support, guidance, and suggestions throughout my PhD. I sincerely thank to Ramon and Muriel for friendly scientific discussions, care and answering my silly questions with patience. Special thanks go to Kestas for sharing innovative ideas with me and explaining me how to handle difficult problems systematically. All of you inspired me a lot to work on novel ideas which eventually led me to complete my PhD.

I am also thankful to my friend Dr. Shubham Kumar for helping me at the beginning of my PhD. I also want to thank DONLL group colleagues and friends; Carlos, Jordi, Bingxia, Judith, Donatas, Hosseim, Pablo, Dario, Maria, Ignacio, Auro, Julio, Yu-Chieh and also LENS colleagues; Joyce, Lorenzo, Sara, Francesco, Dmitry, and Fabrizio. It was a wonderful experience to have a company of you which make my PhD journey enjoyable and worthwhile.

I am also thankful to my friends Muhammad Fahad Zia, Khaqan Majeed, and Tri Bagus Susilo for proofreading my thesis and providing me suggestions to improve the presentation of the thesis.

I would like to thank my previous professors Dr. Mohammad Abdulaziz Husain Alsunaidi and Dr. Husain Masoudi for teaching me the basics of

photonics which ultimately led me to pursue my career in photonics and also indirectly helped me to complete my PhD.

Lastly, I would like to thank my beloved parents, to whom this thesis is dedicated to, and my siblings for their encouragement, patience and unconditional support during my PhD journey.

Contents

Preface

The quest for new artificial structures and materials uncovers new light-matter interactions and intriguing physical phenomena. Since the late 80's purely dielectric materials have been structured, at the wavelength-scale, to develop photonic crystals and photonic crystal fibers. Recently, also the modulation of gain and losses came into play. The new platform based on complex refractive index materials, combining index and gain-loss modulations, opens the door towards new physical concepts and novel applications. One of these fascinating new insights is the realization of classical analogues of quantum systems described by non-Hermitian Hamiltonians, where the complex refractive index plays the role of a complex optical potential. Thus, by carefully combining the real and imaginary parts of the refractive index; it is possible to observe unusual features that cannot be attained in classical Hermitian systems. In particular, non-Hermitian PT-symmetric systems, invariant under the parity and time-reversal symmetries, may support unidirectional mode coupling which is at the basis of novel ideas and applications such as unidirectional invisibility, single mode microlasers or super-sensitive sensors just to name a few. Non-Hermitian photonics has overturned the conventional negative perception of losses and offers new possibilities to utilize the gain and loss for steering optical processes.

The aim of this thesis is to provide new insights into the wave dynamics in this new artificial complex media since a flexible wave control may be

essential to design novel technological devices. The work has a double scope: to propose and develop new concepts in fundamental photonic science; and to provide technological studies for direct applications in actual and ubiquitous devices such as broad area semiconductor lasers. In this sense, the main contribution is a novel approach to manipulate the light flow using non-Hermitian systems for light localization and enhancement, and for the control of the flow of light following arbitrary vector fields and corresponding applications to photonic devices. The thesis is organized as follows:

In Chapter 1, we provide a general overview of non-Hermitian systems holding PT-symmetry. The chapter is devoted to basic concepts of non-Hermitian dynamics in complex periodic systems.

In Chapter 2, we propose the new fundamental concept of local PT-symmetry for the simultaneous field localization and enhancement at a selected point or area. The chapter explains how the asymmetric coupling of inward /outward propagating waves in a PT-axisymmetric configuration may lead to an extraordinary field concentration or homogenization, respectively. We start by analyzing a one-dimensional (1D) system consisting of the combination of two periodic PT-symmetric domains, holding PT-symmetry only locally. Following this 1D local PT-symmetry scheme, a novel 2D PT-axisymmetric configuration is proposed to obtain highly localized fields in real physical systems. In the last part of the chapter, we also discuss the possibility to realize an analogous localization based on axial inward coupling using quasi-periodic systems with global PT-symmetry.

In Chapter 3, we extend and generalize the idea of local PT-symmetry to design systems able to control the flow of light. The design of such 2D (or

higher dimensional) complex structured material for any arbitrary vector field and desired topology is based on a local Hilbert transform. That is to say, the mathematical framework to design such complex optical potentials, either in 1D and 2D, is developed as a modification of the conventional Hilbert transform which relates the two quadratures (real and imaginary parts) of the spatial distribution of the refractive index. The theory of such directionality field is tested on random, periodic, quasi-periodic and localized patterns to generate arbitrary field flows in the form of a sink, vortices or circular channel flows, both in linear and nonlinear systems.

In Chapter 4, we investigate non-Hermitian structures for technological applications. Firstly, we consider 2D periodic lattices, with simultaneous transverse and longitudinal PT-symmetry. We show that such optical potentials may be intended to obtain self-collimated beams, useful for example in integrated optics. Secondly, we propose different schemes of index and gain/loss modulations to enhance the stability of broad area semiconductor (BAS) devices. We show how: (i) the introduction of spatiotemporal modulation on the pump of vertical-external-cavity surface-emitting lasers (VECSELs) with a simple flat mirror configuration, may stabilize its emission; (ii) in phase modulations of index and gain-loss profiles stabilizes the emission from BAS lasers and amplifiers, a proposal relying on the suppression of modulation instabilities using dispersion management; (iii) PT-axisymmetry applied either to BAS lasers or VCSELs renders these lasers into bright and narrow laser sources.

Finally, Chapter 5 presents the summary and conclusions of the thesis along with the discussion on future perspectives to extend this work.

Chapter 1
Introduction

This chapter presents an introduction, background, and overview of the basic underlying concepts of non-Hermitian systems. Such systems were first introduced as a theoretical curiosity in the field of Quantum Mechanics, however, found feasible classical realizations principally in optics, leading to a novel playground for unexpected effects with applications in photonic technologies. The chapter describes the notion of Parity-Time (PT-) symmetry, showing how non-Hermitian systems holding PT-symmetry may have real eigenvalues, hence a real spectrum. The unidirectional behavior of non-Hermitian systems under PT-symmetry is overviewed by analyzing the wave and beam propagation in such complex potentials. The similarities and differences between the spatial dynamics of Photonic Crystals (PhCs) and Gain-Loss Modulated Materials (GLMMs) are discussed in relation to non-Hermitian systems. A basic theoretical framework is provided to study the dispersion and transmission-reflection properties of one-dimensional (1D) PhCs, GLMMs and PT-symmetric materials in a simpler manner. Finally, the paraxial model that is mostly used throughout the thesis to verify the proposed fundamental theories and predictions is also discussed. Besides, this chapter presents the analytical and numerical approaches employed to understand the dynamics of non-Hermitian systems.

1.1 Background

Loss-immune systems are a dream for laser physicists and technologists, especially for those working in optics and photonics. Nobody can deny the significance of gain media due to its importance in amplification of optical signals and many other features. However, on the other hand, losses are always treated and neglected like a '*disobedient child at home*' for creating problems in any device. This may be the reason why fewer efforts have been devoted so far to explore its potential applications in literature. Nowadays, researchers have managed to minimize losses in optical systems to a certain extent through different elegant ways, but it is still almost impossible to get rid of it entirely. This gives rise to some questions: is it possible to tame losses to increase the system efficiency? or how to treat losses in a clever way to get some benefits? Such suggestions may be surprising but instigate more curiosity. How can one expect benefits from losses avoiding its intrinsic detrimental nature? Can gain and losses be manipulated simultaneously as useful ingredients in optical devices? The answers to these questions are hidden in a new class of structured materials named *PT-symmetric systems*, which belong to the more general class of non-Hermitian systems. For a long time, it was commonly believed that non-Hermitian systems always played a destructive role in wave control due to an inherent dissipation of energy. However, our views about the role of losses in light transport drastically changed since the discovery of PT-symmetric systems. Such systems provide new physical mechanisms to manipulate the amplification and absorption of light, thus uncovering novel intriguing features and functionalities.

Historically, non-Hermitian systems attracted attention in the 1990s, when Carl Bender and his colleagues challenged the well-known axiom of Quantum Mechanics saying that Hermicity is not necessary to observe real

eigenvalue spectra [Ben98, Ben99]. They showed that a wide class of non-Hermitian Hamiltonians may still provide real eigenvalues, and therefore describe physical systems when they hold the PT-symmetry conditions. Moreover, they also discovered that PT-symmetric Hamiltonians exhibit a phase transition from real to complex eigenvalues which can be attributed to the spontaneous PT-symmetry breaking of the system eigenfunctions. At one side of this phase transition, the system behaves as a conservative one (mode locking …) and, on the other side, as a dissipative one (oscillations etc). This discovery encouraged many researchers to revisit the Hermitian theory of Quantum Mechanics [Ahm01, Bag01]. Mostafazadeh pointed out that pseudo-Hermicity is the responsible for the real spectra of PT-symmetric Hamiltonians, which belong to a specific class of the general family of pseudo-Hermitian Hamiltonians [Mos02]. Since then, PT-symmetry attracted a significant attention in the field of Quantum Mechanics, and a new mathematical framework was developed for the description of non-Hermitian Hamiltonians [Ben02, Wei03, Mos3, Hei04, Ben05, Ben07]. However, Quantum Mechanics was not able to provide any evidence of PT-symmetry in practical systems. Therefore, the idea of PT-symmetry initially proposed in Quantum Mechanics theory remained purely speculative for many years due to lack of an experimental proof. In this situation, Christodoulides and his co-workers suggested that the concept of PT-symmetry can be physically realized in optical systems with a complex refractive index [Gan07, Mak08]. This suggestion paved the way for the first experimental observation of spontaneous PT-symmetry breaking (where the non-Hermitian system abruptly changes its eigenspectrum from real to complex), in a passive waveguide configuration [Guo09]. Later, PT-symmetry was experimentally observed in active coupled optical waveguides with balanced gain and loss [Rut10]. In this way, optics provided a fertile ground to realize PT-symmetry, leading to the

new research line of non-Hermitian Photonics. The field of non-Hermitian Photonics has rapidly grown due to interesting light-matter interactions that have no analogy in conventional Hermitian structures [Fen17]. There has been a fertile series of research activities to understand non-Hermitian dynamics in optical systems [Kon16, Gan18]. Besides, PT-symmetry has been recently explored in different physical systems such as electronics [Sch11, Sch12], plasmonics [Ben11], microwave [Bit12], mechanics [Ben13], acoustics [Zhu14, Fle15], Bose-condensates [Gra12], and optomechanics [Lu15, Xu16]. The general area of PT-symmetry has opened new avenues for further investigations, which leads to several predictions in many linear and nonlinear systems, e.g. double refraction [Mak08], optical solitons [Mus08, Wim15], Bloch oscillations [Lon09], spectral singularities [Mos09,Ram14], non-linearity induced PT-symmetry breaking [Suk10, Lum13], power oscillations and phase singularities [Mak10], PT-symmetric wave chaos [Wes10], perfect optical absorption [Lon10, Cho11], unidirectional invisibility [Lin11], Talbot effect [Ram12a], defect states [Reg13], loss-induced suppression and revival of lasing [Pen14a], thresholdless PT-symmetry breaking [Ge14], resonant mode conversion [Vys14], optical tunneling [Sav14], asymmetric chirality [Tur15], directional lasing [Pen16], polarization mode conversion [Has17], etc. Most importantly, the presence of the exceptional point (where complex eigenvalues and eigenfunctions merge) in PT-symmetric systems have special significance for many technological applications ranging from non-reciprocal devices [Pen14b, Cha14] to ultra-sensitive measurement devices [Li16, Liu16].

In the last decade, non-Hermitian systems particularly those being PT-symmetric, have been extensively studied in optics for nontrivial spatial effects. Most of the initially reported PT-symmetric studies focused on 1D

systems, where PT-symmetry was considered on a global scale. The global PT-symmetry in 1D systems rapidly became a well-established theory for unidirectional flows. However, the control of unidirectional flows in higher dimensional PT-symmetric systems remained unexplored –a research gap in PT-symmetric studies. To fill this gap, we introduced the concept of local PT-symmetry for the first time. The work presented here mainly focuses on local PT-symmetry in two-dimensional (2D) systems, to provide unidirectionality in designed directions, for manipulation of the field flows. Therefore, the proposed local PT-symmetry provides a more precise control to design a flow configuration on demand. In addition, this thesis also addresses some practical realizations of non-Hermitian structures to obtain self-collimated and high-quality beams in integrated photonic devices.

1.2 Introduction to Parity-Time (PT-) symmetry

Parity (P) and Time-reversal (T) symmetries are fundamental symmetry transformations in Physics. Mathematically, the P symmetry reverses the position, and therefore the momentum. On the other hand, the T symmetry reverses the time.

In Quantum Mechanics, the T operator also changes the sign of the imaginary unit i, therefore (and since the momentum operator is: $p = -ih\,\partial/\partial x$) the P, T, and PT operator perform the following transformations:

$$P\colon\ r \to -r, p \to -p \tag{1.1a}$$

$$T\colon\ \ i \to -i, r \to r, p \to -p \tag{1.1b}$$

$$PT\colon\ \ i \to -i, r \to -r\,, p \to -p \tag{1.1c}$$

To understand the parity and time symmetry operations, we consider a simple Hamiltonian (H) expressed in the form of position and momentum operator as $H = p^2 + V(r)$, where $V(r)$ represents a potential. For a real-valued potential, this Hamiltonian is Hermitic ($H = H^{\dagger}$, where † denotes the adjoint, conjugate transpose, operation) and holds entirely real eigenvalues. However, Carl Bender et al. discovered that the Hermitian condition is too restrictive, and also non-Hermitian Hamiltonians may give the real eigenvalue by full-filling the weaker condition of PT-symmetry. The PT-symmetric condition on the Hamiltonian ($HPT = PTH$) requires that the potential satisfies the relation: $V(r) = V^{\star}(-r)$ [Ben98]. This implies that the real and imaginary parts of the complex potential be even and odd function of space, respectively: Re[$V(r)$]=Re[$V(-r)$] and Im[$V(r)$]=-Im[$V(-r)$]. This leads to a new class of PT-Hamiltonians which are non-Hermitian but, eventually show an entirely real spectrum.

It is important to mention that the spectrum of all PT-symmetric Hamiltonian is not necessarily real. However, the Hermicity condition may be relaxed. For a potential in the form: $V(r)$=Re[$V(r)$]+αIm[$V(r)$] being α ($\alpha \geq 0$) a dimensionless parameter, there is a critical (exceptional) point α_c so that for $\alpha \leq \alpha_c$ the spectrum becomes entirely real. For $\alpha = \alpha_c$ gain and loss are balanced; this corresponds to PT-transition phase. Above this exceptional point, $\alpha > \alpha_c$, the spectrum is formed of pairs of complex conjugate eigenvalues. This situation belongs to PT-broken phase. We can summarize that a PT-symmetric system shows two possible regimes separated by the PT-transition (or exceptional) point: (i) *unbroken PT regime* showing the entire real eigenvalues, and (ii) *broken PT regime* showing complex eigenvalues.

1.2.1 PT-symmetry in Photonics

The concept of PT-symmetry, requiring complex potentials, can be realized with complex dielectric permittivity (or refractive index) profiles in the optical domain. It can be understood by the analogy between the well-known Helmholtz equation and the Schrödinger equation for diffractive light propagation. We start with wave equation derived from Maxwell´s equations for a monochromatic field:

$$\nabla^2 E(r,t) - \frac{\varepsilon}{c^2}\frac{\partial^2 E(r,t)}{\partial t^2} \tag{1.2}$$

where ∇^2 is the Laplacian operator and ε is the dielectric permittivity of the medium. It is not trivial to solve such a non-stationary equation analytically. To simplify our problem, we consider temporally-harmonic monochromatic solutions in the form: $E(r,t) = E(r)e^{i\omega t}$ where $E(r)$ is the complex amplitude, and ω is the angular frequency. This eventually eliminates the time derivative term in Eq. 1.2 and we obtain a scalar Helmholtz equation:

$$\nabla^2 E(r) + \varepsilon(r) k_0^2 E(r) = 0 \tag{1.3}$$

where $k_0 = \omega/c$, is the wave number of frequency ω.

The scalar Helmholtz equation is the classical analog of the stationary Schrödinger equation in Quantum Mechanics [Zya14], written as:

$$\nabla^2 \psi_k(r) - \frac{2m(V(r) - E_k)}{\hbar^2}\psi_k(r) \tag{1.4}$$

Indeed, both equations become identical under substitution: $\psi_k(r) \rightarrow E(r)$ $(V(r) - E_k) \rightarrow \varepsilon(r)k_0^2$, and $-2m/\hbar^2 \rightarrow 1$. The PT-symmetry condition for a quantum mechanical system, requires that the potential fulfils: $V(r) = V^\star(-r)$. Based on equivalence between the potential in quantum mechanics and the dielectric permittivity in optics, we can say that the complex permittivity, $\varepsilon(r)$, (or complex refractive index, $n(r)$) of the optical medium plays the role of a complex optical potential [Gan07, Mak08]. Therefore, we require:

$$\varepsilon(r) = \varepsilon^*(-r) \tag{1.5}$$

Generally, the dielectric permittivity ($\varepsilon = n^2$) in a modulated system may be expressed as $\varepsilon(r) = \varepsilon_b + \Delta\varepsilon(r)$, where $\Delta\varepsilon(r)$ is the modulation imposed on background permittivity, ε_b. For a weak modulation of the dielectric permittivity index, i.e. $\Delta\varepsilon(r) \ll \varepsilon_b$, this relation holds: $\Delta\varepsilon(r) \propto \Delta n(r)$. Equation (1.5) simply implies that the real part of the refractive index (or dielectric permittivity) is an even function and the imaginary part of the refractive index (or dielectric permittivity) is an odd function of space expressed as:

$$n_{Re}(r) = n_{Re}(-r); \quad n_{Im}(r) = -n_{Im}(-r) \tag{1.6}$$

Thus, PT-symmetric structures can be realized in optics using symmetric and anti-symmetric profiles for real and imaginary parts of refractive index, respectively. There are several studies on periodic [Mus08, Mak10, Lin11, Mak11] and non-periodic [Kla08, Rut10] PT-symmetric structures. Figure 1.1 illustrates an example of non-periodic and periodic PT-symmetric potential profiles. However, such potentials with symmetric index and anti-symmetric gain-loss profiles can be designed in a variety of ways.

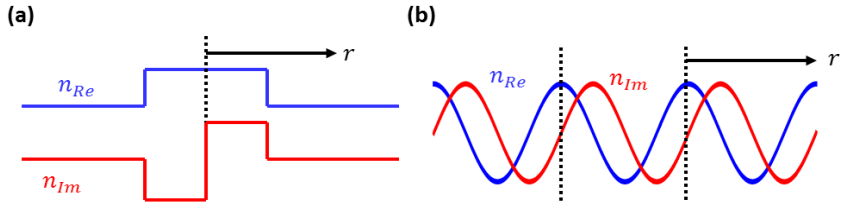

Figure 1.1. Optical PT-symmetric potentials (a) non-periodic (b) periodic

1.2.2 Development in PT-symmetric Photonics

PT-symmetric quantum mechanics has attracted a huge theoretical interest since the pioneering work of Carl Bender, while experimental implementations remain very challenging in practical systems. The isomorphism between the Schrödinger equation and the paraxial equation of diffraction has stimulated theoretical and experimental efforts to realize PT-symmetry in the optical framework. The experimental realization of PT-symmetric systems requires set-ups of at least two optical components, i.e. one with absorption and other one either active (optically pumped) or passive (with losses). In this section, we present a brief overview of the technological advancements in the emerging field of PT-symmetric optics. In 2009, Guo et al. reported the first experimental observation of passive PT-symmetry breaking in optics [Guo09]. Following this study, Ruter et al. experimentally demonstrated the PT-symmetry on a system of actively coupled optical waveguides (LiNbO3 crystal) with balanced gain and loss profiles [Rut10]. In this experiment, intrinsic loss and gain were induced through photorefractive two-wave mixing, well-designed to observe the non-symmetric beam dynamics. In 2012, Regensburger et al. proposed a PT-optical fiber network and experimentally demonstrated the unidirectional light transmission in the temporal domain [Reg12]. Feng et al. proposed a passive PT-symmetric metamaterial on a Si-on-insulator

platform, and experimentally demonstrated what they referred as unidirectional invisibility [Fen13]. Until 2013, most of the experimental observations of PT-symmetry were limited to non-resonant structures like waveguide systems. However, many theoretically predicted phenomena such as non-symmetric light transmission [Ram10, Yin13], simultaneous coherent perfect absorption and lasing [Cho10, Lon10, Cho11], and exceptional points in laser systems [Lie12] could only be realized in resonant structures exhibiting PT-symmetry. In this scenario, scientists invested some efforts for the experimental realization of PT-symmetry breaking in resonant structures like whispering-gallery microcavities for on-chip optical communications [Pen14b]. Chang et al. experimentally observed an on-chip optical isolation in whispering-gallery microcavities by breaking time-reversal symmetry with a gain-saturated nonlinearity [Cha14]. In 2014, Feng et al. proposed a first PT-symmetric laser in which gain-loss is manipulated by periodic Cr/Ge structure, see Fig. 1.2(e) [Fen14]. Such synthetic laser exhibits a single mode operation in a PT-broken phase where lasing and absorbing modes are simultaneously present. Hodaei et al. used the same concept of PT-symmetry breaking for a mode selection mechanism and proposed a PT-symmetric microring laser which allows to select a single longitudinal mode depending on the amount of loss and gain in the system [Hod14]. In short, many experimental studies have been performed to realize PT-symmetric structures ranging from mode-selective lasers, saturable absorbers, optical isolators, optical modulators, coherent perfect absorbers, optical switches, optical diodes, optical microcavities and resonators, sensors to PT-symmetric Bragg gratings for different applications. The pioneering work of experimentally demonstrated optical PT-symmetric systems is summarized in Fig. 1.2.

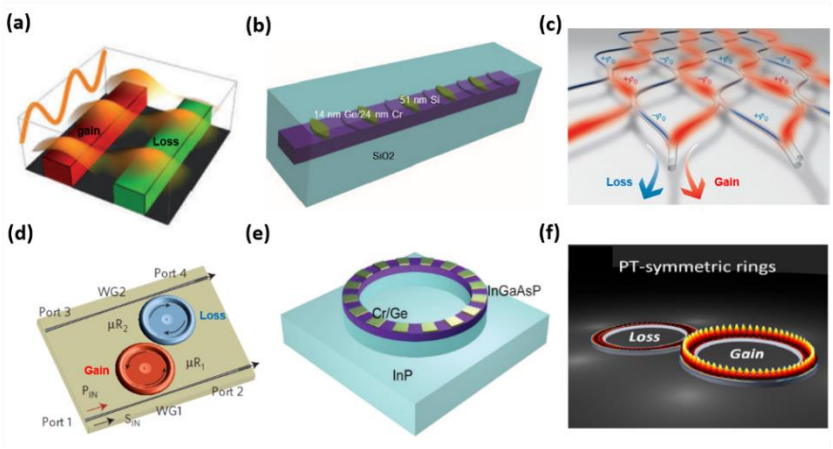

Figure 1.2. Experimentally demonstrated optical PT-symmetric systems (a) PT-symmetric coupled waveguide system [Kot10] (b) PT-symmetric passive metamaterial [Fen12] (c) PT-symmetric fiber network [Reg12] (d) PT-symmetric coupled whispering gallery microresonators [Cha14] (e,f) PT-symmetric microring lasers [Fen14, Hod14].

1.3 Wave propagation in Complex periodic media

In the previous section, we have seen that PT-symmetric structures can be realized with complex optical potentials which can be simply described by a complex refractive index, i.e. $n(r) = n_{Re} + in_{Im}$ where n_{Re} and n_{Im} denote the real and imaginary parts of the refractive index. Such complex potentials define the general class of non-Hermitian media which do not warrant the conservation of energy and hence have complex eigenvalues. The eigenvalues of non-Hermitian potentials become real by carefully designing the gain and loss in the systems, only for PT-symmetric systems. In this thesis, we mainly focus on periodic non-Hermitian systems where both the real and imaginary part of the refractive index are periodic in space. More precisely, they belong to two broader categories, i.e. Photonic Crystals (PhCs) and Gain-Loss Modulated Materials (GLMMs). Periodic

PT-symmetric systems can be formed by the combination of PhCs and GLMMs, holding parity and time reversal symmetry conditions. In the next section, we provide a theoretical background to understand the effects of such periodicity in complex optical potentials. In particular, we study wave and beam propagation in complex periodic potentials to understand the dynamics of non-Hermitian systems with PT-symmetry. Moreover, the dispersion properties of PhCs and GLMMs are also analyzed using the Plane Wave Expansion (PWE) method.

1.3.1 Wave propagation in Photonic Crystals

Photonic Crystals are periodic materials where the real-valued refractive index is spatially modulated in a periodic manner on the wavelength scale. The refractive index variation can be realized in one, two or three dimensions which define the dimensionality of PhCs. The most interesting feature of the PhCs is the existence of photonic bandgaps (PBGs) which appear due to the periodicity of the structure [Yab91]. These PBGs are bands of forbidden frequency for which light cannot propagate through ideal (infinitely long) structures. PBGs have technological importance for different applications, e.g. light localization in defects [Mea91], slow light [Ger05, Bab08], negative refraction [Cub03, Not10], spatial filtering [Ser09, Mai10, Mai15], self-collimation [Kos99, Sta06a], flat lensing [Par03], etc. To understand wave propagation in PhCs, we first consider a simple 1D periodic structure, as the one shown in Fig. 1.3. The simplest structure consists of two layers of different materials of the same thickness, $d_1 = d_2 = d/2$, with high $(n_1 = n_1^{Re} + 0i)$ and low $(n_2 = n_2^{Re} + 0i)$ refractive indices, periodically repeating in space over the period, d. However, the thicknesses of material layers may not necessarily be equal but can be different, depending on the geometry of PhC structure.

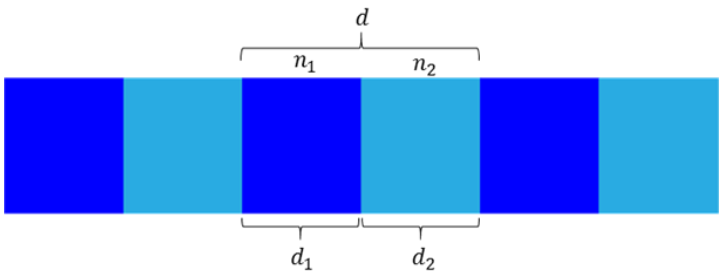

Figure 1.3. Schematic illustration of 1D PhC made of two different materials of same thickness, $d_1 = d_2 = d/2$, with refractive indices n_1 and n_2, respectively. The periodicity of PhC is $d = 2\pi/q$, where q is the lattice wavevector.

First, we determine the dispersion properties of the infinite PhC structure using the PWE method. This method relies on the Floquet-Bloch theorem which expands the periodic magnetic (or equivalently, electric) fields and dielectric permittivity functions into a Fourier series of harmonics of the modulation, whose coefficients may be computed by different techniques, depending on the truncation of the expansion. In a simple sense, the dispersion may be determined by solving an eigenproblem formulated by the Helmholtz equation in an infinitely periodic structure. Such eigenproblem has the following generalized form:

$$\nabla \times \left[\frac{1}{\varepsilon(r)} \nabla \times H(r)\right] = \left(\frac{\omega}{c}\right)^2 E(r) \tag{1.7}$$

where ω/c is the eigenfrequency for the corresponding eigenmode $H(r)$ with dielectric function $\varepsilon(r)$, a periodic function with period R, $\varepsilon(r) = \varepsilon(r + R)$. Assuming a plane wave expansion, the solutions of Eq. (1.7), inside an infinite PhC can be written as: $H(r) = h(r)\, e^{ikx}$, where $h(x) = h(r + R)$ is a periodic function with period R, and plane wavevector k. In wavevector representation, the periodicity of the dielectric function: $\varepsilon(r) =$

$\int \varepsilon(k)e^{-ik\cdot r}dk = \int \varepsilon(k)e^{-ik\cdot r}e^{-ik\cdot R}dk$ requires either $\varepsilon(k) = 0$ or $e^{-ik\cdot R} = 1$. The wavevectors, k, which fulfill this condition $e^{-ik\cdot R} = 1$ or $k \cdot R = 2n\pi$, where n is an integer, are reciprocal lattice vectors, denoted q (or alternatively by G in the literature). So, we can expand $\varepsilon(r)$ and $H(r)$ into a Fourier series of reciprocal vectors:

$$\varepsilon(r) = \sum_q \varepsilon(q)e^{-iq.r} \ , \quad h(r) = \sum_q h(q)e^{-i(k+q).r} \tag{1.8}$$

where $\varepsilon(q)$ and $h(q)$ are Fourier coefficients of the corresponding plane waves. Then, using Eq. (1.7), we can rewrite the Eq. (1.6) for 1D PhC in the following way:

$$\sum_{q'} \varepsilon^{-1}(q-q')((k+q) + (k+q').h(-q') = \left(\frac{\omega}{c}\right)^2 h(q') \tag{1.9}$$

Equation (1.9) is the master equation that is used to compute the temporal dispersion $\omega(k)$ over the unit cell of the lattice at each Bloch wavevector, k. The dispersion relation provides the dependence of eigenfrequencies of the system mode propagating through the structure, $\omega(k)$, on the wavevector, k. In order to determine the dispersion relation, we consider one period (d) of 1D PhC structure, as a unit cell with $R = d$ and $q = 2\pi/d$, and determine the eigensolutions for wavevectors, k, lying within the first Brillioun zone that correspond to $k = [-\pi/d, \pi/d\ ]$. In PhCs, the eigenfrequencies are always real-valued, and mode coupling changes the phase velocity of the wave. The eigenfrequencies push each other at resonance, $k = q/2$, and form the PBG. The propagation of forbidden frequencies corresponding to PBGs is shown with shaded areas on Fig. 1.5(a).

In order to study the transmission, reflection and absorption properties of finite 1D PhC structures, one may use a transfer matrix approach. The Transfer Matrix Method (TMM) is one of the fundamental methods used in optics to analyze the scattering properties of layered structures. This approach relates the forward and backward fields propagating through each layer of the structure and interaction on interfaces between the layers. First, the relation between forward and backward propagating fields at each interface of the layered structure is determined using a 2×2 matching matrix (M). Then, forward and backward fields are propagated from one interface to the other using a 2×2 propagation matrix (P). Finally, matching and propagation matrices relating the fields across different interfaces are combined to form the transfer matrix.

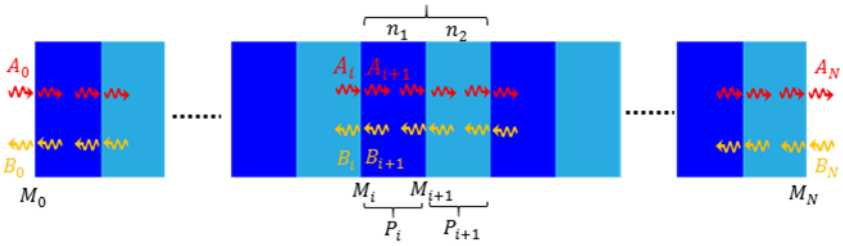

Figure 1.4. Finite structure of 1D PhC with N periods. The arrows at different positions show the forward and backward propagating fields. M represents the matching matrix and P represents the propagation matrix.

We assume a finite 1D PhC structure consisting of periodically stacked bilayers (j=2) with corresponding refractive index, n_j. The field distribution within the jth layer is the superposition of the forward and backward propagating waves of wavevector, k, reads:

$$E_j(x) = A_j e^{-ikx} + B_j e^{-ikx} \tag{1.10}$$

where A_j and B_j are the amplitudes of forward and backward propagating fields at the jth layer. The forward and backward fields inside each layer are represented by the arrows in Fig. 1.4. The backward fields appear due to the Fresnel reflection at each interface between two media. In order to calculate the matching matrix, we apply the boundary conditions at each interface which requires that the tangential components of the total field are continuous across the interface, i.e. $E_j = E_{j+1}$. Note that, for simplicity, we consider incident fields are normal to each material interface. The resultant matrix relates the forward and backward propagating field using the Fresnel coefficients in this form:

$$\begin{bmatrix} A_{j+1} \\ B_{j+1} \end{bmatrix} = M \begin{bmatrix} A_j \\ B_j \end{bmatrix}, \quad M = \frac{1}{t_{ml}} \begin{bmatrix} 1 & r_{lm} \\ r_{lm} & 1 \end{bmatrix} \tag{1.11}$$

the reflection, r_{lm}, and transmission, t_{ml}, coefficients between layers $l = j$ and $m = j + 1$ in the M-matrix can be defined as:

$$r_{lm} = \frac{n_l - n_m}{n_l + m_l} \tag{1.12}$$

$$t_{ml} = \frac{2n_m}{n_l + m_l} \tag{1.13}$$

On the other hand, the propagation matrix introduces the phase shifts acquired by the fields through each layer, of thickness $d/2$ and refractive index n_j. After propagation, the fields acquire phase shifts expressed as:

$$\begin{bmatrix} A_{j+1} \\ B_{j+1} \end{bmatrix} = P \begin{bmatrix} A_j \\ B_j \end{bmatrix}, \quad P = \begin{bmatrix} e^{\frac{in_j k_0 d}{2}} & 0 \\ 0 & e^{-\frac{in_j k_0 d}{2}} \end{bmatrix} \tag{1.14}$$

Now, we can utilize these matching and propagation matrices to study the transmission, reflection and absorption properties of finite 1D PhC. The two interfaces in the structure give matching matrices (M_1, M_2) while two material layers give propagation matrices (P_1, P_2). The transfer matrix, combining the matching and propagation matrices, for wave propagation over one period is expressed as: $T = P_2 M_2 P_1 M_1$. Since the structure is periodic, we can write the amplitudes of forward and backward fields propagating through N periods of the structure in the following way:

$$\begin{bmatrix} A_N \\ B_N \end{bmatrix} = M_N T^N M_0 \begin{bmatrix} A_0 \\ B_0 \end{bmatrix}, \quad T^N = \begin{bmatrix} T_{11}^N & T_{12}^N \\ T_{21}^N & T_{22}^N \end{bmatrix} \tag{1.15}$$

where T^N is transfer matrix for finite 1D PhC composed of N periods. M_0 is the matching matrix at the left-hand side of the PhC, while M_N is the matching matrix at the right-hand side of the PhC structure. When there is no backwards incident at the end of the bilayer of the PhC, i.e. $B_N = 0$ and transmission (T), reflection (R) and absorption (A) may be calculated as:

$$T = \frac{A_N}{A_0}, \qquad R = \frac{B_0}{A_0}, \qquad A = 1 - T - R \tag{1.16}$$

The transmission and reflection spectra for a finite 1D PhC structure is shown in Fig. 1.5(b). The system shows almost zero transmission for certain frequencies corresponding to the first Photonic Band Gap (PBG), where the filed propagation is inhibited by the structures. The oscillations outside the PBGs can be attributed to the finite extent of the structure.

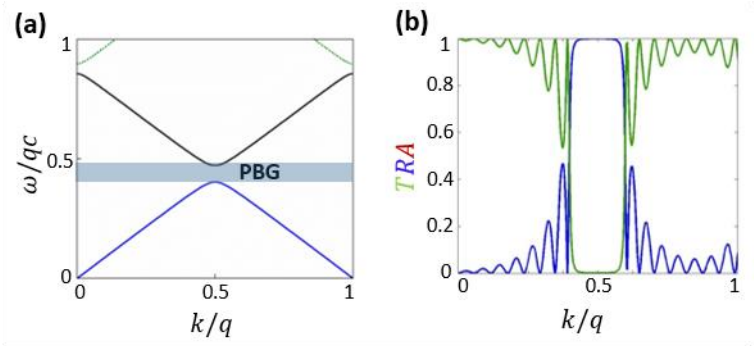

Figure 1.5. Wave propagation in a 1D PhC: (a) dispersion relation obtained by PWE for infinite extended structure, (b) transmission, T, reflection, R, spectra obtained by TMM for the structure of finite extent with N=10; in both plots frequency and wavevector are normalized to the reciprocal lattice vector, q. The parameters of this particular simulation are: $n_1 = 3$, and $n_2 = 1$.

1.3.2 Wave propagation in Gain-loss Modulated Materials

Gain-Loss Modulated Materials (GLMMs) are periodic structures where the gain and loss are spatially modulated in a periodic manner on the wavelength scale. Such materials have already been investigated in one-dimensional systems such as distributed feedback lasers in which the active media is periodically modulated in one spatial dimension to provide optical feedback [Kog71, Che08]. To understand the wave propagation in GLMMs, we consider a simple 1D periodic structure shown in Fig. 1.6. The structure consists of two different materials of same thickness $d/2$ with the same real refractive index , n^{Re}, but with either gain or loss ($n_1 = n^{Re} + in_1^{Im}$) depending on the sign of the imaginary part of the refractive index n^{Im}.

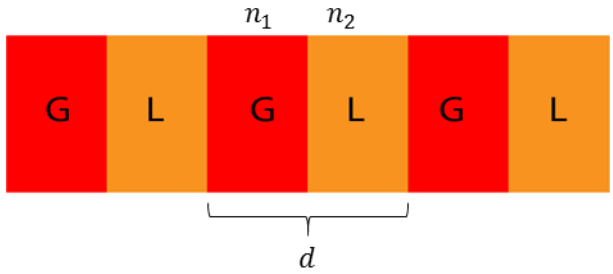

Figure 1.6. Schematic illustration of 1D GLMM with gain (G) and loss (L) layers of thickness, $d/2$, with refractive indices n_1 and n_2, respectively. The periodicity of the structure is $d = 2\pi/q$, where q is the lattice wavevector.

Similarly to the previous section, the dispersion properties of the infinite structure may be investigated using Plane Wave Expansion method. The coupling mechanism in GLMMs is symmetric, as for PhCs, but eigenfrequencies are complex. The real part of the eigenvalue represents frequency, while the imaginary part determines the temporal growth or decay of the corresponding mode. However, when the gain and loss are balanced eigenvalues are real, away from resonance. In such materials, the modes pull each other at resonance which results in locking of some modes at those frequency ranges. Within this locked-frequency range, the imaginary part of eigenfrequencies develops, either leading to amplification or attenuation. As a result, such materials provide directional gain in 2D GLMM structures, leading to different interesting spatial effects such as spatial filtering [Sta09, Bot10], self-collimation [Sta09], flat lensing [Kum13], etc.

Another interesting effect of GLMM is that the presence of a growing mode leads to an enhanced transmission at resonance [see Fig. 1.7(b)]. Therefore, contrary to PhCs where transmission is attenuated in PBGs, GLMMs show antibandgaps at resonance, see the shaded area in the dispersion diagram in

Fig. 1.7(a). The transmission, reflection and absorption properties of 1D GLM structure, of finite size, may be studied using transfer matrix approach [see Fig. 1.7(b)].

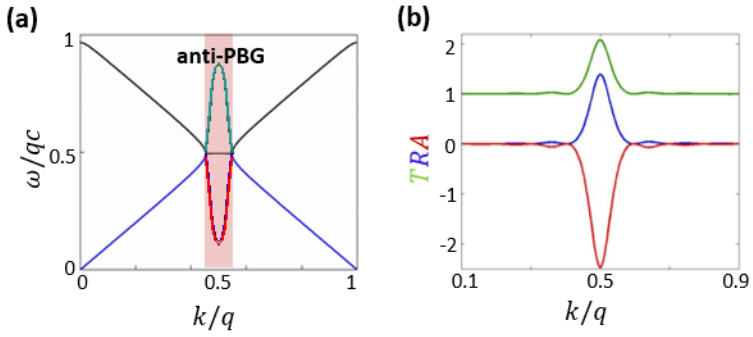

Figure 1.7. Wave propagation in 1D GLMM: (a) dispersion relation as obtained by the PWE method. The imaginary part of the eigenfrequency is superimposed in (a) to show growing (or decaying) of the mode at $k = q/2$, (b) transmission, T, reflection, R, and absorption, A, spectra obtained by TMM for the finite structure with N=10. In both plots, the wavevector, k, is normalized to the lattice vector, q. The simulation parameters are: $n_1 = 1 + 0.2i$, and $n_2 = 1 - 0.2i$.

1.3.3 Wave propagation in PT-symmetric systems

Next, we study the propagation properties of PT-symmetric systems, which may be regarded as a superposition of PhCs and GLMMs with a phase shift between them of a quarter of the period of the modulation. The main feature of PT-symmetric systems is that they hold the utterly interesting property of unidirectionality by appropriately engineering gain and loss regions. In such systems, there exists a threshold above which the system undergoes a phase transitions from real to complex eigenspectrum and no longer maintains its symmetric mode coupling. This transition point also called spontaneous PT-symmetry breaking point (or exceptional point). As a

result, the reflection from a finite PT-symmetric structure may not be symmetric, being diminished from one side while enhanced from the other side [Lin11]. In order to analyze the scattering properties of such structure, we will use the TMM approach. We consider a discrete PT-symmetric structure consisting of four different layers of same thickness, $d/4$, with different refractive indices (n_1, n_2, n_3, n_4) which are periodically repeating in space over the period, d, as shown in Fig. 1.8(a). Layer 1 and 3 have real-valued refractive index, n^{Re}, with high $(n_1 = n_1^{Re} + 0i)$ and low $(n_3 = n_3^{Re} + 0i)$ refractive indices, while Layer 2 and 4 have complex conjugated refractive indices, $n_2 = n^{Re} + in^{Im}$ and $n_4 = n^{Re} - in^{Im}$, where n^{Re} and n^{Im} are positive for balanced gain and loss regions.

In case of passive PhC structure, when there is no gain and loss in the system, we can obtain high reflections for certain frequencies around Bragg condition, thus, acting as high-quality reflectors. Instead, the inclusion of gain and loss in such structures in a PT-symmetric arrangement leads to new functionalities and unconventional wave behavior. We study the transmission, reflection and absorption properties for left and right incident waves, as shown in Figs. 1.8(a) and 1.9(b), respectively. We observe that, when gain and loss are balanced, reflection properties are dependent on the direction of an incident light. For instance, when an incident light is entered from the left side of the structure, the system becomes reflectionless over frequencies at the exceptional point [see Fig. 1.8(b)]. On the other hand, reflection is enhanced when the wave is entered from the right side [see Fig. 1.9(b)]. This difference of reflectivity is due to asymmetric coupling between left and right propagating modes. However, the transmission remains the same irrespective of the incident wave direction.

We would like to mention that PT-symmetric structures are conceptually different from conventional distributed feedback lasers where both the index and gain-loss profiles are in phase. Precisely, the phase shift in the index and gain-loss modulations creates the exceptional point in PT-symmetric systems that leads to unidirectional behavior.

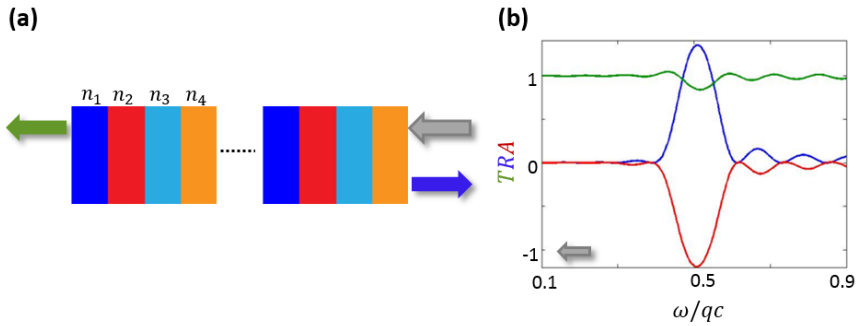

Figure 1.8. (a) Periodic PT-symmetric structure for left side incident wave showing unidirectional transmission (b) corresponding spectral transmission, T, reflection, R, and absorption, A, calculated with TMM, for the finite structure with N=4. The parameters are: $n_1 = 1.2$, $n_2 = 1.1 + 0.1i$, $n_3 = 1$, and $n_4 = 1.1 - 0.1i$.

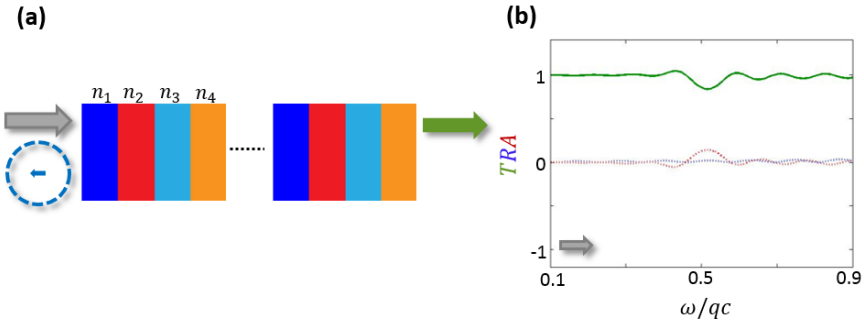

Figure 1.9. (a) PT-symmetric structure for right side incident wave (b) corresponding transmission, reflection and absorption spectra. Same structure as in Fig. 1.8.

1.4 Beam propagation in Complex periodic media

In the previous section, we explained wave propagation phenomena in different periodic structures, i.e. PhCs, GLMMs, and PT-symmetric systems. In all cases, propagation is determined by the wave equation (Eq. (1.2)), which is further simplified assuming a stationary field amplitude, $\partial E/\partial t = 0$, to obtain the scalar Helmholtz equation:

$$\nabla^2 E(r) + \left(\frac{n\omega}{c}\right)^2 E(r) = 0 \tag{1.17}$$

Equation (1.17) provides an important link between wave dynamics of optical and quantum systems, as discussed in section 1.2.1. To find the solution of the Helmholtz equation, we use ansatz: $E(r) = Ae^{ik\cdot r}$ where A denotes the amplitude of a plane wave propagating in wavevector direction, $\vec{k} = [k_x,\ k_y, k_z]$. Then, the propagation equation for the field amplitude, A, can be rewritten as:

$$\nabla^2 A + 2ik\nabla A + (n^2 - 1)k^2 A\ = 0 \tag{1.18}$$

We finally consider the propagation along z-direction and apply the slowly varying envelope approximation $|\partial A/\partial z| \ll |A|k,\ \partial A^2/\partial z^2 = 0,$ which results into the following paraxial equation:

$$\frac{\partial A}{\partial z} = \frac{i}{2k}\nabla^2 A + i\frac{k}{2}(n^2 - 1)A\ = 0 \tag{1.19}$$

Assuming media with a complex refractive index $n(x) = n_0 + \Delta n$, where n_0 is the average value and $\Delta n(x)$ is the weak modulation, the equation can be simplified to:

$$\frac{\partial A}{\partial z} = \frac{i}{2k}\nabla^2 A + i\frac{k}{2}(n^2 - 1)A = 0 \tag{1.20}$$

Note that we assume 1D modulated system for simplicity, however, the modulation can be in two-(or higher) dimensions. The final equation in the normalized form can be written as:

$$\frac{\partial A}{\partial z} = i\nabla^2 A + iV(x)A \tag{1.21}$$

where $V(x)$ is the optical potential representing the modulation of the complex refractive index. We note that Eq. (1.21) describes the evolution of the beam envelope, A, propagating in z-direction. Moreover, the same equation structure is obtained for the time evolution of the field amplitude, just replacing z by t and even it is analogue to the Schrödinger equation for a quantum wave function. We use this paraxial equation in the thesis to study beam propagation through different kinds of non-Hermitian systems because it substantially simplifies the problem to explicit analytical expressions in asymptotical cases.

1.4.1 Spatial dispersion

Several analytical and numerical approaches can be found in the literature for studying the dispersion relations of periodic structures. The coupled harmonic expansion, or plane wave expansion, is one of the most convenient approaches relying on expansion of the field into a finite set of Bloch modes that couple with the harmonics of the periodic potential. As a result, a set of linear coupled equations are obtained and used to compute the transverse dispersion relation of the considered structure.

We consider a general 1D non-Hermitian harmonic potential expressed as:

$$V(x) = n_{Re}\cos(qx) + in_{Im}\cos(qx - \varphi) \tag{1.22}$$

where n_{Re} and n_{Im} are the amplitudes of index and gain-loss modulation while q and φ are the frequency and phase shift between index and gain-loss modulation, respectively. The real and imaginary parts of the potential independently correspond to a PhC and a GLM systems with a simple harmonic variation of real and imaginary refractive index, respectively. These index and gain-loss modulations can be dephased depending on phase shift, φ. The potential becomes PT-symmetric for a phase shift of quarter of the period of the modulation, i.e. $\varphi = \pi/2$.

To determine the dispersion of a complex system analytically, we use a similar approach referred to the Coupled Mode Expansion. The dispersion properties of such a potential can be explored for PhC, GLM and PT-symmetric cases. The technique of Coupled Mode Expansion expands the field into a set of Bloch modes in the form:

$$A(x) = e^{ik_x x}\sum_l a_l e^{ilqx} \tag{1.23}$$

which is inserted into Eq. (1.22) and after considering three most relevant harmonics, $l = -1, 0, 1$, we obtain:

$$\frac{da_{-1}}{dz} = -i(k_x - q)^2 a_{-1} + i\frac{\left(n_{Re} + in_{Im}e^{i\varphi}\right)}{2}a_0 \tag{1.24a}$$

$$\frac{da_0}{dz} = -ik_x^2 a_0 + i\frac{\left(n_{Re} + in_{Im}e^{-i\varphi}\right)}{2}a_{-1} + i\frac{\left(n_{Re} + in_{Im}e^{i\varphi}\right)}{2}a_1 \tag{1.24b}$$

$$\frac{da_1}{dz} = -i(k_x + q)^2 a_1 + \frac{i\left(n_{Re} + in_{Im}e^{-i\varphi}\right)}{2} a_0 \qquad (1.24c)$$

The coupled system can be expressed in a matrix form:

$$\begin{bmatrix} \dot{a_{-1}} \\ \dot{a_0} \\ \dot{a_1} \end{bmatrix} = M \begin{bmatrix} a_{-1} \\ a_0 \\ a_1 \end{bmatrix} \qquad (1.25)$$

where M is the coupling matrix:

$$M = \begin{bmatrix} -i(k_x - q)^2 & \frac{i(n_{Re} - n_{Im})}{2} & 0 \\ \frac{i(n_{Re} + n_{Im})}{2} & -ik_x^2 & \frac{i(n_{Re} - n_{Im})}{2} \\ 0 & \frac{i(n_{Re} + n_{Im})}{2} & -i(k_x + q)^2 \end{bmatrix} \qquad (1.26)$$

This matrix eigenvalues correspond to the solutions of the coupled equations system, providing the spatial dispersion, $k_z(k_x)$, of the considered spatially modulated medium.

The analysis restriction to three modes is justified by the small modulations amplitudes of the refractive index because higher order harmonics have a negligible effect on the main features of the system dynamics. The modes' dispersion is considered to be parabolic, and it is distorted upon interaction at resonance, $k_x = q/2$, depending on the medium properties. For instance, the spatial dispersion for purely real and imaginary modulations are depicted as solid blue and red curves in Fig. 1.10, respectively. The behavior of two modes near the crossing point, $k_x = q/2$, can simply be described by the analytical expression [Bot10]:

$$\Delta k_z = \pm c\sqrt{\Delta k_x^2 - \frac{n^2 k_0^2}{4}} \tag{1.27}$$

where c is the light velocity, Δn is the modulation amplitude of the refractive index, $\Delta k_z = k_z - q/2$ and $\Delta k_x = k_x - q/2$ are the deviations from resonance. The system dynamics mainly depends on the index (n_{Re}) and gain-loss (n_{Im}) modulation amplitudes which define the coupling between harmonics. Since the considered potential is complex in nature, the coupling between the harmonic components can be reactive or dissipative depending on the modulation amplitudes. PhCs and GLMs are two limiting cases of PT-symmetric systems having quite different spatial dynamics, as we discussed earlier.

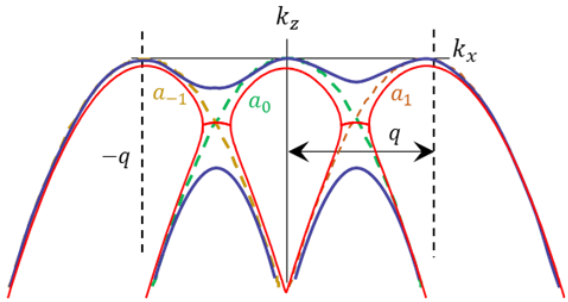

Figure 1.10. Real part of the spatial dispersion for the three-mode model. Dotted lines show the dispersion of three uncoupled modes (a_0, a_{-1}, a_0) represented with parabolas. The coupling between the modes distorts the parabolas, and the resultant curves are represented with solid blue and red lines for real refractive index and imaginary refractive index, respectively.

First, we consider a PhC having a coupling matrix with the following form:

$$M_{PhC} = \begin{bmatrix} -i(k_x - q)^2 & \frac{in_{Re}}{2} & 0 \\ \frac{in_{Re}}{2} & -ik_x^2 & \frac{in_{Re}}{2} \\ 0 & \frac{in_{Re}}{2} & -i(k_x + q)^2 \end{bmatrix} \tag{1.28}$$

The corresponding spatial dispersion relation is shown in Fig. 1.11(a). The reactive coupling pushes the eigenvalues apart from resonance between the coupled modes creating the first PBG in the spatial dispersion. In this case, all eigenvalues are real-valued and provide the propagation wavenumber of the Bloch mode. We also calculate the eigenvectors (b_{-1}, b_0, b_1) which components correspond to the red branch of eigenvalues, as shown in Fig. 1.11. Note that eigenvectors show a symmetric flow between coupled modes.

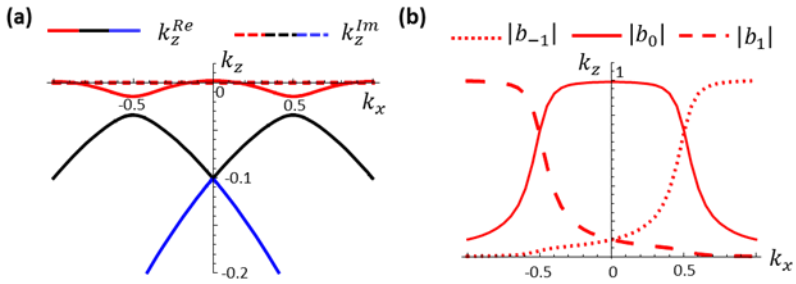

Figure 1.11. (a) Eigenvalues for PhC case (b) eigenvectors corresponding to the red dispersion branch showing a symmetric coupling. The parameters are: $n_{Re} = 0.20$, and $n_{Im} = 0$. We note that k_x is normalized to q_x and k_z.

Next, we study the dispersion properties of a GLM system. The coupling matrix for these systems has the following form:

$$M_{GLM} = \begin{bmatrix} -i(k_x - q)^2 & -\frac{in_{Im}}{2} & 0 \\ \frac{in_{Im}}{2} & -ik_x^2 & -\frac{in_{Im}}{2} \\ 0 & \frac{in_{Im}}{2} & -i(k_x + q)^2 \end{bmatrix} \tag{1.29}$$

In the presence of gain-loss, the system displays complex conjugated eigenvalues at resonance, attributed to the dissipative coupling. The real part of the eigenvalues locks while a nonzero imaginary part develops, leading to growing and decaying propagating modes. Eigenvalues and eigenvector components corresponding to the red curve eigenvalue are shown in Fig. 1.12. Similar to PhC case, the coupling between the modes in GLM system is symmetric. However, locking areas appear, which are at the basis of antibandgaps.

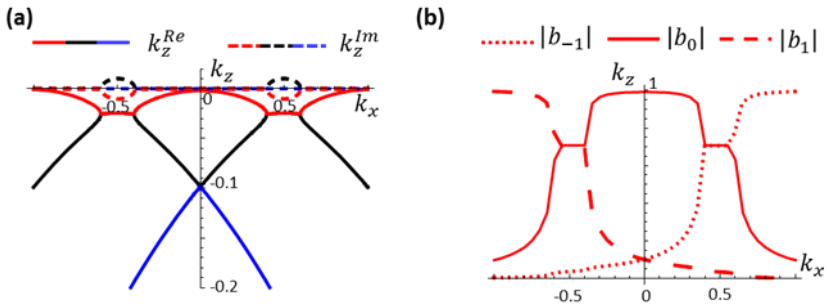

Figure 1.12. (a) Eigenvalues for a GLM case (b) eigenvectors corresponding the red dispersion branch showing a symmetric coupling. The parameters are: $n_{Re} = 0$, and $n_{Im} = 0.2$. We note that k_x is normalized to q_x and k_z.

Finally, we investigate the dispersion relation of a PT-symmetric case, i.e. $\varphi = \pi/2$. In such materials, the most interesting situation occurs at PT-symmetry breaking point ($n_{Re} = n_{Im} = n$) above which the eigenvalues

become complex, as discussed in section 1.3.3. In this case, the coupling of the modes is expressed in the coupling matrix (M) obtained from Eq. (1.23) as:

$$M_{PT} = \begin{bmatrix} -i(k_x - q)^2 & 0 & 0 \\ in & -ik_x^2 & 0 \\ 0 & in & -i(k_x + q)^2 \end{bmatrix} \tag{1.30}$$

Matrix (1.30) clearly indicates that, at the PT-transition point, the mode a_0 couples only to mode a_{-1}, while it does not couple to a_1 leading upper diagonal elements to zero. This asymmetric coupling between modes allows the unidirectional flow of fields with real eigenvalues, as shown in Fig. 1.13(a). In this case, the three modes cross each other at resonance leaving the three parabolas undistorted in the spatial dispersion and the corresponding eigenvector components display the asymmetric behavior, as shown in Fig. 1.13(b).

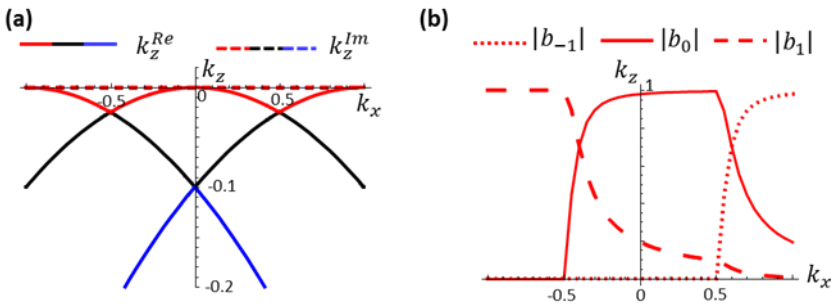

Figure 1.13. (a) Eigenvalues for PT-symmetric case (b) eigenvectors corresponding to the red dispersion branch showing an asymmetric coupling. The parameters are: $n_{Re} = n_{Im} = 0.2$. We note that k_x is normalized to q_x and k_z.

1.4.2 Numerical integration for Beam propagation

Apart from analytical predictions on wave propagation, we also perform numerical beam propagation simulations to verify the expected behaviors. Split-Step Method (SSM) is one of the most widely used numerical techniques to solve the nonlinear partial differential equations due to its lower complexity and easy implementation relative to other methods. SSM belongs to a family of pseudospectral methods, which are typically much faster and flexible as compared to finite difference time domain methods [Taf05]. However, time-domain techniques are inherently more accurate due to the inclusion of forward-backward propagating fields, only compromising at the cost of increased computation time. SSM deals with the linear and nonlinear part of the system equation separately. The solution of the linear part is determined in the frequency domain while the nonlinear part is computed in real space. We use this method to solve either linear or nonlinear system numerically throughout the thesis.

As an example, we shall consider the propagation of beam through a non-Hermitian medium in 1D transverse space with a potential, $V(x) = n_{Re}\cos(qx) + i\, n_{Im}\cos(qx - \varphi)$. The paraxial equation reads:

$$\partial_z A = i\nabla^2 A + i[n_{Re}\cos(qx) + i\, n_{Im}\cos(qx - \varphi)]A \qquad (1.31)$$

For the numerical analysis, we solve Eq. 1.31 using the split-step method and investigate the evolution of a Gaussian beam in the considered potential for different cases. We start with a simple case when the modulation is either purely real (PhC case, $n_{Im} = 0$) or imaginary (GLM case, $n_{Re} = 0$). The results for the beam propagation in PhC and GLM media are shown in Figs.1.14 (a) and 1.14(b), respectively. During the propagation, the beam interacts with potential and couple the energy to the modes, $k \pm q$ and

higher order harmonics. As expected, in both cases, the spatial spectrum of the field after sufficient propagation shows the symmetric coupling between the modes, $k \pm q$. However, the modes are amplified in the gain-loss case due to the predicted antibandgaps situation which is evident in Fig. 1.14 (b).

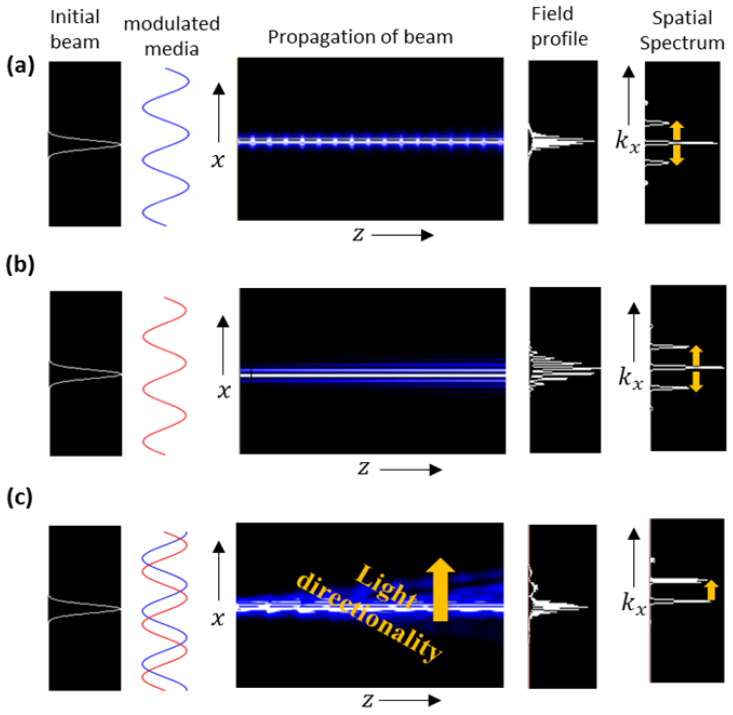

Figure 1.14. Beam propagation in complex periodic media (a) PhCs case with $n_{Re} = 0.25$, and $n_{Im} = 0$ (b) GLMMs case with $n_{Re} = 0$, and $n_{Im} = 0.25$ (c) PT-symmetric case with $n_{Re} = n_{Im} = 0.20$.

Finally, we study the PT-symmetric case for $\varphi = \pi/2$. As previously shown, the most interesting situation in PT-symmetric systems occurs at the exceptional point ($n_{Re} = n_{Im}$). We propagate the beam in PT-symmetric medium at the exactly exceptional point and observe the evolution of the

beam for the same propagation length. The field spectrum is also shown in Fig. 1.14(c). The field and corresponding spectrum clearly indicate an asymmetric energy flow between the modes. The disappearance of mode at $k+q$ in the spatial spectrum clearly shows that the coupling is unidirectional in PT-symmetric case. We find that the results of the beam propagation in complex media follow the predictions of wave propagation in complex media. The general conclusion is that the paraxial model can be used as a testbed to verify different spatial effects in complex systems. Therefore, we use it in the following chapters to test our proposed theories.

Chapter 2

Local PT-symmetric Systems

Inspired by the PT- symmetry breaking property of non-Hermitian systems, we now propose to apply the notion of PT-symmetry in restricted spatial domains, referred as *local PT-symmetry*. We expect that, despite having no global PT-symmetry, the system with *local PT-symmetry* may also show nontrivial effects arising from the different light directionality forced in each spatial domain. A particularly interesting case is the axial symmetry that may lead to the localization phenomenon. Therefore, this chapter describes the novel optical systems that possess local PT-symmetry and axial symmetry. The field localization in such systems is based on non-Hermitian physics which is conceptually different from conventional localization mechanisms that commonly rely on Bragg gratings or gain gratings (distributed feedback) with discontinuities or defects for the case of periodic media or in Anderson localization in disordered media [Sch07]. The fundamental concept in axial PT-symmetry is grounded on a unidirectional (inwards) mode coupling mechanism, in which both index and gain modulations contribute simultaneously to the field localization and enhancement. We study one-dimensional (1D) periodic and quasiperiodic systems to demonstrate the localization mechanism based on the inward coupling. The idea is further extended to two-dimensional (2D) periodic

PT-axisymmetric geometries to show sharp localization and strong enhancement, due in this case to a radial inward coupling. The chapter presents the detailed analysis of the dynamics of PT-axisymmetric systems.

2.1 Introduction to Local PT-symmetry

In the previous chapter, we discussed that PT-symmetric media have recently attracted significant attention for holding intriguing new phenomena relying on the unidirectional mode coupling among which are: unidirectional reflection [Lin11], unidirectional waveguide-coupling [Rut10], coherent perfect absorption [Lon10], lose induced lasing [Pen14a], single longitudinal mode selection [Hod14], constant intensity propagation [Mak15], etc. We would like to emphasize that in all those cases PT-symmetry has been exploited globally in spatial domains, to explore new functionalities. Global PT-symmetry means that the system *uniformly* holds continuously PT-symmetric conditions. On the contrary, the spatial symmetry of a system can be globally broken under PT-transformations while preserving it on a local scale. In this case, the system is *non-uniformly* PT-symmetric holding PT-symmetry on subsystems, i.e. restricted spatial domains—local PT-symmetry. So far, less attention has been paid, to study local PT-symmetry. In most cases, the role of local symmetries is ignored in the systems regardless of their intrinsic presence. The main purpose to design such PT-symmetry locally is to direct the light to follow a desired direction in the local space. In this chapter, we exploit local PT-symmetry for extraordinary field concentration. We combine local PT-symmetry with axial symmetry in periodic systems we refer as *PT-axisymmetric systems*, to observe the simultaneous field localization and enhancement at a selected position which could possibly underpin a new generation of optical systems.

In fact, among the flurry of recent research activities in non-Hermitian photonics, as discussed in Chapter 1, some refer to local PT-symmetry, however in different perspectives since the concept is not analogous to the one we propose here. Kottos and his colleagues used the local PT-symmetry in a particular class of photonic lattices consisting of coupled PT-symmetric dimers. In such configuration, each dimer, represented as a pair of sites, possesses PT-symmetry with respect to its center, referred as P_dT symmetry but the system, as a whole, lacks global symmetry due to the arbitrary choice of each dimer site energies and coupling between dimers [Ben10]. They showed that lattices holding P_dT symmetry exhibit a real spectrum in a wide parameter range and robust against disorder. Later on, they studied P_dT symmetry in photonic lattices (consisting of dimers) to explore non-trivial beam dynamics such as conical diffraction phenomenon [Ram12b], curved and focusing caustic trajectories [Ben15a], and stable Bloch-Zener oscillations [Ben15b]. Nguyen et al. used the similar concept of P_dT symmetry for ladder-shape lattices and studied the effect of disorder on transport and localization properties of waves [Ngu16]. In addition, PT-symmetric coupled configurations were studied to investigate switching [Lup13] and parametric oscillations [Gan12]. Lee et al. reported that a local PT-symmetry holding on composite systems may violate the non-signaling principle of relativity and may allow superluminal propagation [Lee14]. Wimmer et al. observed the stable optical solitons in fiber loop platform, comprised of PT-symmetric lattices that fulfill the PT-symmetry condition along a certain cross-section of the lattice, referred as local PT-symmetric lattices [Wim15]. We would like to mention that our proposal of local PT-symmetry in periodic systems for field localization is completely novel and conceptually different as compared to above-mentioned studies.

2.2 PT-axisymmetry

In chapter 1, we provided an overview of Hermitian and non-Hermitian optical systems generated by combining refractive index and gain-loss modulations. The simplest case of a periodic index modulation, a 1D Photonic Crystals (PhCs), may be described by a harmonic potential as $n = n_{Re}\cos(qx)$. Analogously, a simple 1D while gain-loss modulation (GLM) may be represented as: $n = in_{Im}\cos(qx + \phi)$ being n_{Re} and n_{Im} the amplitudes, and q the spatial wavenumber of the modulations, and ϕ a phase. In both situations, either for the PhCs or GLM case, the propagating modes with wavevector $|k|$ are symmetrically coupled to higher and lower frequencies through the spatial periodicity, irrespective of the different wave dynamics that results in bandgaps (PhCs) and antibandgaps (GLM) at resonance, $k = 2q$, respectively. The most interesting situation occurs for a complex optical potential, when both index and gain/loss are phase shifted with a quarter period of modulation, i.e. $n = n_{Re}\cos(qx) + in_{Im}\sin(qx)$, holding PT-symmetry. In such systems, the coupling among propagating modes becomes strongly unidirectional when both modulations have the same amplitude, i.e. $n = n_{Re} = n_{Im}$. The point of balanced modulation is an exceptional point, in the sense that above it the eigenspectrum of system is no more real, it becomes complex leading to an exponential growth (or decay) of the mode energy. According to the two-mode coupled theory, the ratio between real and imaginary index modulation amplitudes defines the asymmetric coupling between modes. Around the exceptional point, the forward propagating mode is unidirectionally coupled to the backward propagating mode, but not vice versa. This coupling mechanism is easy to understand while considering two modes, but it becomes more engaged in the several modes (or mode continuum) approach. Despite this complexity,

the exceptional point is always present irrespective of the number of modes contributing to the asymmetric properties of the PT-symmetric system.

Here, our interest is to investigate what happens to the system dynamics if the PT-symmetry condition is globally broken, while it holds locally. Let us consider a simple 1D periodic potential which consists of two P-symmetric half-spaces, where each half-space is defined by a PT-symmetric potential that introduces opposed directional couplings being, for example, such coupling left-handed for $x < 0$ and right-handed for $x > 0$, as shown in Fig. 2.1(a). In each half-space, PT-symmetry is locally satisfied on periodically distributed points. The local PT-symmetry, combined with the axial symmetry, may direct the field towards the symmetry center, at $x = 0$, due to inward unidirectional coupling in each half-space. Therefore, we may intuitively expect that the field is concentrated at the center, $x = 0$. On the other hand, interchanging the index and gain-loss modulations, as depicted in the second row of Fig. 2.1(a), the field may be spread because the unidirectional coupling is outwards instead of inwards. This axial configuration can be extended to 2D or 3D systems with a radial symmetry, where the asymmetric radial coupling between incoming and outgoing propagating waves is inwards, leading to an accumulation of the field at the center, $r = 0$. The idea is schematically shown for either favored inward or outward couplings in Fig. 2.1(b).

Mathematically, the proposed periodic PT-axisymmetric systems can be described with different potential profiles. The general condition for the potential to show periodic local PT-symmetry is $V(|r_0 + r|) = V^*(|r_0 - r|)$ for periodically distributed points, r_0 where $r_0 \neq 0$ while axial symmetry is given by $V(r) = V(-r)$ for all r. We consider a simple harmonic PT-symmetric potential in 1D and 2D in the following form:

$$V(x) = n_{Re}\, cos(q|x| + \phi) - i n_{Im}\, sin(q|x| + \phi) \qquad (2.1)$$

$$V(x) = n_{Re}\, cos(q|x| + \phi) - i n_{Im}\, sin(q|x| + \phi) \qquad (2.2)$$

where n_{Re} and n_{Im} are amplitudes of real and imaginary part of refractive index modulation and q is the spatial frequency of the modulation. The phase, ϕ, of the potential defines the character of the symmetry center, $r = 0$. Hence, we characterize the potential by three parameters: (n_{Re}, n_{Im}, ϕ) to evaluate the performance of the system.

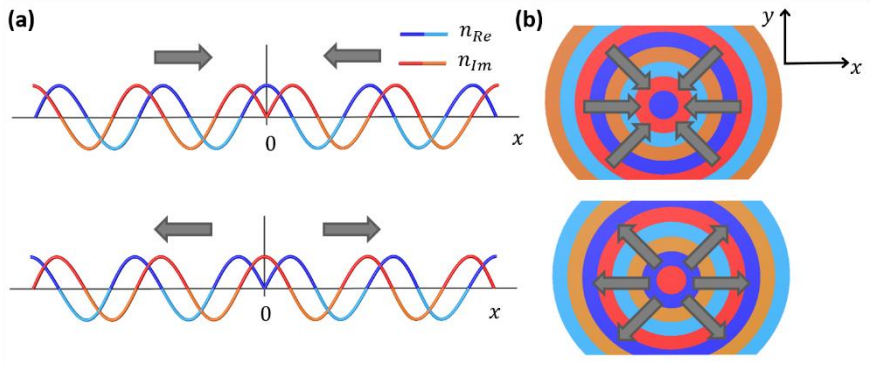

Figure 2.1. Local unidirectional coupling: (a) 1D complex optical potential, where n_{Re} is the real index modulation, and n_{Im} the gain-loss modulation. In the top configuration, a field concentration may be expected at x=0. (b) 2D analogous axisymmetric configuration. The arrows in (a) and (b) indicate the direction of the asymmetric mode coupling.

2.3 Mathematical model

To deal with the propagation of light beams in PT-symmetric structures with smooth spatial periodic modulations, we consider the paraxial propagation of the field:

$$\partial_t A(\vec{r},t) = i\,\nabla^2\,A(\vec{r},t) + iV(\vec{r})A(\vec{r},t) \qquad (2.3)$$

where $A(\vec{r},z)$ is the normalized slowly varying amplitude envelope of the complex electromagnetic field distributed in transverse space, $\vec{r} = (x,y)$, and evolving in time, t, and ∇^2 is the laplacian operator in transverse space (x,y) that represents diffraction. $V(\vec{r})$ is the non-Hermitian potential satisfying the local PT-symmetry and axial symmetry. We use this model to study the spatial effects of beam propagation in 1D, and 2D PT-axisymmetric structures. In Eq. (2.3), the temporal evolution of field is equivalent to propagation of the field along *z*-direction which can be described as:

$$\partial_z A(\vec{r},z) = i\,\nabla_\perp^2 A(\vec{r},z) + iV(\vec{r})A(\vec{r},z) \qquad (2.4)$$

2.4 1D Periodic PT-axisymmetric systems

We start considering a 1D PT-axisymmetric potential, see Eq. (2.1), $V(x) = n_{Re}\,cos(|x|+\phi) - in_{Im}\,sin(|x|+\phi)$. To perform the numerical analysis, we integrate the paraxial wave equation using the split-step scheme. We use a normalized Gaussian beam of initial width w_o in the form $A = e^{-(x/w_o)^2}$, and study the beam propagation through the modulated system. We expect such a system to develop a strong localization at *x*=0 after a sufficient propagation time, and for appropriate parameters, modulation amplitudes and phase. The localization of the field is also expected to follow an exponential temporal evolution (grow or decay) due to the linear nature of the system. Therefore, we may express the asymptotic solution of the propagated field envelops by the product of spatial and temporal exponents which can be expressed as: $A \approx e^{i\omega t}\ e^{ik|x|}$ where $k = k_{Re} + ik_{Im}$ and $\omega = \omega_{Re} + i\omega_{Im}$ are both complex quantities. The real and imaginary

components of the wavenumber, k_{Re} and k_{Im} represent the dominant spatial modes and the spatial localization (delocalization) exponent, respectively. Similarly, ω_{Re} and ω_{Im} denote the temporal oscillation frequency and temporal growth (decay) exponent, respectively. Our aim is to investigate the dynamics of such non-Hermitian systems to explore the parameter space (n_{Re} , n_{Im} , ϕ), and provide a comprehensive analysis of the field localization and enhancement regimes. The spatial localization exponent after a sufficient long time evolution, t, can be numerically calculated as:

$$k_{Im} = d/dx[ln(A(x,t))] \tag{2.5}$$

and respective temporal growth exponent, at x=0, as:

$$\omega_{Im} = d/dt[\ln(A(0,t))] \tag{2.6}$$

Therefore, these two quantities are the figures of merit used to identify and determine the performance of the field localization and enhancement regimes in the parameter space (n_{Re} , n_{Im} , ϕ).

2.4.1 Numerical results

We start our analysis for the 1D potential, for the particular situation ϕ=0. For this case, the potential profile shows inward coupling, and the field is expected to be localized around the symmetry center, $x = 0$, due to the unidirectional coupling on the left-hand $x < 0$ and right-hand $x > 0$ half-spaces. Moreover, we note that a high refractive index is located at x=0, surrounded by gain areas as shown in Fig. 2.1(a). The results for the 1D case for ϕ=0 are presented in Fig. 2.2. The field localization and growth maps are plotted in parameter space (n_{Re} , n_{Im}) in Figs. 2.2(a) and 2.2(b),

respectively. In both maps, the dark blue region represents nearly no localization and field growth. The axis lines, drawn on maps, define the different quadrants in parameter space. We observe that gain modulation plays a key role in field exponential growth that results in large growth for $|n_{Im}| > |n_{Re}|$. This is not so surprising because amplification of field is directly linked with gain irrespective of the system dynamics. However, we observe simultaneously large growths and strong localizations on the top-right quadrant ($n_{Re} > 0, n_{Im} > 0$), where the coupling is inward. This gives the optimal operating regime where both effects are more pronounced. More importantly, the localization effect is stronger along the diagonal line showing the crucial role of relative amplitudes of the real and the imaginary modulations as evident in Fig. 2.2(a).

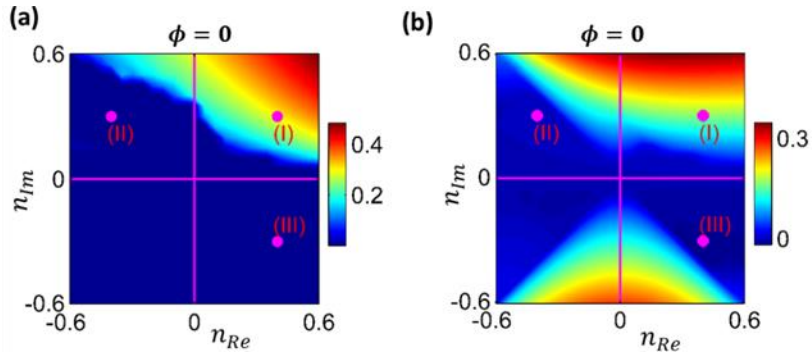

Figure 2.2. (a) Localization map, calculated after a sufficient long time (t~300 units) in the parameter space (n_{Re}, n_{Im}) for ϕ=0. (b) Growth map at the center ($x = 0$), in the parameter space (n_{Re}, n_{Im}).

It is also important to show the spatiotemporal dynamics of propagating field in such non-Hermitian structures. For this purpose, we consider three representative points, (I), (II) and (III) within and outside the field localization regime. The spatial profiles in linear and natural logarithmic

scales are provided along with corresponding spatial spectra for the considered points in Fig. 2.3.

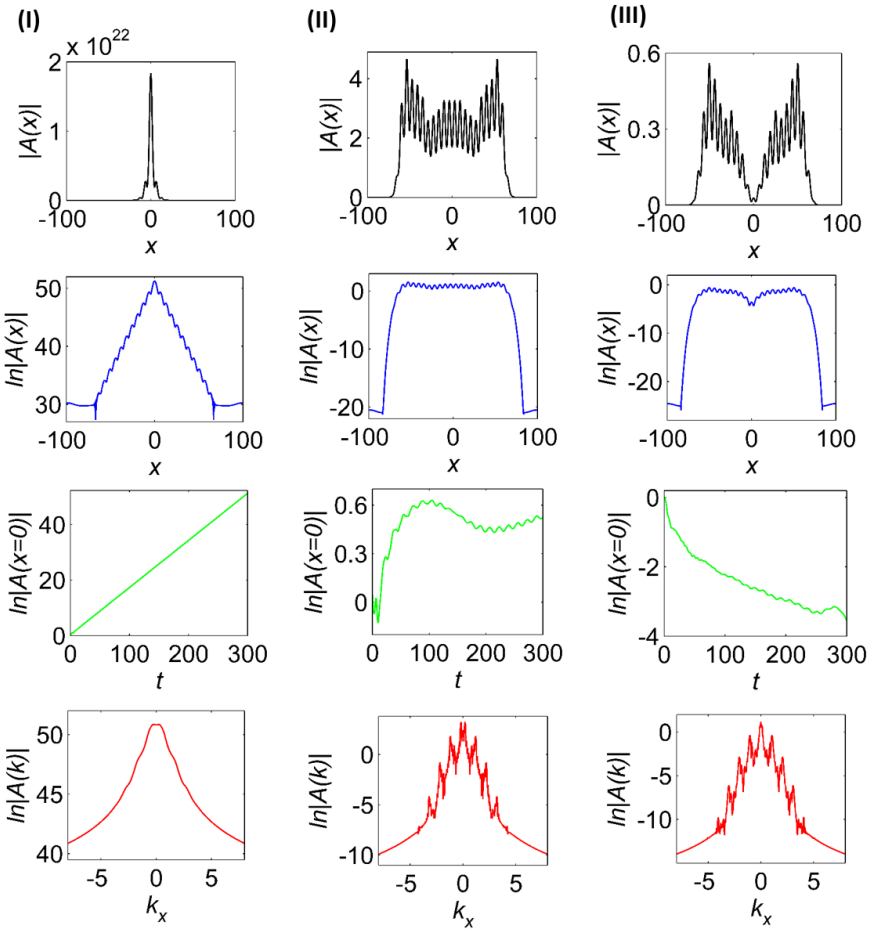

Figure 2.3. Spatiotemporal field dynamics for representative points marked as (I), (II), (III) in Fig.2.2 correspond to the parameter sets (0.4,0.3), (-0.4,0.3) and (0.4,-0.3), respectively. In all cases, the spatial field profiles in linear and logarithmic scale are shown on the first and second row, while the third and fourth rows represent the temporal evolution of the field at the center and the corresponding spatial field spectrum.

As expected, sharp localization is observed for point (I) when the coupling of wavevectors is inward. However, the field is distributed uniformly on space for point (II) and (III) due to outward field flows. A large slope in logarithmic spatial profile confirms the exponential localization effect in inward coupling case. In addition, this exponential slope hides the peaks of dominant spatial modes in Fourier spectrum (I). Therefore, we are unable to recognize the spatial modes participating in localization mechanism, while in (II) and (III), the participating modes are well recognized.

2.4.2 Phase dependent Localization regimes

In the previous section, we restrict our analysis to $\phi = 0$ but, in reality, the phase of the PT-axisymmetric potential decides index and gain-loss profiles at symmetry center, x=0. In this sense, the effect of phase on localization is crucial to have a deeper insight. We explore the parameter space (n_{Re} , n_{Im}) by systematically varying the phase from 0 to 2π and observe that localization regime changes to different quadrants of the parameter space depending on the phase value. We observe that intense localization regime spins counter clock to four quadrants of maps with increase in the phase. The localization maps for the representative phases: $\pi/4$, $\pi/2$, π and $23\pi/16$ are provided in Fig. 2.4 (a,b,c,d). These maps depict the complete picture with possible localization regimes for each phase and show how the strong localization regime flip to different quadrants of parameter space. For $\phi = \pi/4$, strong and weak localization regimes are observed in the first quadrant ($n_{Re} > 0, n_{Im} > 0$) and second quadrant ($n_{Re} < 0, n_{Im} > 0$) of the map, respectively. It is to be noted that strong localization still remains in first quadrant for $\phi = 0$. For $\phi = \pi/2$, strong localization flips to the second quadrant ($n_{Re} < 0, n_{Im} > 0$) where the system is almost PhC-like. Further increasing the phase, localization regime jumps to the third

quadrant($n_{Re} < 0, n_{Im} < 0$) for $\phi = \pi$. Note that this case is exactly symmetric to the one for $\phi = 0$. The strong localization appears in fourth quadrant ($n_{Re} > 0, n_{Im} < 0$) for $\phi = 23\pi/16$. The maximum localization exponent, $k_{Im,max}$, as a function of phase is also plotted in Fig. 2.4e(i). The vertical dashed lines indicate the boundaries that separate strong localization regime for different phases in four (i-iv) quadrant of parameter space. The potential profiles for representative points lying within strong localization regimes are shown in Fig. 2.4e(i-iv).

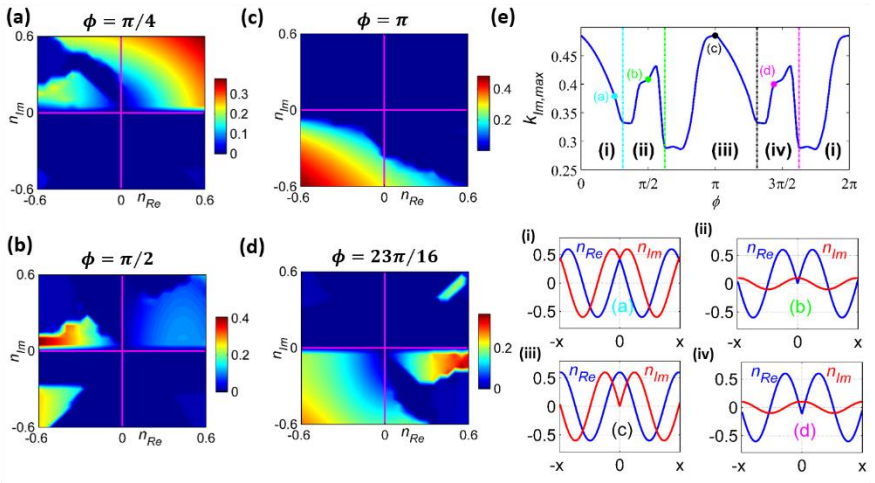

Figure 2.4. Dependence of localization regime on phase. Localization maps calculated after a sufficient long time (t~300 units) for different phases (a) $\phi = \pi/4$ (b) $\pi/2$ (c) π and (d) $23\pi/16$. Maximum localization exponent depending on phase ranges from 0 to 2π showing shift of strongest localization regime within four quadrants of the maps: (i) ($n_{Re} > 0, n_{Im} > 0$), (ii), ($n_{Re} < 0, n_{Im} > 0$) (ii) ($n_{Re} < 0, n_{Im} < 0$) and (iv) ($n_{Re} > 0, n_{Im} < 0$) and respective index and gain-loss potential profiles of representative phases for particular parameter sets.

The results indicate that localization phenomenon occurs in both PhC-like and GLM-like systems. In the GLM-like system, localization appears due

to inward coupling between wavevectors provided by local PT-symmetry. However, standalone axial symmetry can also localize the field at x=0 for some particular phase. In case of PhC-like system, the coupling is outward and localization is less significant than the GLM-like system, see a small island in Fig. 2.4(a). In this case, axial symmetry dominates the coupling behavior for the localization effect. Note that we characterize the system with the localization exponent, however, distribution of localized spatial profiles can be different depending on the modulation parameters. The intense localization appears for $\phi = 0, \pi$ in GLM-like systems.

2.4.3 Mode analysis using Laplace Transform

In this section, we analyze and interpret the different localization regimes systematically by determining spatial modes present in the field spectra. These regimes are appeared in the parameter space due to different mode dynamics which depends mainly on the phase and modulation amplitudes of potentials. In such non-Hermitian system, mode analysis is not so trivial due to intrinsic complex nature of spatial modes, i.e. $k = k_{Re} + ik_{Im}$. The most commonly used Fourier transform gives the complex spectrum of the real variable. Therefore, we observe a smooth profile of the spectrum and resonant peaks of growing modes are not noticeable as depicted in Fig. 2.3. To precisely determine the competing spatial modes in the spectrum, it is essential to calculate spectrum of the complex variable. In this scenario, Laplace transform is the most suitable method to calculate the spectrum of complex quantities [Mor08]. The unilateral Laplace transform can be defined for a function, $A(x)$, for all real values $x \geq 0$ as: $A(s) = \int_0^\infty A(x)e^{-sx}dx$ where $s = \sigma + ik$. The Fourier transform can be considered as a particular case of Laplace transform for $\sigma = 0$. In this sense, the Laplace transform is a much powerful tool compared to the Fourier

transform due to many intrinsic advantages. Among them, it is its less sensitive convergence due to the inclusion of an exponential decaying kernel, i.e. e^{-sx}, that makes it useful for the analysis of transient and unstable systems. Zeroes and poles of the Laplace transform denote critical frequencies with amplitudes, $A(s)$, going to zero or blowing up to infinity, respectively. To describe the difference between Laplace and Fourier transform, we consider a simple exponential decaying field in the form: $A(x) = e^{-(ik_{Re}-k_{Im})x}$ and calculate the corresponding Fourier transform as $A(k) = 1/[k_{im} + i(k_{Re} - k)]$ and Laplace transforms as $A(s = \sigma + ik) = 1/[(k_{Im} - \sigma) + i(k_{Re} - k)]$. In this particular example, a pole appears at $(\sigma, k) = (k_{im}, k_{Re})$ in the Laplace transform and the cross-section over the pole $\sigma = k_{im}$ gives a sharp peak. We numerically calculate the Laplace transform on the half plane, $k_{im} \geq \sigma$ and precisely locate the resonant peaks of spatial modes at $k_{im} \approx \sigma$, where σ represents the spatial localization calculated in our case from the exponential spatial slopes. We consider the representative points in all possible localization regimes for phases $\phi = 0, \pi/4, \pi/2$ and corresponding spectra are shown in Fig. 2.5. The three different spatial modes sets observed in spectra correspond to different localization regimes in PhC-like and GLM-like systems.

The simplest case is the PhC-like system, where leading modes are at the edge of Brillioun zone represented by a set of dominant integer modes: $k_x \approx 0, \pm 1, \pm 2$ for $\phi = \pi/2$. The other two localization regimes are present in GLM-like systems where leading modes are in the very middle of the Brillioun zone and have a set of half-integer dominant modes: $k_x \approx \pm 0.5, \pm 1.5, \pm 2.5$ ... corresponding to frequencies with the largest gain, this is the case for $\phi = \pi/4$ [see Fig. 2.5(b)]. However, the mode dynamics is more complex in GLM-like case, because both the index and gain-loss modulations strongly affect the coupling between harmonics.

Consequently, some configurations do not present the leading modes exactly at the middle of the Brillioun zone. We observe this situation for $\phi = 0, \pi$ when the system supports the dominant mode set: $k_x \approx \pm 0.3, \pm 0.7, \pm 1.7$. This mode analysis helps to differentiate the different localization regimes, existing either in PhC-like or GLM-like cases, and completely characterize the system dynamics.

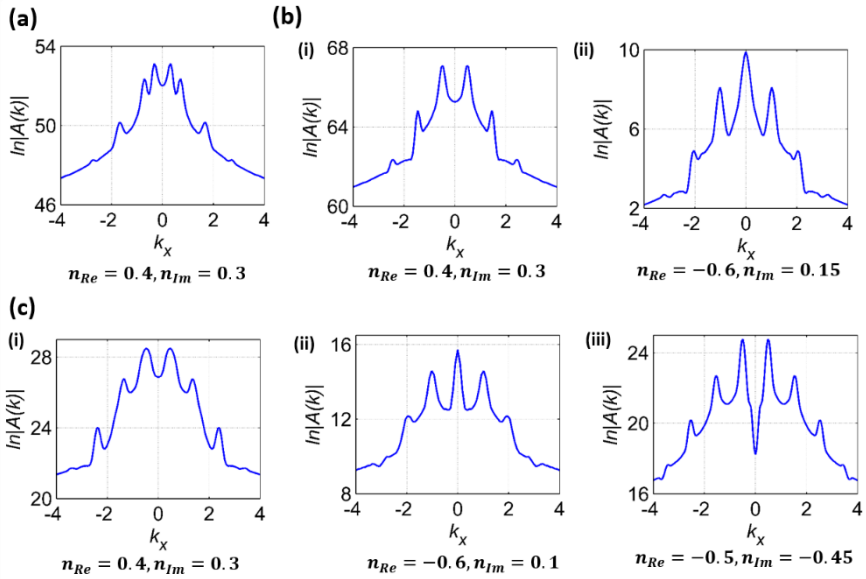

Figure 2.5. Spatial field spectrum as obtained from the Laplace transform, in logarithmic scale, for representative points within the field localization areas for (a) $\phi = 0$, (b) $\pi/4$ and (c) $\pi/2$. Three set of dominant modes are identified correspond to representative points. In (a) the dominant modes are $k_x \approx \pm 0.3, \pm 0.7, \pm 1.7, \ldots$ in (b) the dominant modes are (i) $k_x = \pm 0.5, \pm 1.5, \pm 2.5 \ldots$ and (ii) $k_x = 0, \pm 1, \pm 2, \ldots$; while in (c) the dominant modes are (i) $k_x \approx \pm 0.3, \pm 0.7, \pm 1.7, \ldots$, (ii) $k_x \approx \pm 0.5, \pm 1.5, \pm 2.5 \ldots$,and (iii) $k_x = 0, \pm 1, \pm 2$.

2.4 2D Periodic PT-axisymmetric systems

PT-axisymmetric potentials can be generalized to two- or higher spatial dimensions. In 2D, such harmonic potential has this form: $V(r) = n_{Re}\, cos(r+\phi) - in_{Im}\, sin(r+\phi)$. In this case, the transverse space has radial symmetry, but it can be also explored for other symmetries like square symmetry as well.

2.4.1 Numerical results

In the last section, we concluded that the optimal phase to observe strong localization and growth exponents for the 1D case is $\phi = 0$. Therefore, for 2D case we restrict our study to $\phi = 0$. We perform the numerical analysis for this 2D PT-axisymmetric system, and observe a strong field localization and enhancement around $r = 0$, due to the asymmetric coupling between radially incoming and outgoing propagation waves. Note that the cross-sectional profiles of the corresponding propagated field do not exactly exhibit exponential field slopes due to the axial symmetry. Therefore, first we, calculate the spatial field profile $A(r)\sqrt{r}$ and then calculate the localization exponent from its cross-section. Analogous to the 1D system, the parameter space is explored and the localization and growth exponents are encoded in color maps as shown in Fig. 2.6(a). We observe that regimes with simultaneously strong localization and enhancement exist in the top right quadrant of Figs. 2.6(a) and 2.6(b), similar to the 1D case. The spatial profiles, in linear and natural logarithmic scales, for representative set of parameters inside the localization regime area are shown in Fig. 6(c). The corresponding cross-sectional profiles in Fig. 2.6 c(iv-vii) show a sharp localization while the phase profile is provided in Fig. 2.6 c(iii). The spatial phase variation with jumps from $-\pi$ to $+\pi$, also confirms the inward coupling behavior that leads to localized enhanced fields. The results show

that the localization and enhancement regimes in 2D systems are compatible with 1D case. However, the 2D systems are more realistic for implementation and different arrangements can be realized to observe the localization effects in physical systems.

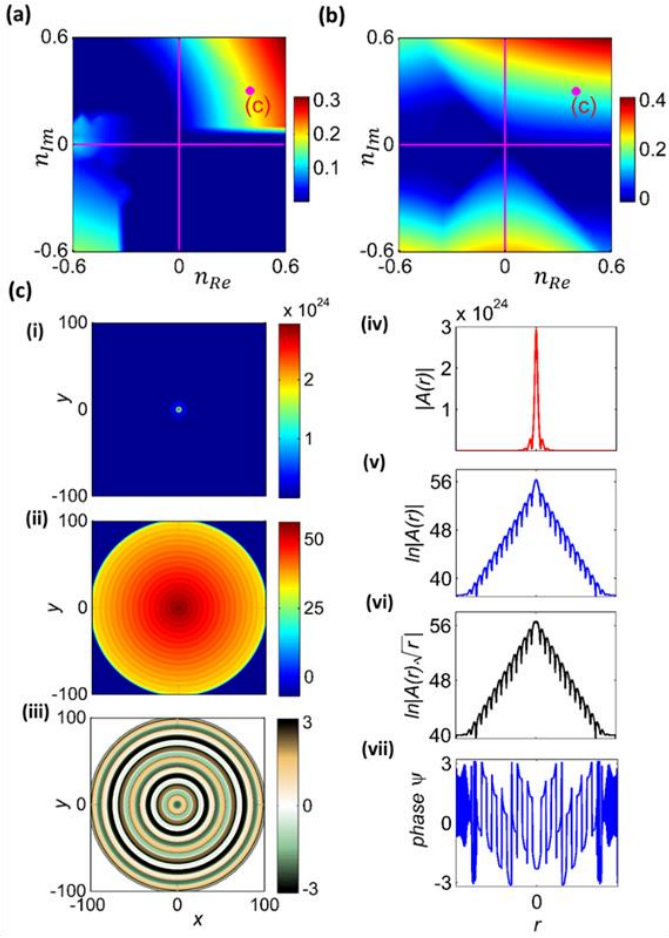

Figure 2.6. (a) Localization (k_{Im}) map of the axial cross-section profile of the field linearized as: $A(r)\sqrt{r}$ for a 2D PT-axisymmetric as in Fig. 2.1(b), calculated after sufficient long time (t~300 units) in parameter space (n_{Re}, n_{Im}). (b) Growth (ω_{Im}) map of the field at the center ($r = 0$) in parameter space. A strong field enhancement and localization at $r = 0$ is shown in (c) for the parameter set (0.4,

0.3). (i,ii) 2D spatial field profiles in linear and natural logarithmic scales, respectively. (iii) Field phase. Panels (iv),(v),(vii) display the axial cross-sectional profiles of (i)-(iii), whilst (vi) depicts the linearized field, $A(r)\sqrt{r}$, in natural logarithmic scale.

2.5 Noise effects in PT-axisymmetric systems

In the previous sections, we have considered an ideal situation without any external perturbation in the optical systems. However, we have not a complete control over external conditions in a realistic optical system, for instance, surface irregularities and the intensity fluctuations of the incident light could modify and deteriorate the field localization and field growth. More specifically, the dynamics of optical systems are very sensitive to the noise, and therefore it is important to study the proposed PT-axisymmetric systems in the presence of noise.

We consider a 1D PT-axisymmetric system and study the propagation of a Gaussian beam with different noise levels to check the robustness of the propagating beam. For convenience, we assume white noise and introduce it in the initial beam with a certain light wavelength, λ. The spatial field profiles after sufficient propagation are depicted in Fig. 2.7. We use the beam quality factor, M^2, defined as: $M^2 = W\theta\pi/\lambda$, to analyze the performance of the system, where W is the width of the beam and θ is its divergence. We observe that the noise level does not affect the output beam quality. The calculated beam quality for all considered parameters is quite universal, similar with a value of M^2=1.32, and characterizes the beam with an exponential slope (nongaussain). We would like to note that the beam shaping effect in a periodic gain-loss structure relies on the anisotropic amplification of modes with smaller wavevectors, rather than on the conventional mechanism of filtering out non desired modes with higher

wavevectors. Therefore, field localization and enhancement in proposed PT-symmetric systems is quite robust to external perturbations.

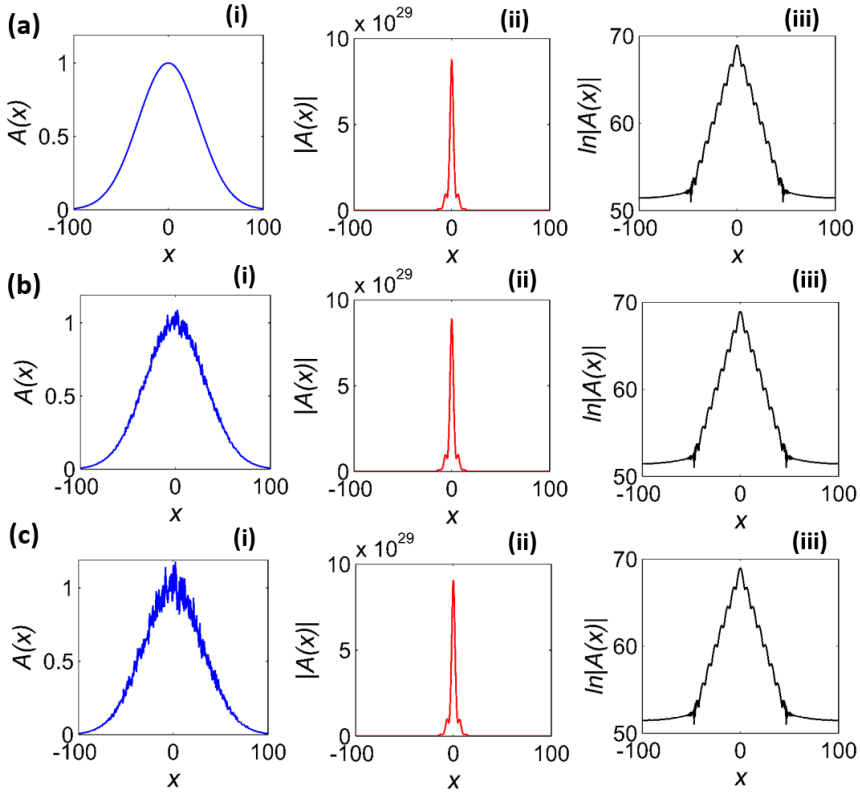

Figure 2.7. (a) Initial Gaussian beam without noise (b) noise level 5% (c) noise level 10%. In all three cases, the initial beam with M^2=17.77 and 15.39 is shown in (i), and the spatial field profile after long time in linear and logarithmic scale are depicted in (ii) and (iii), respectively. The calculated output beam quality is M^2=1.32, for all cases irrespective of the initial noise level.

2.6 Generalization of PT-axisymmetric potentials

Until now, we have only considered the PT-axisymmetric potential with the simple profile, the sinusoidal one. However, our idea is quite universal and

can be applied to any potential profile satisfying the local PT-symmetric and axial symmetry conditions. With the aim to illustrate inward coupling localization irrespective of the potential profile, we may consider other local PT-symmetric and axial symmetric potential profiles in the form: $V(x) = \sum 1/n\, e^{-inqx}$ where n is a positive integer. We would like to mention that asymmetry between $+q$ and $-q$ coefficients provides the directionality. Therefore, we consider the most asymmetric case corresponding to $V(x)$, where n is a positive integer to obtain a strong directionality. In this particular potential, we can generate the sawtooth and stepwise profiles for n =1,2,3,… and n =1,3,5,... respectively. We propagate the beam in such potentials and numerically show that the field localization and enhancement also occurs, as depicted in Fig. 2.8.

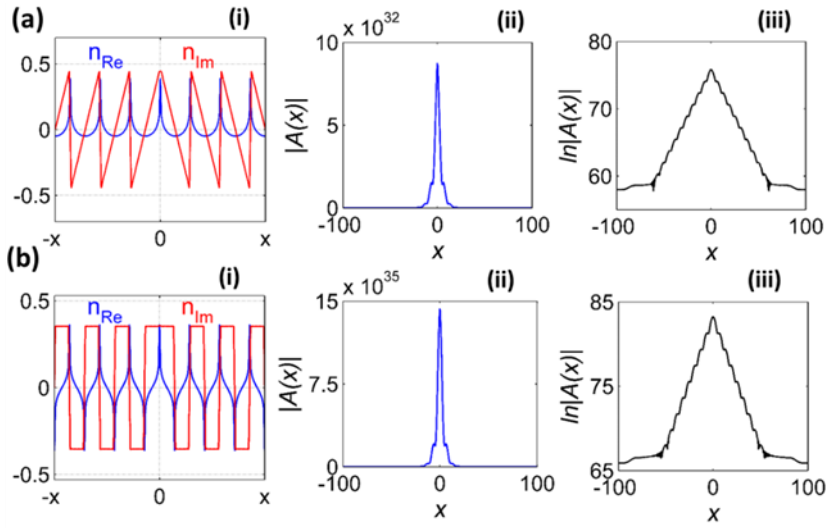

Figure 2.8. PT-axisymmetric potential profiles are shown in (i) and the spatial field profile in linear and logarithmic scales calculated after sufficient time are illustrated in (ii) and (ii), respectively for both cases.

The results indicate that field is localized at the origin, analogously to the

results provided in simple sinusoidal potential. Indeed, such potentials could be engineered in a variety of different ways for practical realization of the proposed effect.

2.7 Localization in quasi-periodic PT-symmetric systems

In the previous sections, we consider the periodic structures to show how local PT-symmetry and axial symmetry leads to strong localization due to asymmetric coupling between inward and outward propagating modes. In such structures, the axial symmetry creates the center for localization, and local PT-symmetry directs the light towards the center. Here, we are proposing another possible configuration for field localization using global PT-symmetry in quasi-periodic systems. The fundamental concept of localization is the same that is based on inward coupling mechanism. In the present situation, the quasi-periodicity naturally creates the localization centers and the complex potential holding global PT-symmetry directs the light towards these centers.

We consider a simple quasi-periodic potential satisfying the global PT-symmetry described as;

$$V(x) = n_{Re}\, cos(\, q_1\, x) + i n_{Im}\, sin(\, q_2\, x) \qquad (2.7)$$

where the modulation frequencies are q_1 and q_2 create a quasi-periodic potential. To simplify the analysis, we normalize $q_1 = 1$ and consider the $q_2 = 1 \pm dk$, where $dk \ll 1$ to get many periods between localization center as shown in Fig. 2.9(a).

The localization center created by quasi-periodicity is displayed by a circle while arrows show the direction of field flows that results in localization and enhancement of the field. The field profile after long time evolution in linear and natural logarithmic scales are shown in Figs. 2.9(b) and 2.9(c), respectively. The general conclusion is that we can exploit the PT-symmetry in many ways to observe the localization phenomena based on asymmetric coupling in periodic as well as quasi-periodic structures.

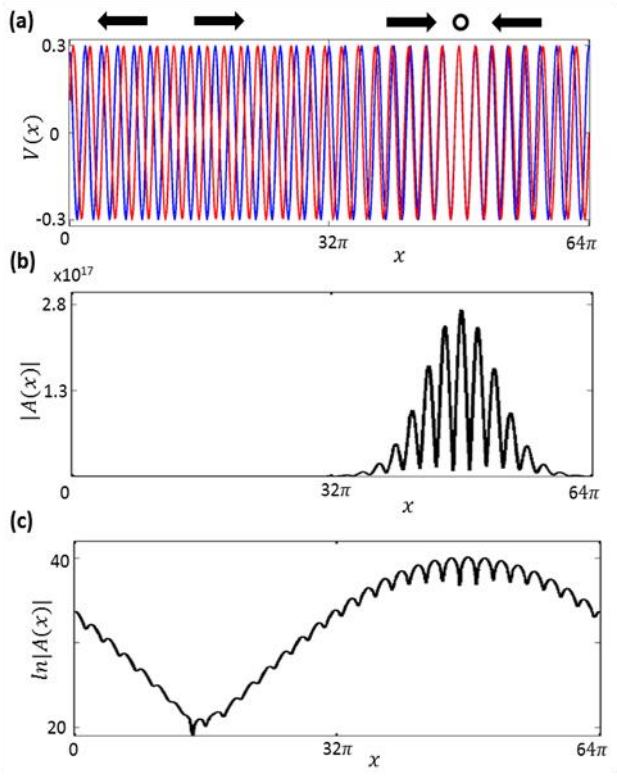

Figure 2.9. (a) Potential profile of quasi-periodic PT system with arrows to show the flow direction (b) spatial field profile in linear and (c) in logarithmic scale calculated after sufficient time. The normalized spatial frequencies $q_1 = 1$ and $q_2 = 0.9687$.

2.8 Conclusions

We propose a novel class of local PT-symmetric systems providing a unique platform for extreme field localization and enhancement around a selected point or area. Such systems have the capability to simultaneously localize and enhance the field due to the asymmetric radial coupling of inward and outward waves. Specifically, this new class of systems can strongly localize the field, depending on the relative modulation amplitudes and phase of the complex potential. We examine the effect of phase variation on localization and found different localization regimes in PhC-like ($n_{Re} > n_{Im}$) and GLM-like ($n_{Re} < n_{Im}$) systems. The localization regime spins counter-clockwise between the four quadrants of the parameter space (n_{Re}, n_{Im}) map by varying the phase from 0 to 2π. We interpret the existence of different localization regimes using the mode analysis, performed by the numerical Laplace transform of the complex field. The results give three different sets of leading spatial modes which belong to PhC-like case, i.e. $k_x = 0, \pm 1, \pm 2, \ldots$ and GLM-like case for $k_x \approx \pm 0.3, \pm 0.7, \pm 1.7, \ldots.$, $k_x \approx \pm 0.5, \pm 1.5, \pm 2.5$, doing few calculations we could deduce a general form for this modes: $k_x \approx n \pm a, n \in \mathbb{Z}, 0 < a < 1, a \in \mathbb{R}$. The localization is stronger for GLM-like, which can be attributed to the inward coupling mechanism. The most interesting scenario occurs for GLM-like systems, for which extreme field concentrations are achieved for a wide range of parameter sets, for $\phi = 0$, either in the proposed 1D or 2D axisymmetric configurations. Also for PhC-like systems, less significant field localizations are obtained for some particular potential phases. Besides, we also investigate the robustness of the localization mechanism. For this purpose, we incorporate the noise in an initial Gaussian beam and point out the maintenance of the output beam quality irrespective of the noise level. The results confirm the robustness of the proposed

localization mechanism in response to external perturbations. We also show that periodic PT-axisymmetric potential can be engineered in many ways for experimental implementation, for instance, sawtooth and stepwise profiles. In the last part, we show that localization based on inward coupling can also be realized in quasi-periodic systems. In such systems, global PT-symmetry directs the light towards the localization point which is intrinsically created due to quasi-periodicity of the system. The fundamental concept may also be easily implemented to find remarkable applications in various linear and nonlinear optoelectronic devices where a high degree of localization is essentially desirable such as optical switching in nanostructures, optical modulators, or broad aperture lasers and microlasers. In particular, it could be applied to improve the beam quality of emission from broad aperture lasers. Moreover, localization mechanism based on inward coupling is universal which can be realized in different physical systems ranging from acoustics to Bose-condensates and among others.

Chapter 3
Directionality Fields

In the previous chapter, we showed how local PT-symmetry, by breaking the space symmetry, may allow unidirectional flow of light along a particular direction in given spatial domains, either for one-dimensional (1D) or two-dimensional (2D) systems. We also showed how PT-axisymmetric potentials, holding only local PT-symmetry can lead to light concentration. Therefore, as an extension of the local PT-symmetry concept, we propose a theory we refer as *directionality fields* to manipulate the flows of the electromagnetic field (or another kind of wave). The proposed directionality fields provide a precise control over the dynamics of probe fields and mold their flow in an arbitrary configuration, based on nontrivial wave dynamics in non-Hermitian systems. Such directionality fields can be generated from given vector fields, $\vec{p}(\vec{r})$, with desired shapes and topologies, that is to say, we consider an arbitrary 2D vector field to define the local unidirectionality, following the vector field. We develop the mathematical framework to realize such directionality fields based on a modification in the centenarian Hilbert transform, referred as a *local Hilbert transform*. This derived mathematical tool allows building 2D (or higher-dimensional) directionality fields from any original background optical potential either representing an index or a gain-loss modulation (e.g. being regular, irregular, extended or localized). In particular, we study some

interesting cases of directionality fields in the form of a sink, a vortex, and a circular channel in either linear or nonlinear systems. We show that the proposed directionality fields can be observed in both paraxial and non-paraxial limits. Hence, this chapter focuses on such unique directionality fields that could open new perspectives to manipulate the waves in real physical systems.

3.1 Temporal Hilbert Transform and Kramers-Kronig relations

The Hilbert transform is an integral relation that transforms a given real-valued function $x(t)$ into another function $y(t)$, by convoluting $x(t)$ with the function $1/\pi t$. The Hilbert transform (and its inverse) connect the real and imaginary (imaginary and real) parts of a causal signal being also known as Kramers-Kronig (KK) relations. These relations are used to calculate the real part from the imaginary part (or vice versa) of response functions in physical systems. We start by inspecting the KK relations. We consider a dielectric susceptibility, χ_e, of a causal material. Causality requires that the system has zero response before applying any external field. Therefore, the susceptibility in time-domain can be expressed as:

$$\chi_{\mathrm{e}}(t) = \chi_e(t)\, H(t) \tag{3.1}$$

where $H(t)$ is the Heaviside function defined as:

$$H(t) = \begin{cases} 0 & t < 0 \\ 1 & t > 0 \end{cases} \tag{3.2}$$

Performing a Fourier, Eq. (3.1) becomes the convolution:

$$\mathcal{F}\{\chi_e(t)\} = \chi_e(\omega) * H(\omega) = \int_{-\infty}^{\infty} \chi_e(u)H(u-\omega)du \tag{3.3}$$

where $\chi_e(\omega)$ and $H(\omega)$ are Fourier transforms calculated as,

$$\chi_e(\omega) = \int_{-\infty}^{\infty} \chi_e(t)e^{-i\omega t}dt \tag{3.4}$$

$$H(\omega) = \int_{-\infty}^{\infty} H(t)e^{-i\omega t}dt = \frac{1}{2}\delta(\omega) + \frac{j}{2\pi\omega} \tag{3.5}$$

Inserting Eqs. (3.4) and (3.5) into Eq. (3.3) and after simplification, we get:

$$\chi_e(\omega) = \frac{1}{2}\int_{-\infty}^{\infty} \chi_e(u)\delta(u-\omega)du + \mathcal{P}\int_{-\infty}^{\infty} \frac{j\chi_e(u)}{2\pi(u-\omega)}du$$

$$\chi_e(\omega) = \frac{1}{2}\chi_e(\omega) + \frac{j}{2\pi}\mathcal{P}\int_{-\infty}^{\infty} \frac{\chi_e(u)}{(u-\omega)}du$$

$$\chi_e(\omega) = \frac{j}{\pi}\mathcal{P}\int_{-\infty}^{\infty} \frac{\chi_e(u)}{(u-\omega)} \tag{3.6}$$

where $\mathcal{P}$ represents Cauchy principal value, to avoid the poles of the integral, at $u = \omega$. Equation (3.6) describes the frequency response of a causal material being invariant under a Hilbert transformation. We can easily obtain the Kramers-Kronig relations by rewriting Eq. (3.6) with

complex dielectric susceptibility in frequency domain, i.e. $\chi_e(\omega) = \chi_{Re}(\omega) + j\chi_{im}(\omega)$ and the results are:

$$\chi_{Re}(\omega) = \frac{1}{\pi}\mathcal{P}\int_{-\infty}^{\infty}\frac{\chi_{im}(u)}{(u-\omega)}du \tag{3.7a}$$

$$\chi_{im}(\omega) = -\frac{1}{\pi}\mathcal{P}\int_{-\infty}^{\infty}\frac{\chi_{Re}(u)}{(u-\omega)}du \tag{3.7b}$$

the imaginary part of the complex dielectric susceptibility χ_e. By imposing the causality condition on the Fourier transform of the susceptibility, we obtain: $\chi_e(-\omega) = \chi_e^*(\omega)$. It implies that $\chi_{Re}(\omega)$ and $\chi_{im}(\omega)$ are even and odd function of dielectric susceptibility, respectively. Hence, the relations may also be expressed as:

$$\chi_{Re}(\omega) = \frac{2}{\pi}\mathcal{P}\int_{0}^{\infty}\frac{u\chi_{im}(u)}{(u^2-\omega^2)}du \tag{3.8a}$$

$$\chi_{im}(\omega) = -\frac{2\omega}{\pi}\mathcal{P}\int_{0}^{\infty}\frac{\chi_{Re}(u)}{(u^2-\omega^2)}du \tag{3.8b}$$

3.2 Modified Spatial Hilbert Transform

In the previous section, we review the derivation of the pair of Hilbert transforms defining the Kramers-Kronig relations of a causal material. However, these relations may be also expressed in the spatial domain, just by replacing the time (t) with space (x). In image processing field, the spatial Hilbert transform is extensively studied for image edge detection

and enhancement [Han96, Dav00, Guo06]. Recently, Horsley et al. discovered that the spatial Kramers-Kronig relations are precisely the general mathematical relations between real and imaginary parts of complex refractive index of a new family of reflectionless non-Hermitian potentials [Hor15]. Therefore, in such potentails, the spatial refractive index and gain-loss profiles are related to one another by a Hilbert transform. In the same way that Kramers-Kronig relations in time warrant invisibility of the past, the Kramers-Kronig spatial relations modify the wave scattering to get unidirectional invisibility, that is to say, suppressing scattering in one direction [Lon16, Hor16, Kin17a, Kin17b, Hor17]. Following this idea, a systematic approach based on generalized Hilbert transform was recently proposed for the invisibility of an arbitrary object [Hay18]. Jiang et al. experimentally designed such a spatial Kramers-Kronig profiled metamaterial structure for broadband perfect absorption [Jia17]. Precisely following this ideas, we propose using a spatial Hilbert transform to control the field flow to a given direction based on the material properties. It is important to mention that the idea of building non-Hermitian potentials from Spatial Hilbert transform is not equivalent to a complex coordinate transformation to derive material properties, as in conformal mapping and transformation optics [Pen06, Leo06, Che10, Xu15]. The proposal is based on a different scheme, the Spatial Kramers-Kronig relations, which, always allows using non-magnetic materials. Finally, the present study may contribute to provide a physical insight to understand the wave propagation in the complex artificial systems.

To illustrate how the spatial Hilbert transform modifies the spectral properties, we consider a random background real potential, $n(x)$, and its spatial and its spatial Fourier transform, $n(k_x)$, is shown in Fig. 3.1(a). The spatial propagation symmetry can be maximally broken if the spectra

is set to zero either on the left or right half-axis, k_x. Mathematically, this can be achieved by adding the following spectrum, $m(k_x)$, to the initial potential spectrum, $n(k_x)$:

$$m(k_x) = n(k_x) \cdot p \cdot sgn(k_x) \tag{3.9}$$

where sgn is the signum function and p = ±1, determines the asymmetry in the spectrum of the resultant potential in Fourier domain: $U(k_x) = n(k_x) + m(k_x)$. For $p = +1$, negative frequencies are suppressed on $U(k_x)$, showing only a positive spectrum. On the contrary, for $p = -1$, $U(k_x)$ will have only a negative spectrum. The antisymmetric spectral profiles of $m_{\pm}(k_x)$ for $p = \pm 1$ are shown in Figs. 3.1(c) and 3.1(d). The obtained positive and negative spectra for the final potential $U_{\pm}(k_x)$ with $p = \pm 1$ are also shown in Figs. 3.1(e) and 3.1(f), respectively. The asymmetry in the spectrum predicts that the obtained potentials are actually complex functions in real space, U.

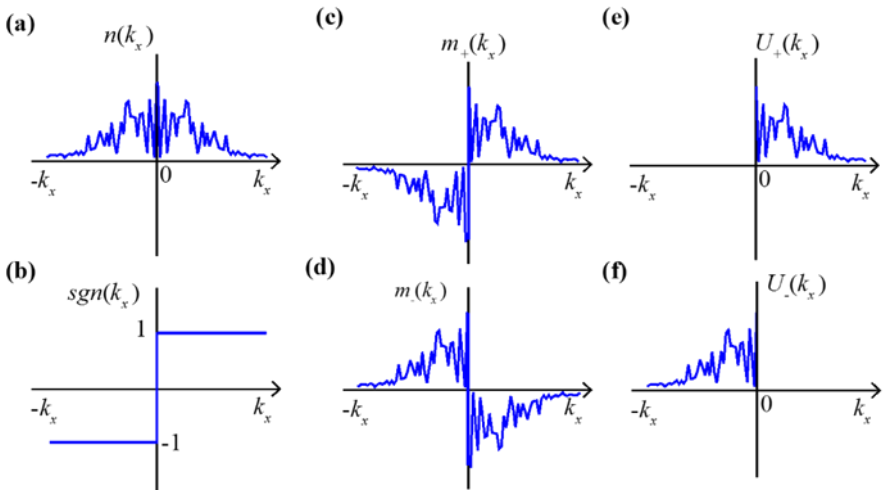

Figure 3.1. (a) Spatial spectrum of a random background potential (b) sign function

(c,d) antisymmetric spectral part of potential $m_{\pm}(k_x)$ for $p = \pm 1$ (e,f) final potential spectra $U_{\pm}(k_x)$ for $p = \pm 1$.

Therefore, the spectrum of the potential has both a symmetric, $n(k_x)$, and an antisymmetric, $m(k_x)$, part. The symmetric part of the spectrum corresponds to the initial real-valued potential, while the antisymmetric part of the spectrum (with the sign function) determines the imaginary part of the potential in real space.

At this point, we note that the inverse Fourier transform of Eq. (3.9) is related to the Hilbert transform: the convolution (inverse transform of the product in real space) of a real-valued function (of x) and the function $1/\pi t$. Thus, we define a modified Hilbert transform, in real space, as the convolution of the real potential and the inverse Fourier transform of the sign function, as the operator:

$$m(x) = \frac{p}{\pi}\mathcal{P}\int \frac{n(x_1)}{x - x_1}dx_1 \tag{3.10}$$

by introducing the directionality factor, p, to control the left/right scattering, which is absent in the conventional Hilbert transform. Note that the inverse Fourier transform of the sign-function is $\sqrt{2/\pi}\cdot i/x$, and the convolution in Eq.(3.10) in 1D introduces the factor $(2\pi)^{-1/2}$; also $\mathcal{P}$ stands for the Cauchy principal value of the integral. In turn, the inverse modified Hilbert transform can be written as:

$$n(x) = \frac{-p}{\pi}\mathcal{P}\int \frac{m(x_1)}{x - x_1}dx_1 \tag{3.11}$$

For consistency, the direct and inverse modified Hilbert transforms $H * H^{-1}$ can be calculated by applying sequentially Eq. (3.10) and Eq. (3.11):

$$m(x) = \frac{p}{\pi}\mathcal{P}\int \frac{n(x_1)}{x - x_1}dx_1 = \frac{-p^2}{\pi^2}\mathcal{P}\int \frac{dx_1}{(x - x_1)(x_1 - x_2)}dx_1 dx_2 \quad (3.12)$$

Since the relation $\frac{1}{\pi^2}\mathcal{P}\int \frac{dx_1}{(x-x_1)(x_1-x_2)} = -\delta(x - x_2)$ holds, the sequentially direct- and inverse modified Hilbert transform results in the identity operator as for the conventional Hilbert transform. This modified Hilbert transform ensures the maximum spatial asymmetry in response of the system of the non-Hermitian potentials. However, Hilbert transform is valid for the PT-symmetric potentials at the so-called PT-phase transition point (but not vice versa).

3.3 Proposed Local Spatial Hilbert Transform

We have discussed in the previous chapters that non-Hermitian systems may support asymmetrical coupling between propagating modes when the PT-symmetry condition is satisfied. The most interesting situation occurs at the exceptional point where two propagation modes coalesce leading to unidirectional behavior. Inspired by this unidirectionality property, we proposed the idea of local PT-symmetry in Chapter 2. This local PT-symmetry may provide the localization of the field at the boundary of two domains, the symmetry center, in the 1D configuration, by favoring the inward flow of left-propagating waves, and right-propagating waves, in the right and left half-domains, respectively. We also showed that this same idea could further be applied to higher dimensions with PT-axisymmetry. Here, we extend and generalize the idea of local PT-symmetry to general complex non-Hermitian systems either being regular or random, for the

control of the field flows in desired configurations. In particular, we propose a new approach to build non-Hermitian potentials that can favor unidirectional flows by breaking the mode coupling symmetry locally, in 1D or in higher dimensions. For the simplest 1D system, such unidirectional potentials may favor the energy flow towards selected positions which could be used to build sources and sinks in the spatial domain, as shown in Fig. 3.2(a). In 2D or higher dimensional systems, such local control of field flows offers a flexible and rich topological map of possibilities. We shall start by any arbitrary vectorial field $p(\vec{r})$ and construct the unidirectional potentials by assigning the directionality following the vector field $p(\vec{r})$, at each point (x, y) in two or (x, y, z) in three dimensions. In other words, we can generate the directionality fields to direct the light with any given topological configuration. For example, they can be applied to create the sinks for probe fields (for instance to increase absorption of probe fields at the sink), vortices and closed circular channel in probe fields as shown in Fig. 3.2(b,c,d).

The proposed vectorial potentials, hold the PT-symmetry condition only locally, in the entire spatial domain. Therefore, working exactly on the local exceptional point can allow a precise control over the field flow sense, enabling the generation of arbitrary directionality fields. This proposed novel family of non-Hermitian potentials can lead to a novel and nontrivial wave dynamics. Physically, such directionality fields have special significance, becoming relevant for applications in many linear and nonlinear systems.

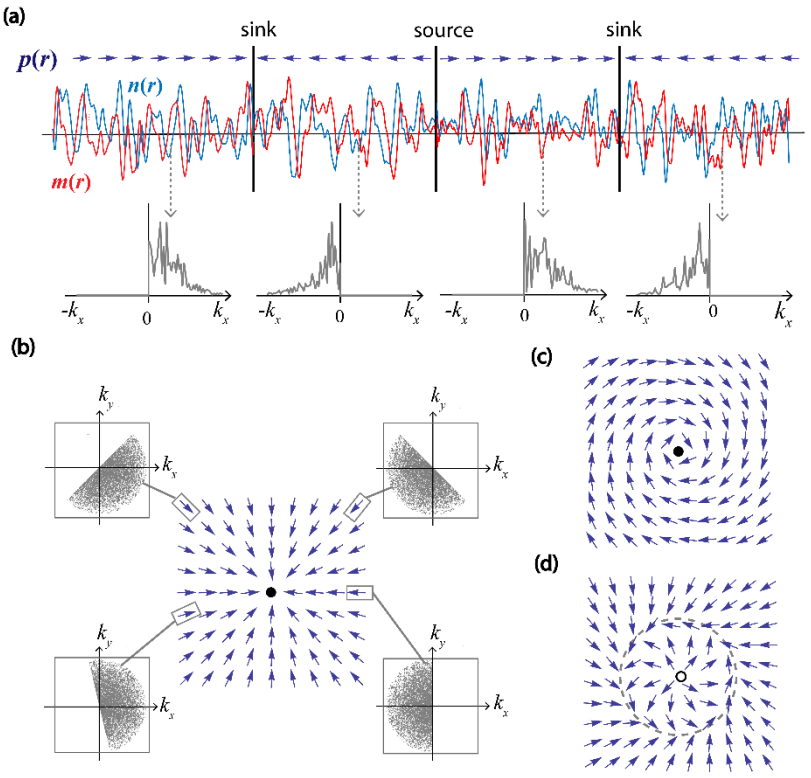

Figure 3.2. Unidirectional PT-vector fields. (a) 1D directionality field consisting of spatial domains of different parity containing sinks and sources between the domains. The first row represents the Fourier spectrum for the corresponding unidirectional complex potential [real part (blue), imaginary part (red)] provided in the second row for different unidirectionality (b) unidirectional vector field in two spatial dimensions in form of a focus, which eventually creates the sink for the probe field. The insets show the Fourier transforms of the unidirectional potentials at several points. (c) Unidirectional vector field in form of a node resulting in vortices of the probe field. (d) More complex unidirectional chiral vector field creating a circular flow channel for the probe field. In all cases, the vector fields, $\vec{p}(\vec{r})$, are denoted by the dark blue arrows.

3.4.1 1D Spatial Local Hilbert Transform

In this section, we derive relations for 1D spatial local Hilbert transform to generate the vectorial potentials. In order to introduce the local unidirectionality, we must consider some measure of directionality. In the simplest 1D case, for instance for those containing domains of alternating directionality as shown in Fig. 3.2(a), one should introduce the local function of the directionality, therefore, the parameter p becomes space-dependent $p(x)$. We assume a scalar function $p(x)$ which would equal ± 1 for right/left unidirectionality, respectively. Thus, a uniform unidirectionality $p(x) = const = \pm 1$ can be constructed with the help of a pair of the spatial Hilbert transforms:

$$m(x) = \frac{1}{\pi}\mathcal{P}\int \frac{p(x)n(x_1)}{x - x_1}dx_1 \tag{3.13}$$

and the inverse:

$$n(x) = \frac{-1}{\pi}\mathcal{P}\int \frac{p(x_1)m(x_1)}{x - x_1}dx_1 \tag{3.14}$$

connecting two quadratures of the complex potential. Such quadratures can be, for instance, the real and imaginary part of the refractive index in Optics. The spatial Hilbert transform ensures the suppressions of either the left- or right-scattering by the corresponding potential, depending on the sign of p. Note that the directionality function $p(x)$ enters into Eq. (3.13) and in Eq. (3.14) in different ways: in Eq. (3.13) it enters after the integration, and in Eq. (3.14) – before the integration. The symmetric shape of the pair of Hilbert transform would result in the following integral on $\int \frac{p(x_1)dx_1}{(x-x_1)(x_1-x_2)}$ checking the direct- and inverse Hilbert transform sequentially. The above

integral does not lead to $\delta(x - x_2)$ function for noncontinuos $p(x_1)$. Note that $p(x_1)$ is not continuous at the sink and source points.

Equations (3.12) and (3.13) written in symbolical operator form read: $m(x) = \hat{H}\hat{P}n(x)$, and $n(x) = \hat{P}\hat{H}^{-1}m(x)$, where $\hat{H}$ is the Hilbert operator (i.e. setting of half-spectra to zero) and $\hat{P}$ is the directionality operator (saying which half of spectra to set to zero). Calucltion of the sequentially direct- and inverse Hilbert transform result either in $m(x) = \hat{H}\hat{P}\hat{P}\hat{H}^{-1}m(x)$, or in $n(x) = \hat{P}\hat{H}^{-1}\hat{H}\hat{P}n(x)$. Since $p(x)^2 = 1$, then both direct- and inverse Hilbert transforms result in unity relations. In contrary, the direct- and inverse Hilbert transform in symmetrical case would lead to operators $\hat{H}\hat{P}\hat{H}^{-1}\hat{P}$ and $\hat{H}^{-1}\hat{P}\hat{H}\hat{P}$ which, in general, are not unity operators if $\hat{H}$ and $\hat{P}$ do not commute.

3.4.2 2D Spatial Local Hilbert Transform

In 2D systems, we define the directionality by a vector, $\vec{p}$, with the norm $|\vec{p}| = 1$. The background potential, $n(\vec{r})$, is also defined in 2D space, and its Fourier image: $n(\vec{k}) = \frac{1}{2\pi}\int n(\vec{r})exp(-i\vec{k}\vec{r})d\vec{r}$. Then the directionality can be achieved by setting a corresponding half-plane of spectrum $n(\vec{k})$ to zero, which mathematically reads:

$$m(\vec{k}) = n(\vec{k}) \cdot sgn(\vec{k} \cdot \vec{p}) \tag{3.15}$$

The Fourier transform of $sgn(\vec{k} \cdot \vec{p})$ reads: $2i\delta(\vec{r} \cdot \vec{q})/\vec{r} \cdot \vec{p}$, where $\vec{q}$ is the unit vector orthogonal to the given field of directionality: $\vec{q} \cdot \vec{p} = 0$, and $|\vec{q}| = 1$. The Hilbert transform then follows directly:

$$m(\vec{r}) = \frac{1}{\pi}\mathcal{P}\iint \frac{\delta\big((\vec{r}-\vec{r}_1)\cdot\vec{q}\big)n(\vec{r}_1)}{(\vec{r}-\vec{r}_1)\cdot\vec{p}}d\vec{r}_1 \tag{3.16}$$

$$n(\vec{r}) = \frac{-1}{\pi}\mathcal{P}\iint \frac{\delta\big((\vec{r}-\vec{r}_1)\cdot\vec{q}\big)m(\vec{r}_1)}{(\vec{r}-\vec{r}_1)\cdot\vec{p}}d\vec{r}_1 \tag{3.17}$$

Equations (3.16) and (3.17) correspond to the Hilbert transform for a uniform directionality. In order to write the final result for local Hilbert transform in 2D, we assume that the fields $\vec{p}(\vec{r})$ and $\vec{q}(\vec{r})$ are functions of space, same as in the 1D case. Then, the corresponding formulas read:

$$m(\vec{r}) = \frac{1}{\pi}\mathcal{P}\iint \frac{\delta\big((\vec{r}-\vec{r}_1)\cdot\vec{q}(\vec{r}-\vec{r}_1)\big)n(\vec{r}_1)}{\vec{p}(\vec{r})(\vec{r}-\vec{r}_1)}d\vec{r}_1 \tag{3.18}$$

$$n(\vec{r}) = \frac{-1}{\pi}\mathcal{P}\iint \frac{\delta\big((\vec{r}-\vec{r}_1)\cdot\vec{q}(\vec{r}_1)\big)m(\vec{r}_1)}{\vec{p}(\vec{r}_1)(\vec{r}-\vec{r}_1)}d\vec{r}_1 \tag{3.19}$$

Here $\vec{q}(\vec{r})$ is the field orthogonal to the given directionality field: $\vec{q}(\vec{r})\cdot\vec{p}(\vec{r}) = 0$, and $|\vec{q}(\vec{r})| = 1$. Analogously to the 1D case, previously explored, the sequence of direct- and inverse Hilbert transform using asymmetric pair Eq. (3.18) and Eq. (3.19) leads to the unity relation, and thus ensures compatibility. Note that, technically, they become effectively 1D integrals due to the presence of the Kronecker-delta function in the integrals.

3.4 Mathematical model

To study the dynamics of directionality fields, we consider a paraxial field equation in the normalized form as:

$$\partial_t A(\vec{r},t) = i\nabla^2 A(\vec{r},t) + iU(\vec{r})A(\vec{r},t) \tag{3.20}$$

where $A(\vec{r},t)$ is the slowly varying electric field envelope distributed in the 2D space, $\vec{r}=(x,y)$, and evolving in time, t, and $U(\vec{r})=n_{re}(\vec{r})+in_{im}(\vec{r})$ is a complex potential in two-dimensional space generated from arbitrary vector field of directionality, $\vec{p}(\vec{r})$. Here, $n_{re}(\vec{r})$ is the initial considered background pattern, and $n_{im}(\vec{r})$ is the constructed imaginary part of the potential using proposed local Hilbert transform. We note that Eq. (3.19) is analog to the longitudinal propagation of the field (in z) with the transverse potential $U(\vec{r})$ only by replacing the temporal coordinate, t, by the longitudinal coordinate, z.

3.5 Directionality fields in linear systems

In order to design directionality fields, the general procedure is to start with a given vectorial field $\vec{p}(\vec{r})$ to direct the flow of light, as shown in Fig. 3.2. Next, consider any initial background potential $n(\vec{r})$, for instance being real, but a complex one could more generally be considered (by including optical gain and losses). Then, the spatial profile of the gain-loss function, $m(\vec{r})$, is constructed from the initial refraction index profile $n(\vec{r})$, using the proposed local Hilbert transform. Finally, in order to verify the idea, we numerically solve Eq. (3.20) using the split step method. We explore different configuration for the directionality fields that demonstrate the flexible functionality of our proposal.

3.5.1 Temporal evolution in Sink vector fields

In this section, we consider simple vector field in the form of a sink or a focus, $\vec{p}(\vec{r})=-\vec{r}/|\vec{r}|$ [see Fig. 3.2(b)], and perform a detailed study of the sink directionality field for different spatially extended and localized patterns. We start with real periodic potentials in the form of hexagonal, octagonal and decagonal patterns and construct the corresponding

imaginary parts using proposed local Hilbert transform, for the sink vector field. We consider an initial Gaussian beam at an arbitrary position, in 2D space, and propagate it through the modified structure to observe the flow of the probe field. Initially, the propagated field shows a transient state which finally evolved to the stationary state, after a sufficient evolution time. In the transient state, the field is spread, while in the stationary state, it is localized around the center, $r = 0$. Due to the linearity of the system, the field grows in time while maintaining its spatial profile. The numerical results for periodic non-Hermitian potentials are presented in Fig. 3.3.

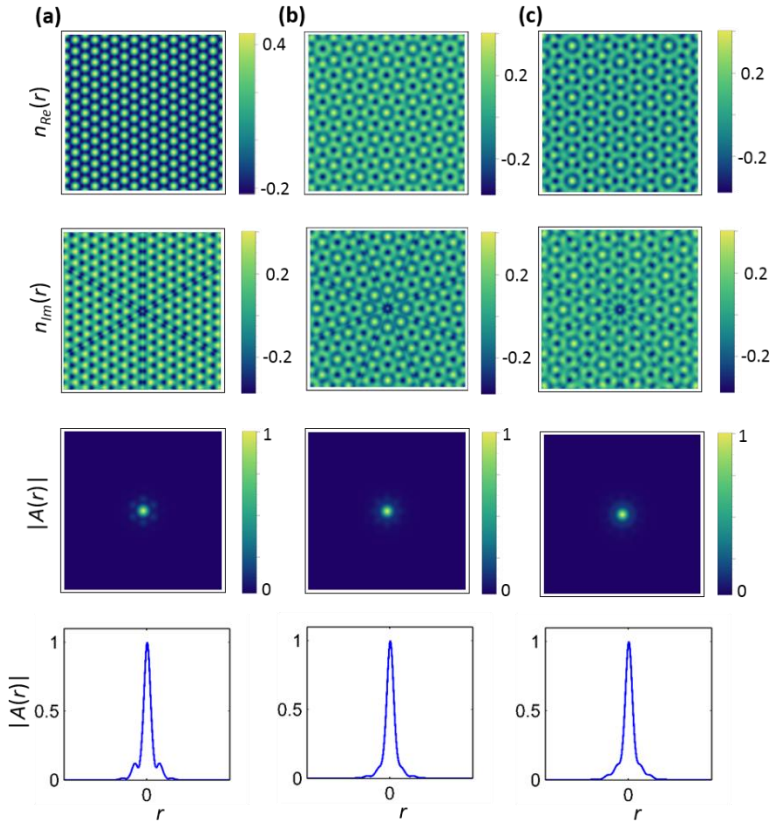

Figure 3.3. Probe field evolution in sink directionality field (the one shown on Fig. 3.2(b)) generated from the real-valued background potential with different regular

patterns such as: (a) hexagonal (b) octagonal, (c) decagonal. The upper row depicts the real part of the background potential, $n_{re}(\vec{r})$, the second row the corresponding imaginary part of the potential generated by the local Hilbert transform, $n_{im}(\vec{r})$, the thrid row shows the normalized final distributions of the probe field after sufficiently long time and and the bottom row shows the corresponding cross-sectional profile of the field.

We normalize the field during propagation in all cases, for representation. The bottom row shows the cross-sectional profile of the localized field in Fig. 3.3. We also asses the robustness and flexibility of the method. The results clearly indicate that field is sharply localized at the center irrespective of the initial periodic potential profile. Besides, we note that the localization phenomenon can be observed for any arbitrary position of the initial probe field.

Next, we consider different localized patterns to investigate sink directionality fields. The localized pattern can be generated by truncating the infinite pattern. We perform the same procedure to generate non-Hermitian localized potentials for three different finite patterns [see Fig. 3.4)]. The numerical results for the propagation of probe field, after sufficient evolution time, are presented in the third row and corresponding cross-sectional profile in the last row of Fig. 3.4. The dynamical behavior of field flow remains same as in the periodic case, showing initially spreading of the field in the transient state and, then, finally the localization at the center. The results confirm the sink behavior in localized patterns irrespective of initial profile.

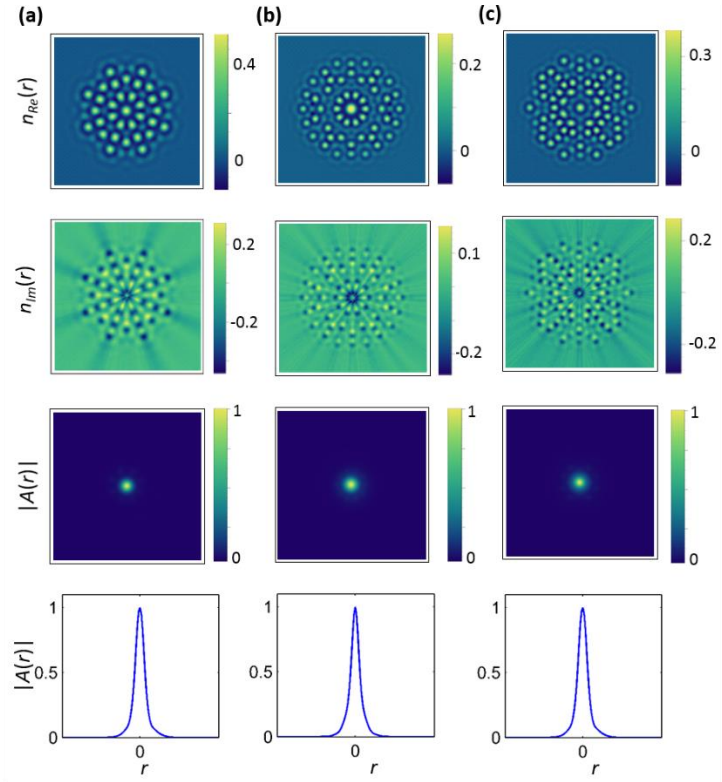

Figure 3.4. Probe field evolution in a sink directionality field generated from real-valued background potentials with differently localized patterns. The upper row depicts the real part of the background potential, $n_{re}(\vec{r})$ and the second row the corresponding imaginary part of the potential generated by the local Hilbert transform, $n_{im}(\vec{r})$. Thrid row shows the normalized final distributions of the probe field after sufficiently long time and and the bottom row shows the corresponding cross-sectional profile of the field.

Finally, we consider random patterns to analyze sink directionality fields. The random patterns can be generated in a variety of ways. For our analysis, we generate the pattern from initial white Gaussian noise. First, we study a pattern with spatial spectrum in the form of a solid disk, a common example of random structures [see the first two rows of Fig 3.5(a)]. On the other

hand, a random pattern can be generated from modulation wavevectors lying on a ring in reciprocal space, so-called generalized Bessel distributions [see the first rows of Fig. 3.5 (b) and 3.5(c)]. The numerical results for such random patterns are shown in the two lower rows of Fig. 3.5. Similar to periodic and localized potential cases, the results indicate that sink directionality fields are also possible to observe in non-Hermitian random potentials. We consider different thickness for the *k*-space ring in the spatial spectrum of the generalized Bessel distribution. The results confirm the localization at the center for both cases as shown in Figs. 3.5 (b) and 3.5(c).

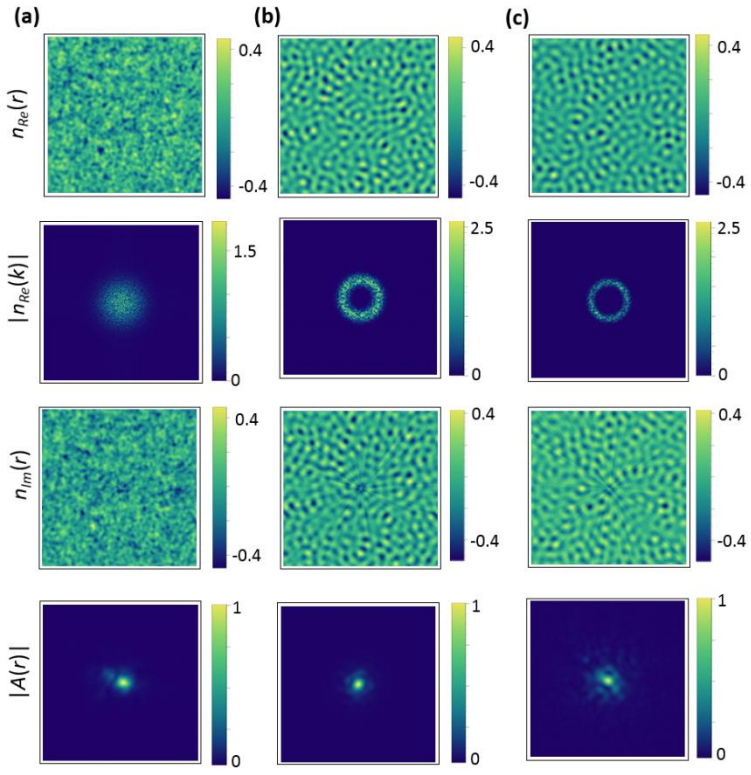

Figure 3.5. Probe field evolution in a sink directionality field generated from real-valued background potentials with random patterns such as: (a) random (b,c)

generalized Bessel distributions. The upper row depicts the real part of the background potential, $n_{re}(\vec{r})$, the second row the corresponding spatial spectrum of the potential. the third row the corresponding imaginary part of the potential generated by the local Hilbert transform, $n_{im}(\vec{r})$, the bottom row shows the normalized final distributions of the probe field after sufficiently long time.

We note the robustness of the mechanism, as localization occurs irrespectively of the initially chosen probe field position. We confirm that different background configurations, being periodic, quasi-periodic random, or localized lead to similar localization distributions, with small differences due to different symmetries of the background potential.

3.5.1 Temporal evolution in Chiral vector fields

Next, we consider more exotic directionality fields constructed from a vortex and a circular channel vector fields, which may result useful for micromanipulation of light for applications. We define a superposition of vortex with a sink by the vector field expressed as: $\vec{p}(\vec{r}) = -(\alpha\vec{r} + \beta\vec{r} \times \vec{e}_z)/|\alpha\vec{r} + \beta\vec{r} \times \vec{e}_z|$, and a circular channel flow as $\vec{p}(\vec{r}) = (\alpha(|\vec{r}| - 1)\vec{e}_r + \beta\vec{r} \times \vec{e}_z)/|\alpha(|\vec{r}| - 1)\vec{e}_r + \beta\vec{r} \times \vec{e}_z)|$. In both expressions, $\vec{e}_z$, $\vec{e}_r$, and $\vec{e}_\varphi$ stand for the unit basis vectors in polar coordinates, and α and β correspond to the radial and azimuthal part of the flow, respectively. The results for both cases are provided in Fig. 3.6. The final spatial field distributions in the second column indicate that the probe field drifted towards the center and follows vortex and circular channel vector fields. In vortex case, the zero intensity in the center of field profile clearly confirms the phase singularity depicted in the third column of Fig. 3.6(a). We also calculate the field flows using the relation: $-i(A^*\nabla A - A\nabla A^*)$, where A is the final state of the probe field after sufficient time evolution, shown in the last column of Fig. 3.6. The field flow clearly confirms the chiral behavior

of the vortex and circular channel directionality fields. The evolutions of the field towards the final state in the considered chiral cases is also robust and weakly dependent on the background potential as well as on initial distribution of probe fields.

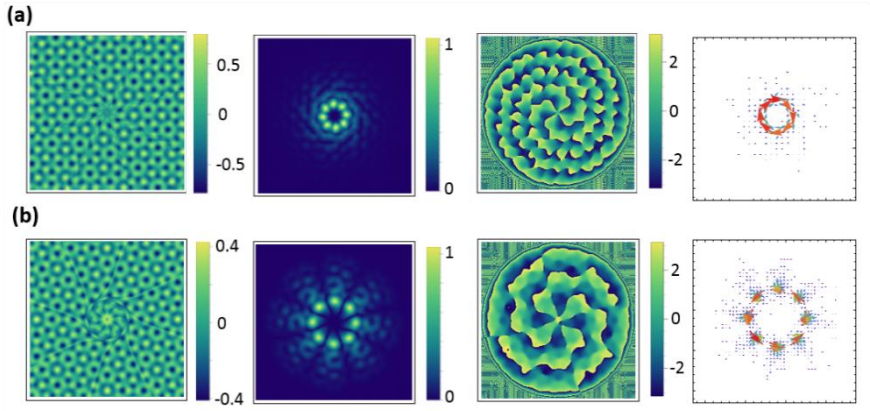

Figure 3.6. Probe field evolution in a chiral directionality field, for octagonal background potentials. (a) Vortex with sink (b) circular flow channel, corresponding to the vector fields of Fig. 3(c) and 3(d). The first column represents the imaginary part of the potential (real part is shown in Fig.3.3 (b); the second column is the normalized final amplitude distributions of the probe field; the third column is the phase distributions of the probe field and the fourth column represents the corresponding flow of the probe field.

3.6 Directionality fields in nonlinear systems

In previous sections, only linear systems were considered, however, directionality fields may also be considered for nonlinear laser-like systems, with field saturation. We consider such a system described by the Complex Ginzburg Landau equation, given as;

$$\partial_t A(r,t) = i\,\nabla_\perp^2 A(r,t) + (p - |A|^2)A(r,t) + iV(r)A(r,t) \qquad (3.21)$$

where $A(r,t)$ is the envelope of complex field distributed in space, r, and p is the pump parameter. The nonlinearity is due to the gain saturation. $V(r)$ is a non-Hermitian potential generated from the local Hilbert transform.

As a general example, we arbitrarily consider an octagonal background pattern [see Fig. 3.3(b)] and study sink and chiral directionality fields in the form of a vortex and a circular channel flow. The results obtained for a nonlinear laser-like system are summarized in Fig. 3.7. Moreover, we calculate the flux during the evolution of the field. Results at particular time instants, t, are presented with spatial field distribution as depicted in bottom row of Fig. 3.7. It is clear from the flux that the field is directed towards the center, during evolution, confirming the sink, vortex and circular channel flow of light.

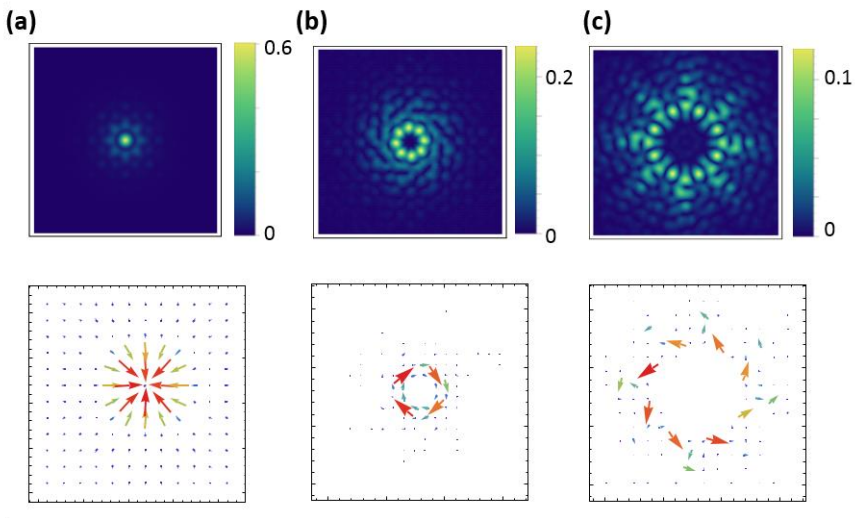

Figure 3.7. Field evolution by the CGLE (laser case) for a directionality field in the form of (a) a sink (b) a vortex (c) a circular channel flow. The top row represents the stationary field profile after saturation and bottom row displays the corresponding field flow confirming the predictions.

3.7 Propagation within Directionality fields

In the previous sections, we explore the temporal evolution, or equivalently longitudinal propagation, of a probe field in the proposed directionality fields. All previous results are supported by paraxial approximations, however, we here explore the performance of the local Hilbert transform beyond the paraxial limit, for the case of in-plane propagation of probe filed within the 2D plane. Thus, the aim of this section is twofold, to analyze propagation when the potential is not transverse but in-plane, and to numerically assess the proposed generalized local Hilbert transform in the non-paraxial limit, using the full set of Maxwell's equations for the spatial propagation of the probe field. Therefore, we provide confirmation of the directionality fields, at optical frequencies, on the full set of Maxwell equations employing the finite-difference-time-domain (FDTD) method.

3.7.1 Sink Directionality fields with gain-loss media

In section 3.5.1, we provide a detailed analysis of the temporal evolution (longitudinal propagation) of the sink directionality field generated from different background patterns. Here, we extend the same procedure and perform FDTD simulations for in-plane filed propagation, in an optical medium with an octagonally-patterned background potential for sink directionality fields. Fig. 3.8(a) shows the spatial refractive distribution of the initial background profile, while the imaginary profile of the modified medium, generated by sink vectorial field, is depicted in Fig. 3.8(b). We place a source within the 2D modified medium which injects electromagnetic waves with an electric field polarized perpendicularly to the plane. Figure 3.8 collectively shows the full-wave FDTD simulation results at various time frames, and for sources with different beam waists.

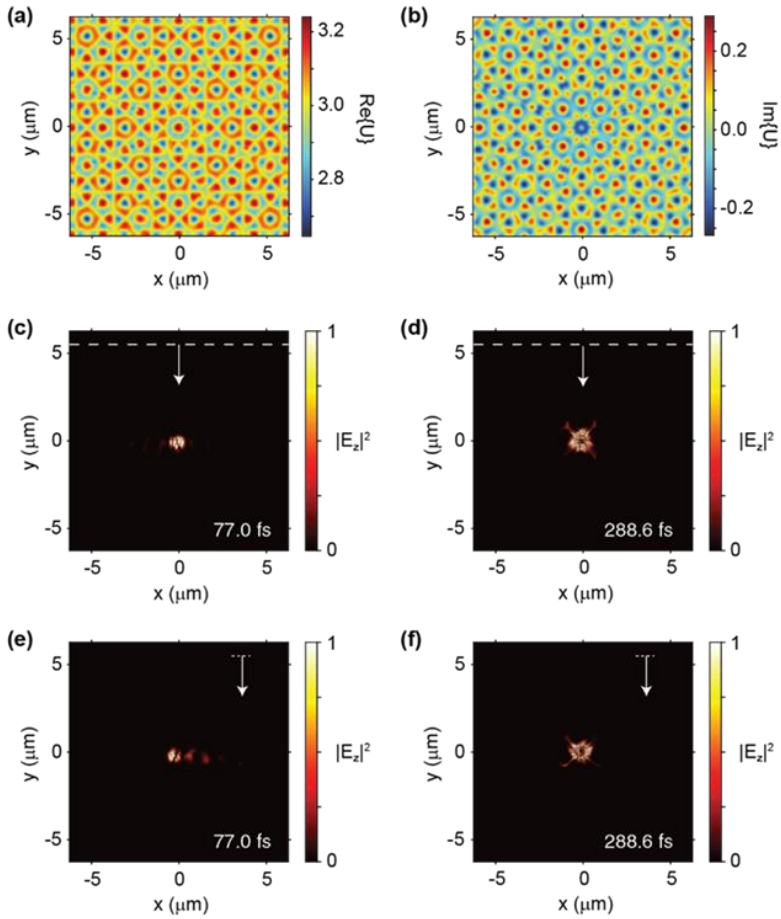

Figure 3.8. Real (a) and imaginary (b) parts of the refractive index generated by the local Hilbert transforms in form of a sink. Instantaneous spatial intensity profiles for a line source illumination with a beam waist radius of 5.0 μm, at the time frames: (c) 77.0 fs and (d) 288.6 fs. Similar intensity profiles for a narrow-line source illumination, with a beam waist radius of 1.0 μm, at the time frames: (e) 77.0 fs and (f) 288.6 fs. Both sources inject a broadband pulse with a central frequency of 599.6 THz (i.e. the central wavelength of 500 nm) with a bandwidth of 133.6 THz. The dashed white lines indicate the positions of the sources, while the white arrows denote the source injection direction.

We note that for the case represented in Fig. 3.8, the localization effect is observed twice. First, the incident pulse in the form of a plane wave propagating towards the sink focuses at the center of the sink [see Figs. 3.8(c) and 3.8(e)]. This is a transient behavior, and it evidences that the directionality field concentrates the incoming wave into the sink. The field behavior after this primary focusing strongly depends on the specific situation. In this particular case, the fields temporally dissipate from the sink position, however, in a long-term scale, they again concentrate at the sink position, as clearly shown in Figs. 3.8(d) and 3.8(f). Therefore, we show the twofold effect of field-management by the directionality field: transient and asymptotic. The asymptotic concentration of the probe field precisely corresponds to the (stationary) scattering theory.

3.7.2 Sink Directionality fields with lossy media

An important advantage of the field directionality concept is that the complex locally transformed media can be constructed excluding gain materials and consider lossy materials only. To achieve this goal, we simply add an "offset" to the imaginary part of the dielectric permittivity such that the gain areas are completely eliminated in the sample optical medium. Note that since the Fourier spectra of a constant offset function is a Dirac delta function positioned at the center of the wavevector domain, adding the offset does not distort the local spectra of the medium. We apply this method to the potential of Fig.3.8 and the corresponding numerical calculations are given in Figs. 3.9(a) and 3.9(b) for sources with different waist radii. It follows from these figures, that the incoming wave is, as expected, directed towards the center, forming a localization around the center region. It is noted that no post-localization occurs in this case, due to the absence of any gain material.

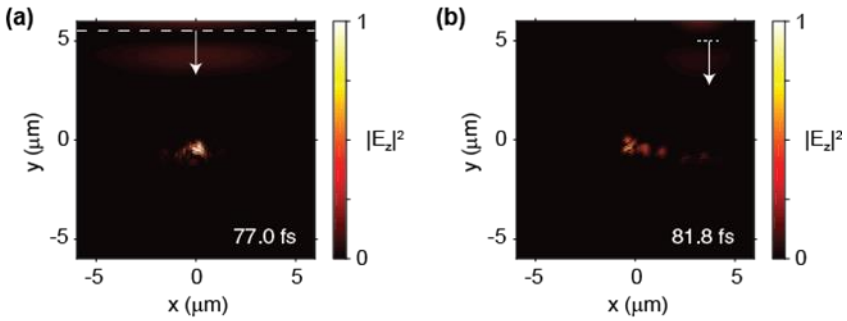

Figure 3.9. Instantaneous spatial intensity profiles in a pure lossy medium: (a) for a line source illumination with a Gaussian beam waist radius of 5.0 μm and (b) for a narrow-line source illumination with a Gaussian beam waist radius of 1.0 μm at the time frames 77.0 fs and 81.8 fs, respectively. Temporal properties of the sources are the same as in Fig. 3.8. The dashed white lines indicate the positions of the sources, while the white arrows denote the source injection direction. Numerical calculations were performed using Lumerical FDTD Solutions.

The numerical simulation results indicate that the overall scenario remains same in both paraxial and FDTD model. The proposed theory of directionality fields, constructed using local Hilbert transform, can be applied for paraxial models like Schrödinger equation, and also to more complicated wave propagation models, in particular to full Maxwell equations using FDTD model.

3.8 Conclusions

We provide a new tool for the optical control of the field flow based on a local Hilbert transform, which may trigger and encourage a broad interest in the emerging community of non-Hermitian potentials. To date, the reported non-Hermitian systems allow homogeneous unidirectionality for only one single vectorial direction in the whole space with different non-

trivial effects. In contrast, in this chapter, we propose the novel concept of local unidirectionality, which we refer as directionality fields, for the control of the flow of light. To obtain such non-Hermitian potentials with the desired unidirectionality, we derive a new mathematical framework: a local Hilbert transforms. The local Hilbert transform, developed in 1D and 2D, relates the two quadratures, real and imaginary parts of the spatial distribution of non-Hermitian potentials to generate arbitrary directionality fields from any arbitrary background pattern. Besides, the relations obtained in 2D could be straightforwardly extendable to 3D systems. We perform a detailed analysis of sink directionality fields generated from initial periodic, quasi-periodic, random and localized background potentials. We numerically show that the temporal evolution (or transverse propagation) of probe fields follows the sink directionality field, irrespective of the initial background profile or initial probe beam location. We also study the chiral directionality fields, e.g. a vortex and a circular flow channel with octagonal background pattern and results show a good agreement with the predictions. Therefore, we clearly demonstrate the flexibility and robustness of the proposal. To confirm our theory applicability beyond the paraxial approximation, we perform FDTD simulations of field propagation within the potential plane, using the full set of Maxwell equations. Directionality fields can be held both in the paraxial and non-paraxial limit. We also show that directionality fields can be observed with purely lossy media, thus increasing the feasibility for practical realization, e.g. Perfectly Matched Layer (PML) on arbitrary boundary contours. Moreover, we demonstrate that directionality fields can be generated in nonlinear laser-like systems described by Complex Ginzburg-Landau equation. Such directionality field concept applied to the electromagnetic spectrum can lead to a plethora of optical applications ranging from efficient light detectors/absorbers, lasers with improved

brightness and beam emission quality to optical data processors. The proposed theory can yield a significant control over electromagnetic field flows, providing an alternative to the broad field of transformation optics. Our proposal is generic, which may offer rich possibilities for structuring the light in linear and nonlinear micro-optical systems. Moreover, it can be applied to all fields of wave dynamics, like zero temperature Bose-Einstein condensates, acoustics, plasmonic waves, etc., which are described by the models of Schrödinger equation type.

Chapter 4
Realizations of Non-Hermitian Systems

In the previous chapters, we developed new light-manipulation concepts in non-Hermitian media enabling high spatial quality beams. Based on these ideas, we show here how non-Hermitian media can be physically realized in technological systems. This chapter is devoted to the real world applications of non-Hermitian systems. It is organized in two parts. In the first part, the capability of non-Hermitian media to develop the self-collimation phenomenon is tested in two-dimensional (2D) PT-symmetric lattices which can have direct applications to beam profile shaping in integrated optics. In the second part, three different schemes of the index and gain-loss modulations are proposed to obtain high spatial quality beams in three different semiconductor devices: (i) Stabilization of broad area semiconductor amplifiers is demonstrated using the 2D index and gain-loss modulations. (ii) A novel design of flat mirror VECSEL is proposed in which stability of the device is enhanced using the periodic spatiotemporal modulation of the pump profile. (iii) A new class of PT-axisymmetric lasers was proposed for stable and high spatial quality emission. The idea is based on the local PT-symmetry explained in Chapter 2.

4.1 Introduction to Self-collimated beams

Diffraction is a well-known fundamental phenomenon in which different spatial frequency components acquire different phase shifts during propagation, leading to light beam broadening. This can be described with the propagation of an optical beam, for instance, a Gaussian beam, in the free space, as shown in Fig. 4.1(a). The beam wavefronts become curved during propagation due to a relative phase shift among angular components depending on the propagation angles. The corresponding angular spectrum is shown in Fig. 4.1(b), where the concave surface illustrates the normal (positive) diffraction observed in a homogeneous medium. However, modulated media can present more complex spatial dispersion relations like convex surfaces leading to negative diffraction or flat surfaces around $k_x = 0$, denoting no diffraction and the corresponding self-collimation effect.

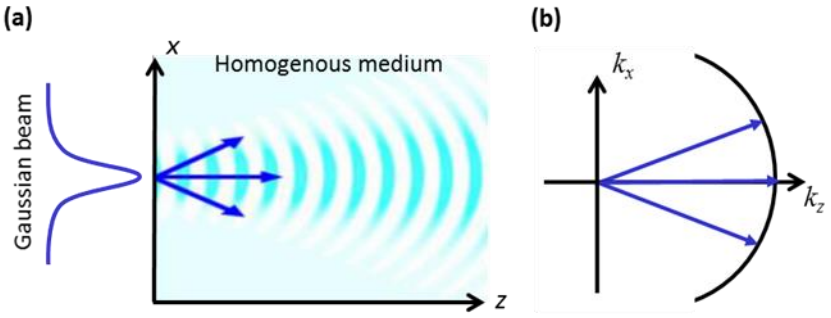

Figure 4.1. (a) A Gaussian beam, propagating in the *z*-direction, is decomposed into different plane waves (b) corresponding angular spatial spectrum showing concave wavefront surface for normal diffraction.

In practical systems, diffraction of light beams leads to undesirable effects such as beam divergence (diffraction broadening) which degrades the performance and limits the applications. Therefore, the generation of non-

diffractive beams is desired for increasing the efficiency of many optical devices, especially for integrated photonic optics. In recent years, several approaches are proposed to limit the diffraction spreading and enhance the beam directivity. One of the most common methods is to generate the non-diffractive beams through canonical superposition of plane waves. Bessel [Dur87], Mathieu [Veg00], and Weber [Ban04] beams are most common examples of such non-diffractive beams [see Fig. 4.2].

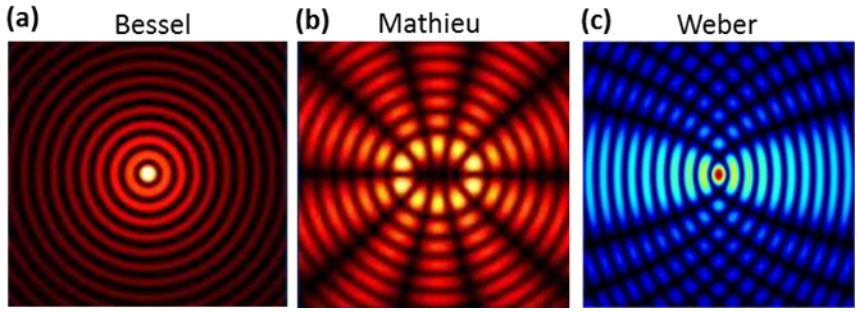

Figure 4.2. Examples of non-diffractive beams profiles (a) Bessel beam (b) Mathieu beam (c) Weber beam.

All these non-diffractive beams have infinite spatial size and supposed to convey infinite power and energy. For practical applications, such beams are truncated (their size and energy are actually limited) that leads to diffraction. Therefore, we can postpone the diffraction to some distance using such non-diffractive beams but can´t completely get rid of it. In this situation, the control of propagating beam diffraction may require some alternative physical mechanisms. Another most common approach relies on structured materials that provide an efficient way to control and engineer the dispersion properties of propagating beams. One of the possible effects is the reduction or even elimination of diffraction, leading to the self-collimation phenomenon. The self-collimation effect is observed when the

surface of constant frequency becomes flat for a specific range of light frequencies, and propagation angles. As a result, the beam maintains its width for long distances as compared to free space diffraction length. The phenomenon of beam self-collimation is also known as dynamical localization in quantum mechanics, which can be observed in modulated lattices [Lon06, Sta06b, Lig07, Gar12]. More recently, self-collimation has been realized in acoustics [Esp07, Per07], exciton-polariton condensates [Den10], however, this effect is more extensively explored in optics. The diffraction-free propagation, or the so-called self-collimation, was first discovered in the Photonic crystal (PhC), where a spatial modulation of the refractive index on the wavelength scale tailors diffraction properties [Zen87, Kos99, Wit02, Chi03, Pra07a, Sta06a]. Later, gain-loss modulated (GLM) materials, where gain and loss are periodically modulated on the wavelength scale, also showed similar spatial effects resulting in flat lensing, focusing and self-collimation [Sta09, Bot10]. In such materials, the angular dependence of the phase velocity and intensity growth leads to different spatial effects through diffractive and diffusive management. In reality, the frequency dependence of gain-loss and refractive index are expected to occur together in real materials due to the non-instantaneous and causal response of the medium, as discussed in the previous chapter in the context of Kramers-Kronig relations. Therefore, the simultaneous management of diffraction and diffusion should be considered in real materials to increase the feasibility of practical realizations. This perspective requires complex materials to control the dispersive properties of propagating beams. More recently, self-collimation has also been demonstrated in periodic complex materials [Her14] and metamaterials [Agu08, Pol11]; besides, flat bands were engineered in thresholdless high-dimensional complex crystals [Cer16] with PT-symmetry.

In this section, we propose new configurations of 2D non-Hermitian lattices to observe the non-diffractive propagation of beams. This effect seems to be possible in such complex media due to its ability to tailor the dispersion properties through spatial modulation. We mainly focus on the PT-symmetric case which allows self-collimated beam with asymmetric energy flows among the propagating modes. In particular, the PT-symmetry is considered in transverse, longitudinal and simultaneously in both directions. We perform the analytical study to predict the self-collimation phenomenon in such lattices using coupled mode harmonic expansion and further, the results are confirmed with numerical simulations performed in paraxial approximation.

4.1.1 Proposed lattice configuration PT*x*, PT*z*, PT*zx*

In the previous chapters, we discuss that non-Hermitian potentials allow symmetric or asymmetric coupling among the propagating modes under particular symmetry conditions. Based on different coupling mechanism, we propose here 2D periodic PT-symmetric lattices to observe the self-collimation phenomenon. We consider three different lattice configurations holding PT-symmetry in the transverse (PT*x*), longitudinal (PT*z*) and simultaneously in both (PT*zx*) directions. Such 2D spatially periodic lattices can be defined with complex refractive index profiles as:

$$\Delta n_{\mathrm{PT}x} = [n_{Re}\cos(q_{\perp}x) + in_{Im}\sin(q_{\perp}x)]\cos(q_{\parallel}z) \tag{4.1}$$

$$\Delta n_{\mathrm{PT}z} = \left[n_{Re}\cos(q_{\parallel}z) + in_{Im}\sin(q_{\parallel}z)\right]\cos(q_{\perp}x) \tag{4.2}$$

$$\Delta n_{\mathrm{PT}zx} = n_{Re}\cos(q_{\perp}x + q_{\parallel}z) + in_{Im}\sin(q_{\perp}x + q_{\parallel}z) \tag{4.3}$$

where $q_{\perp}$ and $q_{||}$ are the reciprocal lattice vector of modulation in the transverse and longitudinal direction, respectively. The refractive index and gain-loss modulation amplitudes are represented with n_{Re} and n_{Im}. To show different coupling behavior, we provide the index and gain/loss profiles of PT*x*, PT*z* and PT*zx* potential with the corresponding coupling wavevectors in Fig. 4.3. The coupling behavior depends on the index and gain-loss modulation amplitudes that can favor the propagation in particular direction with appropriate parameters. In case of PT*x* lattice, the coupling of transverse modes in light propagation along the *z*-direction becomes asymmetric [see Fig. 4.3(a)], while PT*z* lattices give a symmetric coupling among modes [see Fig. 4.3(b)]. In PT*zx* lattices, the potential is generated by only one wavevector ensuring the asymmetric coupling. The possible couplings between wave vectors for this potential are shown in Fig.4.3(c).

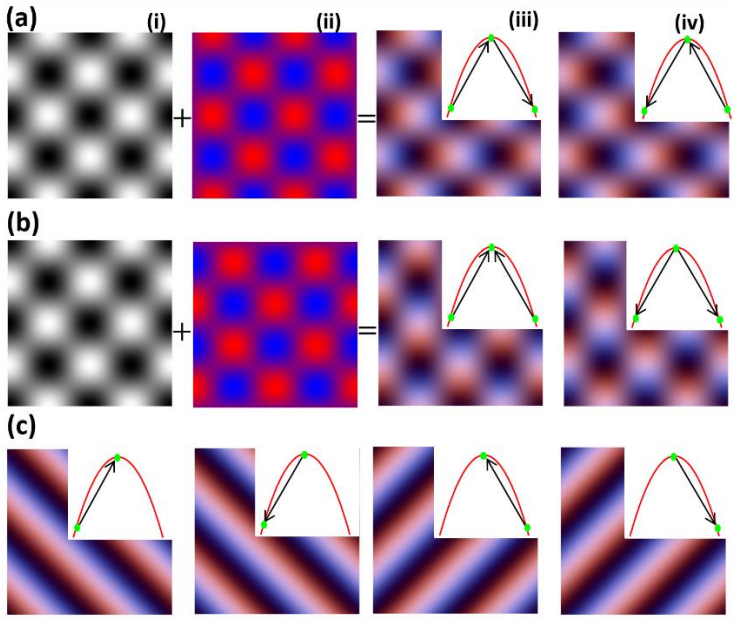

Figure 4.3. PT-symmetric lattices holding PT-symmetry in different direction (a) PT*x* (b) PT*z* (c) PT*zx* . In (a,b), refractive index and gain-loss profiles are shown

in (i,ii) while (iii,iv) represents a combination of index and gain/loss profiles of the complex potential with modulations in the transverse and longitudinal direction and its complex conjugate. In (c), complex modulation profiles of PT*zx* crystal, and its complex conjugate are shown in (i,ii) while (ii,iv) represent the complex modulation profiles of π rotated PT*zx* crystal, and its complex conjugate. Insets display the corresponding reciprocal lattice vectors for the three PT-symmetric complex crystals showing different couplings for a given complex lattice and its complex conjugate.

4.1.2 Mathematical model

In order to study the proposed 2D PT-symmetric lattices, we consider the normalized paraxial model for an electromagnetic field propagating in the *z*-direction, expressed as:

$$\partial_z A(x,z) = i\,\nabla_\perp^2 A(x,z) + iV(x,Qz)A(x,z) \qquad (4.4)$$

where $V(x,Qz)$ given by the possible complex refractive index profiles in Eqs.4.1, 4.2 and 4.3 is the normalized potential and depends on the dimensionless geometrical parameter, $Q = 2k_0 q_{\|}/q_\perp^{-2}$. For convenience, we normalize the transverse coordinate, x, to $q_\perp^{-1}$ and the longitudinal coordinate, z, to $2k_0/q_\perp^{-2}$ –being the wavevector's components k_x, k_z correspondingly scaled to $q_\perp$ and $q_\perp^{-2}/2k_0$. The real/imaginary amplitudes of the potential are normalized as: $m_{Re/Im} = n_{Re/Im}\,2k_0^2/n_0 q_\perp^2$ where k_0 is the wave number of incident monochromatic light and n_0 is the initial background refractive index.

4.1.3 Analytical study: Coupled mode expansion

With the aim to study the spatial dynamics in beam propagation, we first consider a harmonic expansion of the transverse field and analyze the

coupling between the different transverse harmonics. This coupling is given by the lattices modulation generated by the corresponding lattice wave vectors that can be written as $\vec{q}_1 = (1, Q), \vec{q}_2 = (-1, Q)$ for the normalized variables. The potentials of the three considered PT-symmetric potentials can be expressed as a combination of the lattice wave vectors in the forms:

$$V_{PT} = m_1 e^{\,i\vec{q}_1\vec{r}} + m_2 e^{i\vec{q}_2\vec{r}} + m_3 e^{-i\vec{q}_1\vec{r}} + m_4 e^{-i\vec{q}_2\vec{r}} \qquad (4.5)$$

and the field $A(x, z)$ is expanded into the resultant harmonics, $\vec{q}_{l,p} = \vec{k} + l\vec{q}_1 + p\vec{q}_2$ with amplitudes $a_{l,p}$ equivalently to a Bloch mode expansion. In general, it can be written:

$$A(x, z) = e^{-i(k_x x)} \sum_{l,p} a_{l,p}\ e^{-i[-(l-p)x + (l+p)Qz]} \qquad (4.6)$$

As suggested in previous studies of PhCs and GLMs, for the analysis of beam propagation inside these complex lattices, it is sufficient to consider the three most relevant harmonics $(l, p) = (0,0); (0,1); (1,0)$ with amplitudes $(a_{0,0}, a_{0,1}, a_{1,0})$ [Sta06a, Sta09]. Inserting this Bloch mode expansion in the propagation equation, Eq. (4.2), we obtain a system of coupled equations given by:

$$\frac{da_{1,0}}{dz} = -ik_x^2 a_{0,0} + im_1 a_{0,1} + m_2 a_{1,0} \qquad (4.7a)$$

$$\frac{da_{0,0}}{dz} = -i(k_x - 1)^2 a_{0,1} + iQa_{0,1} + m_3 a_{0,0} \qquad (4.7b)$$

$$\frac{da_{0,1}}{dz} = -i(k_x + 1)^2 a_{1,0} + im_1 a_{1,0} + m_4 a_{0,0} \qquad (4.7c)$$

where m_1, m_2, m_3 and m_4 are the linear coefficients which define the coupling behavior between different modes. These coefficients depend on real and imaginary parts of the modulation amplitudes of particular PT-symmetric lattice under investigation. In our analysis, asymmetric coupling between modes in PTx case gives $m_1 = m_4 = (m_{Re} + m_{Im})/4$ and $m_2 = m_3 = (m_{Re} - m_{Im})/4$ while for PTz, the symmetric coupling provides $m_1 = m_2 = (m_{Re} + m_{Im})/4$,and $m_3 = m_4 = (m_{Re} - m_{Im})/4$. In PT$zx$, the harmonic $a_{0,1}$ is decoupled and the coefficients become: $m_2 = m_4 = 0$, $m_1 = (m_{Re} + m_{Im})/2$ and $m_3 = (m_{Re} - m_{Im})/2$. The eigenvalues of the coupled system can be calculated from the Jacobian matrix of equation set (4.7) and present real or imaginary values depending on the matrix coefficients. For all positive coefficients, when $m_{Re} > m_{Im}$ the PT-symmetric media show real eigenvalues like in PhC-media, while complex conjugated eigenvalues arise for $m_{Re} < m_{Im}$ like in GLM-media. However, the corresponding eigenvectors are not necessary symmetric as in the PhC or GLM materials. Due to complex nature of PT-symmetric lattices, the coupling between the harmonic components can be both reactive and dissipative. For PhCs-like case, all eigenvalues are real-valued and coupling is reactive leading to standard band-gaps in the spatial dispersion. On the other hand, for the GLM-like case, eigenvalues are complex conjugated. Thus, their real parts lock while a nonzero imaginary part develops. The curvature of the real and imaginary spatial dispersion $k_z(k_x)$ respectively determines the diffraction and diffusion of light in propagation along the material and the material modulation allow managing them to obtain flat segments in real and imaginary part of spatial dispersion denoting non-diffraction and non-diffusive phenomena, respectively. The flat features in dispersion relation can be easily determined by imposing a zero value on the second derivative either of the real or the imaginary part of spatial dispersion. In this way, we can explore the parameter space to

identify the non-diffractive and non-diffusive conditions in the proposed lattices using the eigenvalues analysis. We have three-dimensional parameter space (m_{Re}, m_{Im}, Q) which requires a lot of time to explore completely. To simplify our analysis, we reduce the parameter space to two-dimension (m_{Re}, Q) by assuming the condition $m_{Im} = c - m_{Re}$ where c being a constant number. We study the dynamics the PT-symmetric lattices by conveniently exploring normalized pair of parameters (m_{Re}, Q).

We start with a non-Hermitian lattice satisfying the PT-symmetry only in the transverse or the longitudinal direction while considering the real modulation in other direction (PT*x* or PT*z*). The eigenvalue analysis provides the same results for both PT*x* and PT*z* cases while the difference lies in eigenvectors only. Note that eigenvectors give the harmonic amplitudes composing the eigenmode while eigenvalues give the evolution of this mode in propagation. Due to different coupling mechanism in both cases, the eigenvectors are asymmetric for PT*x* case and symmetric for PTz case. The conditions for non-diffractive and non-diffusive beam propagation in the parameter space (m_{Re}, Q) are analytically calculated and results are provided in Fig. 4.4(a). Note the lack of crossing points of the nondiffractive and nondiffusive curves meaning the nonpossible beam self-collimation in GLM-like media. Therefore, we observe the self-collimation only appear in the PhC-like regime for the PT*x* or PTz lattices, where the system has no intrinsic diffusion. The corresponding real-valued dispersion, exhibiting a flat non-diffractive mode is shown in Fig. 4.4 for the representative point II (red curve). Further, we analyze PTz*x* lattice and similarly determine the non-diffractive regime in parameter space (m_{Re}, Q), as shown in Fig. 4.4 (b). Note that in this case, the red curve corresponding to point III is a non-diffractive mode ($\partial^2 k_z / \partial k_z^2 \neq 0$), however, with non-zero refraction $\partial k_z / \partial k_z \neq 0$.

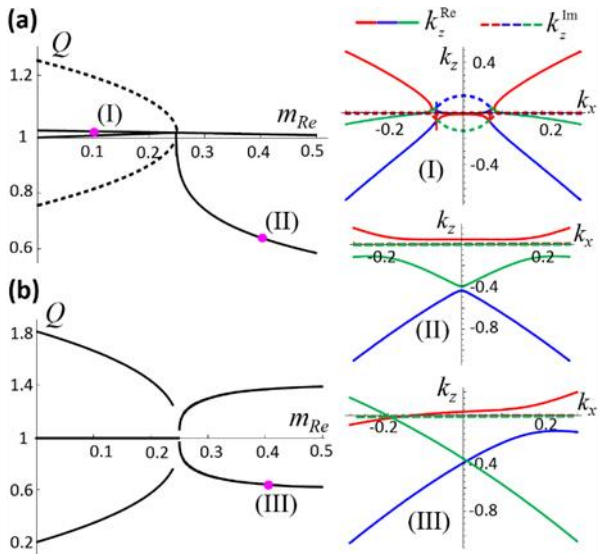

Figure 4.4. Complex dispersion relations for the three-mode expansion. (Left) non-diffraction conditions (solid curves) and non-diffusive propagation (dashed curves) in the parameter space (m_{Re}, Q), being $m_{Im} = c - m_{Re}$ for the different lattices where c =0.5. (a) PTx or PTz b) PTzx. (Right) Spatial dispersion relations for three representative points with non-diffractive propagation corresponding to different parameter sets: (I) (0.1, 0.99) (II) (0.4, 0.64) (III) (0.4, 0.6). The solid/dashed curves represent the real/imaginary parts of the wavenumber.

4.1.4 Numerical analysis: Self-collimated regimes

In this section, we provide the numerical evidence of our analytical predictions for self-collimation phenomenon in different PT-symmetric lattices. For this purpose, we assume an initial Gaussian beam which exhibits typical diffraction phenomenon in free space. We propagate the beam through proposed PT-symmetric lattices for certain modulation parameters and observe the evolution of the field intensity. To compare the results with analytical predictions, we calculate the beam width after a sufficient long propagation length using a knife-edge method [Sie91] by

filtering out the higher spatial frequencies in the final distribution. The propagation of the beam along the structure, for three representative points (I, II, III) of Fig. 4.4, is shown in Fig. 4.5.

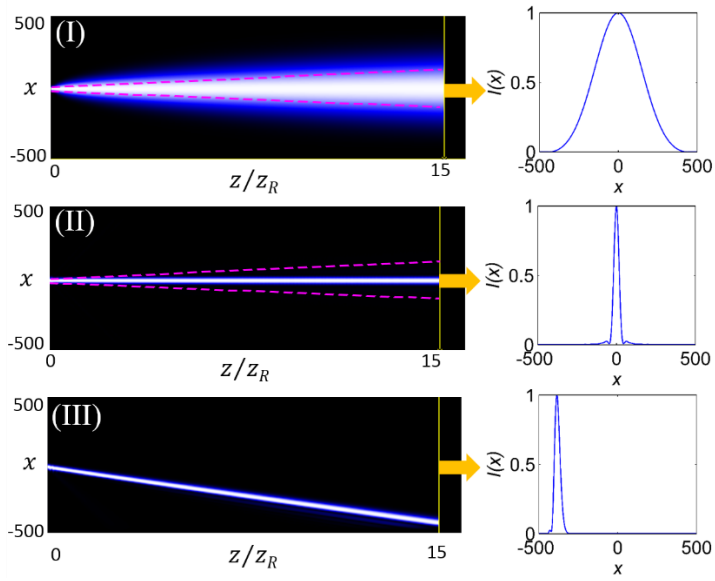

Figure 4.5. Propagation of a Gaussian beam through PT-symmetric media for a normalized propagated length of $z = 15z_R$, being z_R the Rayleigh length. (Left) evolution of field intensity for the three particular parameter sets of Fig. 4.4, exhibiting: (I) non-diffractive but diffusive propagation for a PT*x* GLM-like case, (II) non-diffractive propagation for a PT*x* PhC-like case and (III) non-diffractive propagation for a PT*zx* PhC-like case. (Right) corresponding field intensity transversal profiles at the propagation length, $z = 15z_R$. The peak amplitude in each transverse section is normalized to unity. The initial Gaussian beam width is $w_0 = 20$ and $z_R = 100$. The dotted line in (I,II) represents the free space diffracted beam, shown for comparison.

The beam shows non-diffractive propagation but experience diffusive broadening for parameter set (I) corresponding to GLM-like case in PT*x* or

PTz lattice. On the other hand, non-diffractive beam propagation is observed with parameter sets (II) and (III) that correspond to PhC-like cases when there is no intrinsic diffusion. The numerical results are in perfect agreement with our analytical predictions. We filter out the higher order transverse modes (k_x> 0.5) in the intensity profile during propagation for a clearer representation. The intensity profiles at the end of the lattice ($z = 15z_R$) are shown in the right column of Fig. 4.5.

For a comprehensive numerical study of the self-collimated beams, we explore the parameter space, (m_{Re}, Q), by calculating beam width after a sufficient long propagation ($z = 5z_R$) of a Gaussian beam through different PT-symmetric lattices. The values of beam width are normalized to the initial width w/w_0 to guess the broadening of the beam. We plot the normalized widths by indexing it with different colors in the map [see Fig. 4.1.5] to identify the self-collimation regime, that is, where normalized beam widths are equal to the initial width. We note that the PTx and PTz lattices give exactly the same normalized beam width values in the parameter space as the PTx case, as predicted in eigenvalue analysis. However, the field distributions in the presence of transverse modulation look different, due to different dynamics and transverse mode coupling. The white areas in Fig. 4.6 correspond to the self-collimation regime, for which the initial beam maintains its width along propagation length. In case of PTzx potential, we obtain two distinct self-collimation regions for $Q < 1$ and $Q > 1$ both lying in the PhC-like case, i.e. $m_{Re} \geq c/2$ [see Fig. 4.6(b)]. These two regions correspond to non-diffractive propagation of different modes. The bottom region ($Q < 1$) corresponds to the non-diffraction propagation of central mode carrying most of the system energy. On the other hand, top region ($Q < 1$) represents the non-diffraction propagation of other modes carrying a very small amount of system energy. Therefore,

the most interesting is the bottom region for practical realizations. In GLM-like case, the diffusion is always present in PT lattices that leads to broadening of the beam irrespective of non-diffractive condition. In order to compare the numerical and analytical results, we superimpose the analytical predicted curves of non-diffractive and non-diffusive propagation onto the numerically calculated maps. The numerical results show a perfect agreement with the analytical predictions, confirming the self-collimation regimes in parameter space.

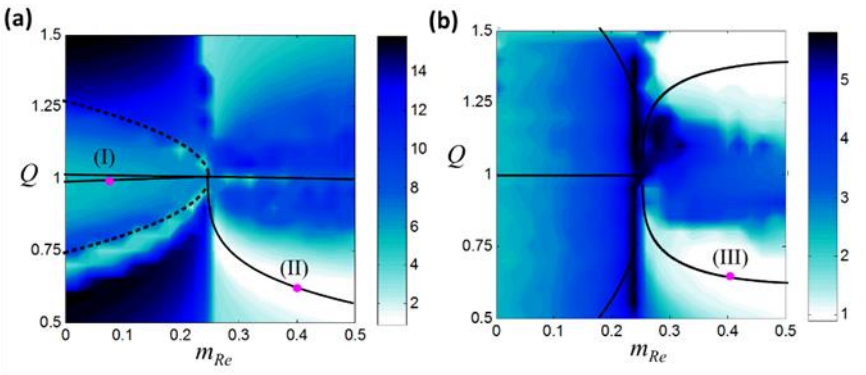

Figure 4.6. Beam width maps in parameter space, (m_{Re}, Q). Numerical beam width (w/w_o) after a long propagation ($z = 5z_R$) of a Gaussian beam for different PT-symmetric potentials: (a) PT*x* (b) PT*z*x. The white islands represent the self-collimation regimes. The solid and dotted curves show the analytical non-diffractive and non-diffusive conditions provided for comparison.

4.1.5 Mode dynamics of Self-collimated beams

In the previous sections, we explain that PT*x* and PT*z* lattices provide the same eigenvalues but show different mode dynamics due to different coupling mechanism among modes. In order to understand the mode dynamics of self-collimated beams in such lattices, first, we analytically determine the eigenvectors. In section 4.1.2, we consider three modes

$(0, \pm q)$ for eigenvalue analysis providing different eigenvectors for each eigenvalue. Here, we are only interested in eigenvectors of the non-diffractive mode which have three eigenvector components for a parameter set. For convenience, we normalize the eigenvector components to the fundamental harmonic as: $|a_+(k)| = \left|a_{1,0}(k)/a_{0,0}(k)\right|$, and $|a_-(k)| = \left|a_{0,1}(k)/a_{0,0}(k)\right|$. Such components are depicted for the PT*x* and corresponding complex conjugated PT*x* lattice in the first column of Fig. 4.7. It is obvious from the eigenvector components that energy flows are asymmetric in both PT*x* lattice, and that the modes carrying more energy are interchanged in complex conjugated potentials. Next, we numerically calculate the intensity profiles and spatial spectra $|A(k_x)|$ of a Gaussian beam propagated in such lattices. The asymmetric sides bands being $|A(k_x = -1) > A(k_x = 1)|$, as illustrated in Fig. 4.7a(iii) and reversed $|A(k_x = -1) < A(k_x = 1)|$ for the complex conjugated PT*x* lattice. Note that in the complex conjugated case, the energy flows in opposite directions due to the unidirectional coupling, as schematically represented in Figs. 4.3a(ii) and 4.3a(iv).

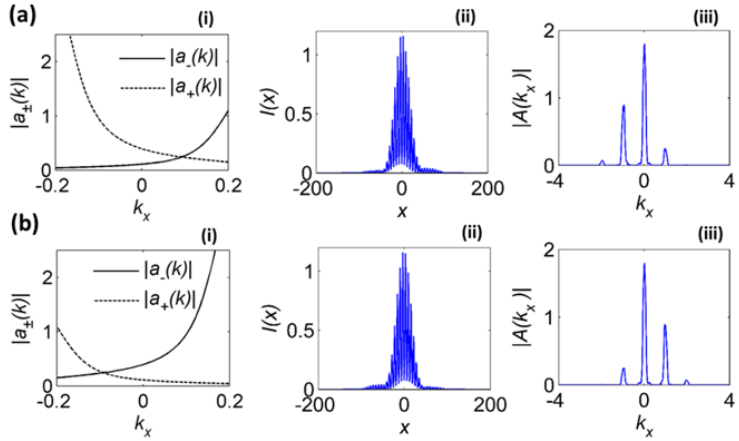

Figure 4.7. Dynamics analysis of a PT*x* potential (a) and its complex conjugate (b)

(i) normalized eigenvector components of non-diffracted branches of eigenvalues (ii)field intensity profiles of the propagated Gaussian beam (iii) corresponding spatial field spectra. Calculations correspond to parameter set (0.32, 0.71) after a propagation length of $z = 6z_R$.

In case of PTz lattice, we observe a symmetric mode coupling, $|a_+(k)| = |a_-(k)|$, with large eigenvector components in complex conjugated lattice [see Fig. 4.8a(i) and 4.8a(ii)]. In this case, the energy flow symmetrically to the side bands resulting in enhancement or reduction of spectral amplitudes, depending on the inward coupling or outward coupling as shown in Figs. 4.8a(iii) and 4.8b (iii), respectively. This spectral analysis confirms our predictions about different energy distribution between modes, asymmetrical for the PT*x* and symmetric for PT*z* lattices. We can say that the energy distribution between spatial modes of the self-collimated beams can be easily engineered in such lattices with appropriate modulation parameters.

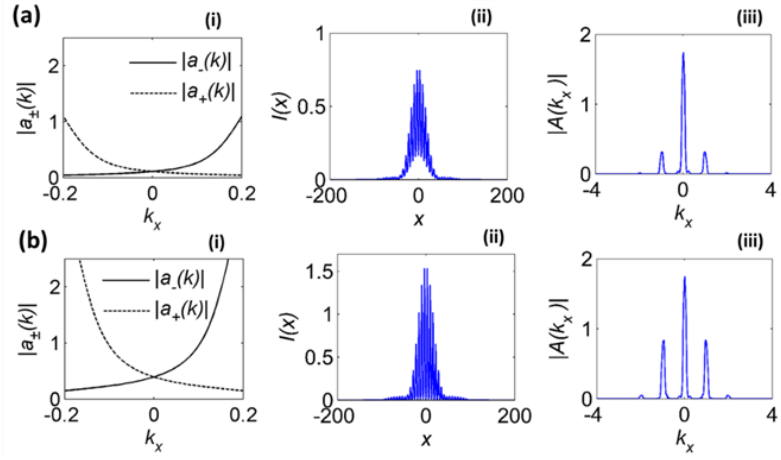

Figure 4.8. Dynamics analysis of a PTz potential (a) and its complex conjugate (b). (i) normalized eigenvector components of non-diffracted branches of eigenvalues (ii) field intensity profiles of the propagated Gaussian beam (iii)

corresponding spatial field spectra. Calculations correspond to the parameter set (0.32, 0.71) after a propagation length of $z = 6z_R$.

Furthermore, we analyze the dynamics of beam propagation in the self-collimation regime, for PTx and PTz lattices during evolution. We investigate numerically the energy flow between spatial modes (q = 0,±1) of the self-collimated beam along the non-diffractive line in Fig. 4.3(a). Modes energy is periodically oscillating after certain propagated length due to the resonant coupling mechanism given by transverse and longitudinal character of the lattice. We determine the mean values of spectral field components of the numerically propagated field and normalize the side-band amplitudes to the central mode amplitude as: $|A_{\pm}| = \langle|A(k_x = \pm 1)|\rangle / \langle|A(k_x = 0)|\rangle$ [see Fig. 4.8]. In PTx case, the modes coupling is asymmetric so $|A_+|$ and $|A_-|$ shows different amplitudes as depicted Fig. 4.8a(ii). Note that the complex conjugate of PTx lattice only reverses the spectral field amplitudes [see Fig. 4.9a(iii)]. On the other hand, in PTz case, the symmetric coupling leads to equal spectral amplitudes for spatial modes $|A_+| = |A_-|$. This also holds for the corresponding complex conjugated potential, for which the side-band energy is enhanced, as illustrated in Figs. 4.9b(ii) and 4.9b (iii).

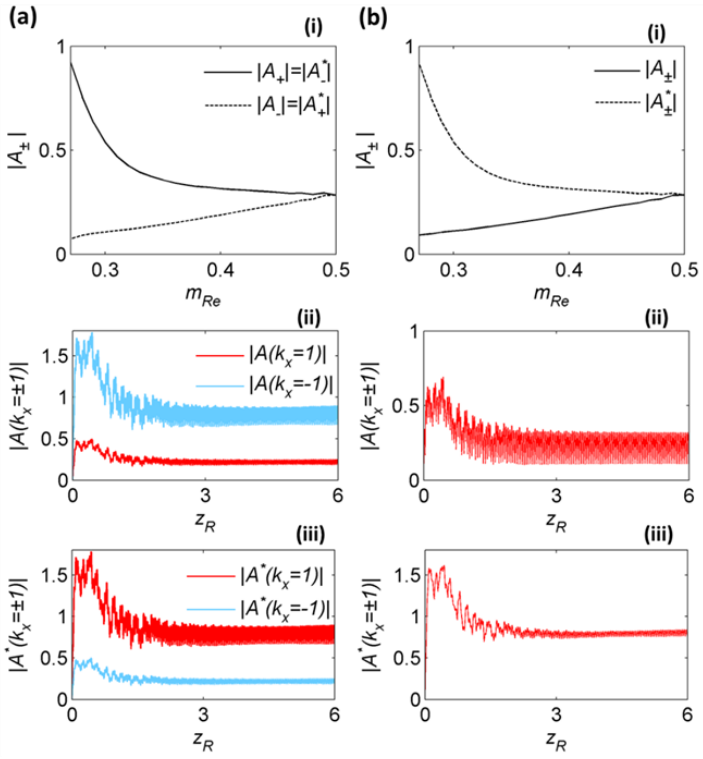

Figure 4.9. Numerical study of the dynamics of the spectral field components for a PT*x* (a) and PTz (b) potentials. (i) Normalized spectral field amplitudes $|A_{\pm}|$, along the non-diffractive curves of Fig. 4.4, for the PT lattices and their corresponding complex conjugated. Evolution of the spectral field components $|A(k_x = \pm 1)|$ in propagation for the considered complex potentials (ii) and their complex conjugates (iii), for the parameter set (0.32, 0.71).

4.1.6 Summary

We propose non-diffractive propagation of narrow beams in PT-symmetric lattices where gain-loss and refractive index modulations are phase-shifted by a quarter of the spatial period. We analyze 2D modulated systems, holding PT-symmetry either in the transverse (PT*x*), longitudinal (PTz) or simultaneously in both directions (PTz*x*). Such complex modulations may

influence the system dispersion leading to a complete suppression of diffraction and diffusion. We show that such complex lattices offer the possibility to suppress diffraction in the limiting cases of PhC-like and GLMM-like behaving lattices. However, non-diffractive beams in GLMM-like systems always experience self-broadening due to intrinsic diffusion. We explore the parameter space to determine the self-collimation regimes for PT*x*, PT*z*, and PT*zx* lattices. The analytical conditions for non-diffractive and non-diffusive beam propagation are in perfect agreement with numerical simulations performed under a paraxial approximation. Finally, we analyze the beam dynamics in the self-collimation regime. The symmetric and asymmetric coupling in self-collimated beams opens the way to control the energy distribution among spatial modes by 2D PT-symmetric crystals. The predicted self-collimation effect may be useful to shape the beam profile in PT-symmetric integrated optics.

4.2 Introduction to Semiconductor optical devices

Semiconductor optical devices particularly amplifiers and lasers are robust, compact and highly efficient light sources with many applications. The main component of such devices is a semiconductor gain medium, which allows stimulated emission. The majority of the semiconductor lasers are laser diodes in which stimulated emission is activated through electrical or optical pumping. There is a large variety of different semiconductor lasers available nowadays, covering broad parameter regions and many different application areas. They can be mainly divided by the emitting direction, e.g. edge emitting lasers and surface emitting lasers. In edge emitting lasers, also called Broad Area Laser (BAL) Diodes [see Fig. 4.10(a)], the light propagates parallel to the active or gain layer generated by the semiconductor p-n junction, while in Vertical-Cavity Surface-Emitting

Lasers (VCSEL) light propagates perpendicular to the surface of the semiconductor active layer.

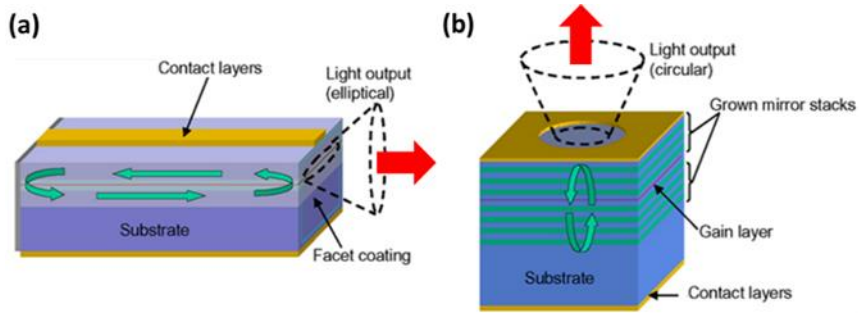

Figure 4.10. Schematic illustration of (a) Broad area edge emitting laser (BAL) (b) vertical-cavity surface-emitting laser (VCSEL).

Additionally, semiconductor amplifiers are also available from broad area laser diodes where the corresponding cavity mirrors are substituted by anti-reflection coatings and are called Broad Area Semiconductor (BAS) amplifiers. Surface emitting lasers can be further classified based on cavity length, and thus, resonators with few μm-long length cavity are named vertical-cavity-surface-emitting lasers (VCSELs) while external mirror resonators, with cavity lengths typically ranging from millimeters to centimeters, are called vertical-external-cavity surface-emitting lasers (VECSELs).

BALs and VCSELs suffer from a relatively low beam quality resulting in a less than optimal brightness and divergence. The large divergence makes its focalization and the coupling into fibers highly inefficient, impeding many industrial applications. The low spatial and temporal beam quality of these semiconductor lasers and amplifiers is due to the absence of an intrinsic selection mechanism of the emitted spatial mode within its large

aspect-ratio cavity. BALs and tapered amplifiers suffer the lack of mode selection in one spatial direction while VCSELs experience this drawback in both transverse directions. Moreover, nonlinear processes give rise to the modulation instability (MI) for strong enough nonlinear regimes which is responsible for beam inhomogeneities and filamentation that additionally deteriorates the quality of the beam [Hes95, Ada93, Mar96, Hes96]. The MI responds to the instability of the homogeneous solution by spatial modulations, leading to growing spatial modes and responsible for the patterns formation phenomenon in many spatially extended nonlinear dynamical systems. These instabilities can generate stable and unstable patterns in a route to spatiotemporal behaviors and chaotic pattern dynamics in a variety of systems, particularly in semiconductor devices. As a result, the performance of high-power semiconductor lasers is severely degraded and limit the number of possible applications. In this situation, efficient and compact schemes to control the detrimental spatiotemporal dynamics are needed to obtain stable output beam emission in such devices. A significant improvement in the beam quality would multiply the number of applications of these lasers.

Many theoretical and experimental attempts have been made to improve the spatial structure of the broad aperture semiconductor lasers using different techniques. Some of them are structured delayed optical feedback [Wol00], phase conjugated feedback [DeT97], external optical injection [Pak17], a Fourier-optical 4f setup [Wol99] and inward bent curvature in laser facet [Sal85]. Similarly, the problem of transverse mode selection in VECSELs is resolved using an external spherical mirror. All these techniques rely on complex external configurations which make the semiconductors devices less robust and compact.

In recent years, more feasible approaches based on dispersion management are reported to improve the output emission in such devices. Previous studies have shown that the periodic modulation of pump profile in transverse and longitudinal directions can lead to spatial filtering and stabilization effects in BAS amplifiers [Her12, Rad13]. However, stabilization through pump modulations result in a partial improvement of beams emitted by BAS amplifiers and is also limited to a small value of the linewidth enhancement factor, α_H, that relates index and gain variations [Kum14]. Thus, the pump modulation in such devices causes a combined gain and refraction index modulation limiting the beam stabilization for high enough α_H factors and pumping. In this situation, it is vital to explore more flexible and versatile schemes to enhance the stability of BAS amplifiers in highly nonlinear regimes.

In the next sections, we focus on three semiconductor devices, i.e. BAS amplifiers, VECSELs, and VCSELs, exploring new configurations to obtain narrow and high spatial beams in such devices. Firstly, we demonstrate that the in-phase 2D modulation of index and gain-loss in BAS amplifiers provides an efficient method of stabilization. Secondly, we propose a versatile design of flat mirror VECSELs in which the MI is suppressed using spatiotemporal modulation of the pump current. Thirdly, a novel configuration of PT-axisymmetric lasers is proposed in which light generated in the entire transverse area of the laser cavity is concentrated in a narrow beam by an axial modulation of refractive index and gain in a PT-symmetry.

4.3 Broad Area Semiconductor (BAS) Amplifiers

The spatially-incoherent light emission in high power regimes limits the application of BAS amplifiers as explained in section 4.2. Therefore, the

stabilization of BAS amplifiers is an important subject from the technological perspective. Here, we propose 2D periodic modulations of refractive index and pump (gain-loss) simultaneously on the transverse and longitudinal space, which provide an efficient scheme to control the emission of BAS amplifiers. The interplay between the index and gain-loss modulations efficiently suppresses the intrinsic pattern forming instabilities, leading to highly stable and bright narrow output beams in such devices. To explore the best-operating conditions, we analyze the stabilization performance of the device in terms of pump current and linewidth enhancement factor.

4.3.1 Mathematical model

The static paraxial model [Ult03], describing the dynamics of the electric field (A) and carrier density (N) for BAS amplifiers, can be expressed as:

$$\frac{\partial A}{\partial z} = \frac{i}{2k_0 n}\ \frac{\partial^2 A}{\partial x^2} + s[(1 - i\alpha_H)N - 1 - \gamma]A \qquad (4.8a)$$

$$D\frac{\partial^2 N}{\partial x^2} + p - N - (N-1)|A|^2 = 0 \qquad (4.8b)$$

where $A(x,z)$ is the slowly varying envelop of complex optical field propagating along longitudinal direction (z), γ considers the linear absorption and scattering loss, k_0 is the wavenumber of incoming light, p is the pump current, D is the carrier diffusion coefficient and α_H is the linewidth enhancement factor (Henry factor) of the semiconductor. Here s is inversely proportional to light matter interaction length. Typically s is of the order of $\sim 10^{-2}\mu m^{-1}$ and strongly depends on the construction of lasers

and semiconductor materials. Note that s can be related with the field confinement factor [Agr84].

For the small diffusion, $D \ll 0$, the carrier density is adiabatically eliminated and the model is reduced to one field equation given as:

$$\frac{\partial A}{\partial z} = \frac{i}{2k_0 n}\ \frac{\partial^2 A}{\partial x^2} + s\left[\frac{p-1}{1+|A|^2}(1 - i\alpha_H) - i\alpha_H - \gamma\right]A \qquad (4.9)$$

Equation (4.9) is used to analyze the dynamical behavior and stability of BAS amplifiers.

4.3.2 Linear stability analysis

Standard linear stability analysis is a most widely used technique to study the stability of the stationary solution of a non-linear system. In this method, first, we linearize the system in the presence of small external perturbations and then calculate the eigenvalue spectrum of this linearized system. The real part of eigenvalues $\lambda_{Re}(k)$ determine whether the stationary state is linearly stable, $\lambda_{Re}(k) < 0$ or unstable, $\lambda_{Re}(k) > 0$.

To perform the standard linear stability analysis of the unmodulated case, we determined the homogenous state: $A_0 = \sqrt{(p-1)/\gamma - 1}$ and then study the response of the system to a weak transverse perturbation around that steady state. We assumed the perturbations grow (or decay) exponentially with modulation in transverse wavenumber, k_x. After linearization, we obtain the following expression for Lyapunov exponents:

$$\lambda(k_x) = \frac{1}{2}\ \mathrm{Re}\left[-c_1 \pm i\sqrt{\frac{k_x^2}{nk_0}\left(\frac{k_x^2}{k_0} - 2c_1\alpha_H\right) - c_1^2}\right] \qquad (4.10)$$

where $c_1 = 2\gamma(p-\gamma-1)/(p-1)$. Equation (4.10) predicts the range of unstable transverse wave vectors responsible for the modulation instability. The bandwidth of unstable wavenumbers is $0 < k_x < \sqrt{2\alpha_H cnk_0}$ which is compatible with Ref. [Pra07b]. The maximum unstable wavenumber shifted towards the higher spatial frequencies with increasing α_{H} and p. Therefore, the region of instability mainly depends on the pump current, p, and the line width enhancement factor, α_H, as shown in Fig.4.11. As a matter of fact, instabilities are more pronounced in the highly nonlinear regime, leading to incoherent spatial emission.

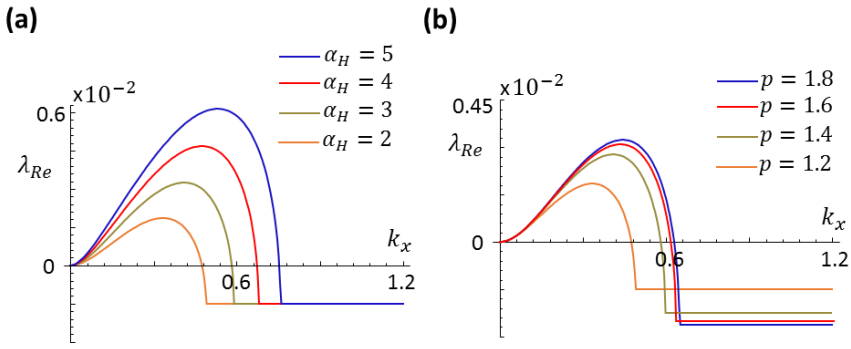

Figure 4.11. The results from the linear stability analysis showing the dependence of the Lyapunov growth exponents on (a) the linewidth enhancement factor, α_H and (b) the pump, p in different scenarios.

4.3.3 Index and pump modulated BAS amplifier

In the previous section, we discuss the destabilization of the steady state solution of BAS amplifiers through the modulation instability. The associated modes instability, depicted in Fig. 4.11, could be suppressed or eliminated by tailoring the system dispersion. One of most convenient approach for manipulating the dispersion is through spatial modulations. Previous studies show that the stability of BAS laser sources with only

pump modulations increase but not sufficiently for stabilizing highly nonlinear regimes arising at large enough α_H and pump values. The main reason is that pump modulations also infer refractive index modulations through the α_H factor enhancing the self-focusing effect and resultant instabilities. To deal this situation, we propose here to simultaneously modulate pump and refractive index profiles in the following way:

$$\frac{\partial A}{\partial z} = \frac{i}{2k_0 n}\frac{\partial^2 A}{\partial x^2} + \left[\frac{p + 4m_1(x,z) - 1}{1 + |A|^2}(1 - i\alpha_H) - i\alpha_H - \gamma\right]A + ik_0 4m_2(x,z)A \tag{4.11}$$

where $m_{1,2}(x,z) = m_{1,2}cos(q_x x)cos(q_z z)$, m_1 and m_2 are the amplitudes of the pump and the refractive index modulations of the same spatial profile, and q_x and q_z the corresponding modulation wavenumbers in the transverse and longitudinal directions. The spatial modulations are assumed in the transverse and longitudinal directions on small spatial scales, i.e. $|q_x| \gg |k_x|$ and $|q_z| \gg |\lambda|$, where k_z and λ are the typical transverse and exponential instability grow parameter, respectively. The modulation of the system may be characterized by a geometrical parameter relating both wavenumbers: $Q = 2nk_0 q_z/q_x^2$ where $q_x = 2\pi/d_\perp$, $q_z = 2\pi/d_\parallel$ being $d_\perp$ and $d_\parallel$ denote the transverse and longitudinal period of the modulation, respectively.

According to the Bloch-mode theorem, the steady-state solution of the modulated BAS system can be described by the transverse and longitudinal harmonics (n, l) of the modulations in the form: $A(r) = \sum a_{n,l}\, e^{i(nq_x x + lq_z z)}$. The interaction between the fundamental mode $a_{0,0}$ and higher order harmonics $a_{1,-1}$, $a_{-1,-1}$, … creates the resonance phenomenon for geometrical parameter $Q = 1$, which allows manipulation of the spatial

dispersion of the system [Sta06a]. Such mutual resonance between the transverse-longitudinal harmonics is expected to suppress the region of unstable wavevectors that excite the chaotic dynamics.

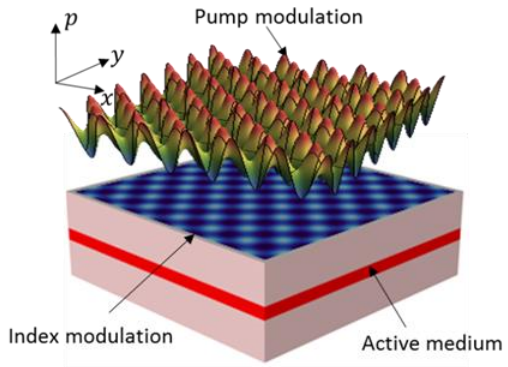

Figure 4.12. Schematic illustration of a BAS amplifier with the periodic modulations of the pump (gain-loss) and index profiles.

4.3.4 Stabilization results

To characterize the stability of doubly-modulated BAS amplifier, we perform the linear stability analysis using modified Floquet procedure [Kum14]. Floquet stability analysis for a spatial homogenous system is straight-forward due to coupling between only the harmonics of complex perturbations at $+k_x$ and $-k_x$. In such case, 4 independent perturbations corresponding to each perturbation $a_{\pm}(k_x)$ modes are required and, in the end, the linear evolution matrix (4x4) as a function of k_x is obtained. However, in case of the periodic spatial nonhomogeneous system, the procedure is revised to introduce the additional coupling effect between spatial harmonics. The transverse-longitudinal modulation induces a linear coupling between spatial harmonics of the perturbations; $k_x, k_x \pm q, k_x \pm 2q$. Therefore, each coupled harmonics is perturbed here independently for

each k_x. The resultant evolution matrix has dimensions of $(4n \times 4n)$, where n characterizes the number of spatial harmonics considered for analysis. We consider four harmonics to check the system stability due to a weak influence of higher order harmonics. The linear evolution matrix of perturbations is calculated by integrating over one longitudinal period . The exponential growth of the diagonal elements of the linear evolution matrix determines the Lyapunov exponents, $\lambda_{Re}(k_x)$. The sign of Lyapunov exponents indicates the system stability, which depends on the exponential growth (unstable) or decay (stable) of the perturbation.

The parameter space (m_1, m_2) is explored at resonance, $Q = 1$, to plot the stability map as a function of the maximum Lyapunov exponents, $\lambda_{Re,max}(k_x)$ [see Fig. 4.13(a)]. The white region, encircled with a black curve, corresponds to the complete stabilization, for which $\lambda_{Re,max}(k_x) \leq 0$. It is evident that after introduction of a small index modulation, $m_2 \neq 0$, the combined effect of pump and index modulations completely stabilizes the system. The eigenvalues for the representative points, showing complete and partial stabilization of the system, are provided in Fig. 4.13(b) and Fig. 4.13(c), respectively. In both cases, the Lyapunov exponents of the modulated system lay below the dotted curve corresponding to the unmodulated unstable case. When all Lyapunov exponents are negative, the system is fully stabilized case [see Fig. 4.13(b)].

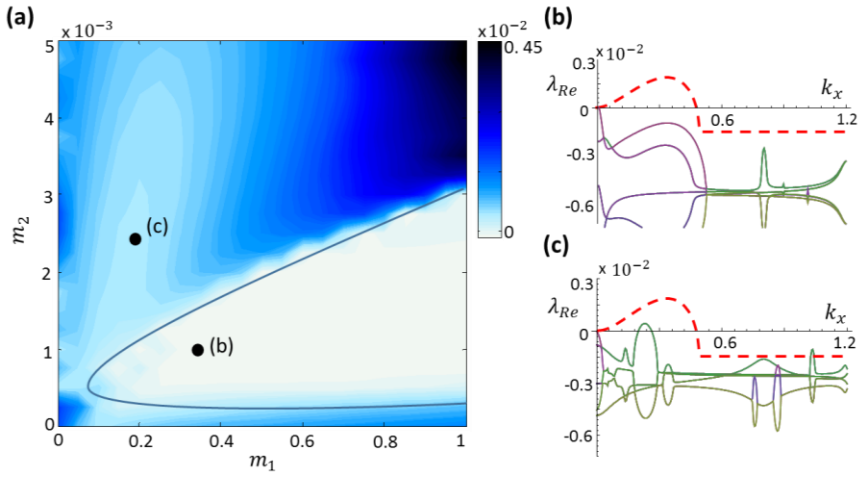

Figure 4.13. (a) Stability map obtained from the modified Floquet stability analysis for $\alpha_H = 2,\ p = 1.2, s = 0.03\mu m^{-1},\ k_0 = 2\pi\mu m^{-1},\ n = 3.3$ and $\gamma = 0.1$. The real eigenvalues curves, Lyapunov exponents, are shown for complete stabilization in (b) and partial stabilization with remaining instability in (c).

The Floquet stability results are further confirmed by the direct numerical integration of the unmodulated and modulated BAS systems, as shown in Fig. 4.14(a) and Fig. 4.14 (b), respectively. The left and right panels, in both cases, represent the field evolution and corresponding angular spectrum during propagation. For the unmodulated case, a chaotic behavior is clearly observed which is also evident from the wide range of unstable wavevectors in the corresponding spectrum. On the other hand, such chaotic behavior may be eliminated in the presence of pump and index modulations resulting in complete stabilization. The spatiotemporal dynamics confirms the results obtained from the Floquet stability analysis, exhibiting a perfect consistency between the predictions and the direct numerical integration of the model.

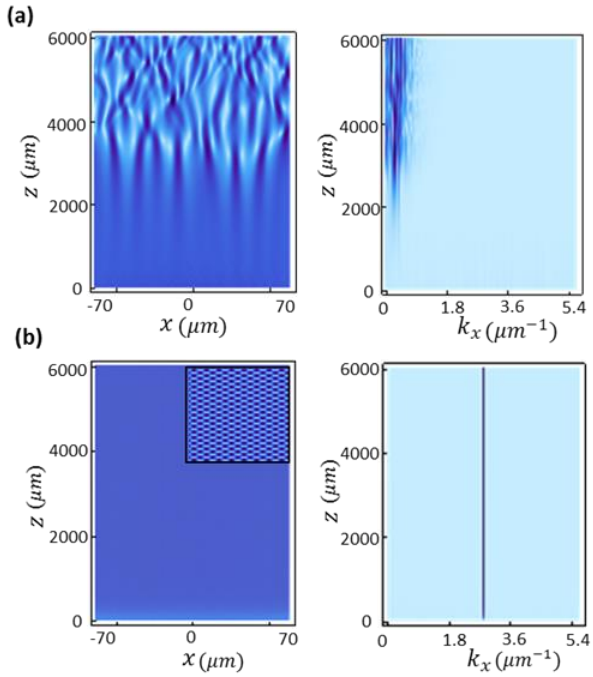

Figure 4.14. Direct numerical integration results: (a) unmodulated case, (b) 2D doubly-modulated case exhibiting complete stabilization. In (a,b), left column shows the field profiles and right column shows the corresponding angular spectrum. The zoomed-in view of the field in modulated cases is depicted in the inset. The simulation parameters are width= $140\mu m$, $\alpha_H = 2$, $p = 1.2$, $s = 0.03\mu m^{-1}$, $\gamma = 0.1, k_0 = 2\pi\mu m^{-1}, n = 3.3, d_\perp = 2.2\ \mu m$ and $d_\parallel = 32\mu m$.

Next, we extend our analysis on the stability of modulated BAS by exploring the parameter space (m_1, m_2) for different α_H values. The stability of the system is reduced when increasing α_H values, and it is in agreement with the increasing range of unstable wavenumbers shown in Fig. 4.11(a). Therefore, it becomes more difficult to stabilize the BAS amplifiers through modulations for large α_H. Floquet stability maps for $\alpha_H = 3$ and $\alpha_H = 4$ in Fig. 4.15 depict this diminishing stability. As we expected, the stability region is shrunk for $\alpha_H = 3$ [see Fig.4.15 (a)], and it

becomes very tiny in the case of $\alpha_H = 4$. For large α_H, higher amplitudes of pump modulation are required for stabilization which compensate the focusing effect enhanced through pump modulation.

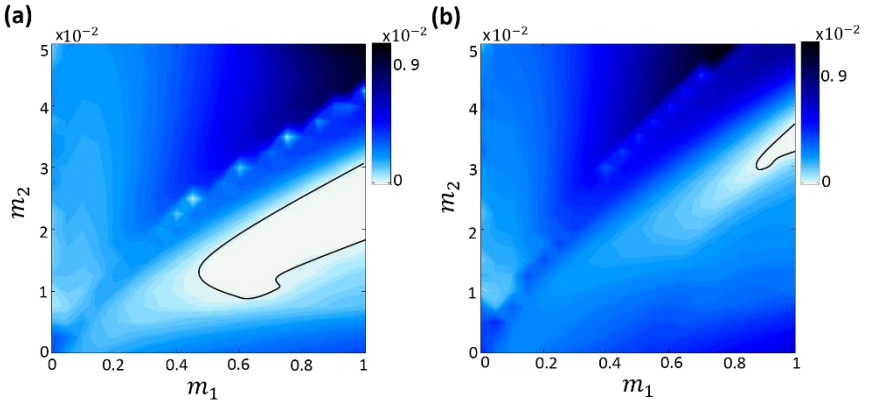

Figure 4.15. Stability maps calculated from modified Floquet procedure at $Q = 1$ for different linewidth enhancement factor (a) $\alpha_H = 3$ (b) $\alpha_H = 4$.

Furthermore, we perform a quantitative analysis to determine the stabilization performance of doubly-modulated BAS amplifier. In order to explore the neutral instability curve, we calculate the minimum value of linewidth enhancement factor, α_H, up to which full stabilization is obtained for different pump levels. We determine the neutral instability curve for different bounds of the pump modulation amplitude [see Fig. 4(a)]. Note that the range of unstable wavenumbers in the spectra increases with the pump above threshold. The results indicate that α_H decreases for higher pump currents. The general trend of the neutral instability curve remains same when restricting the pump modulation amplitude. The curve is shifted upwards by increasing the limit of m_1, i.e. $m_1 \leq 1$. This restriction also has a physical interpretation since these systems are always modulated with

a weak modulation to avoid additional detrimental spatial and temporal effects.

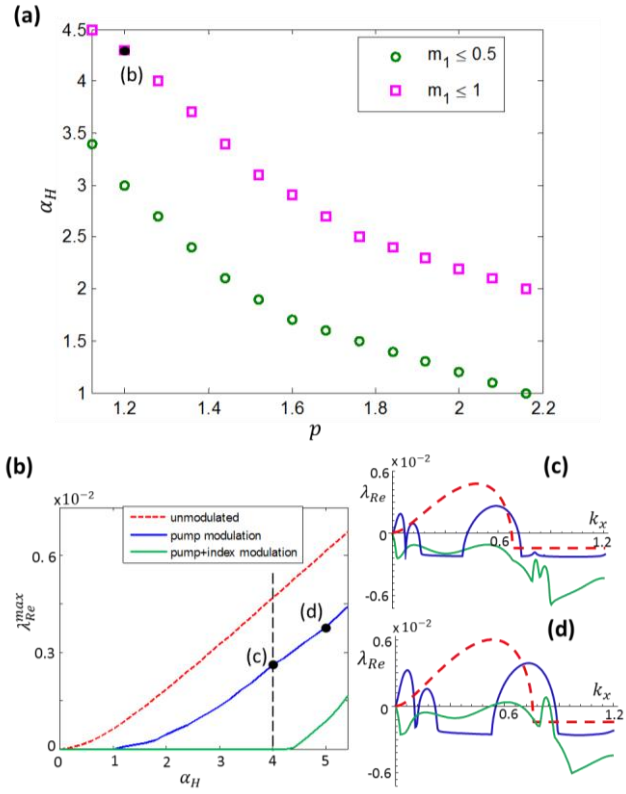

Figure 4.16. Stabilization performance of BAS amplifiers. (a) Minimum linewidth enhancement factor, α_H, for which stabilization is achieved as a function of the pump parameter, by restricting the amplitude of the pump modulation, m_1. (b) Comparison of the doubly-modulated, pump plus index, proposed configuration with only pump modulation, as a function of the linewidth enhancement factor for p=1.2. (c,d) Lyapunov spectra for α_H = 4 and α_H = 5 for the unmodulated (red dotted), only pump modulation (blue) and doubly-modulated (green) systems. The stabilization is significantly enhanced in case of pump and index modulation as compared to only pump modulation.

Finally, we fix the pump current and study the stabilization performance as a function of α_H. We determine the maximum remaining Lyapunov exponent after stabilization for only pump modulation (blue curve), simultaneous pump and index modulations (green) and compare them with the unstabilized case (red dotted curve) [see Fig. 4.16(b)]. We find that, as expected, only introducing a modulation in the pump only allows complete stabilization up to $\alpha_H \approx 1$, while the stabilization is more robust and efficient for a simultaneous modulation of pump and index profiles, reaching stabilization for substantially high linewidth enhancement factors, up to $\alpha_H \approx 4.5$. The Lyapunov spectra for high nonlinearities, $\alpha_H = 4$ and $\alpha_H = 5$ are provided in Fig. 4.16(c) and Fig. 4.16(d), respectively, showing complete and partial stabilization for the doubly-modulated BAS system.

4.3.5 Summary

To conclude, we propose that simultaneous 2D modulations of pump and index profiles provide an efficient scheme to stabilize BAS lasers and amplifiers. The proposed configuration can completely eliminate the MI in highly nonlinear regimes ($\alpha_H > 4$), with appropriate parameters. We explore the parameter space to determine the MI free regions, showing that best stabilization occurs around the resonance of both modulations, for $Q = 1$. Moreover, we perform an analysis of the stabilization performance of the device in terms of the linewidth enhancement factor and the pump parameter for the doubly-modulated BAS laser source. The proposal could be implemented with actual nanofabrication techniques, being moreover compact, contrary to other approaches to improve the emission from BAS laser sources.

4.4 Vertical-External-Cavity Surface-Emitting Lasers (VECSELs)

VCSELs and VECSELs are versatile coherent light sources due to their compactness, high conversion efficiency, single longitudinal mode operation, low lasing threshold and circular profile of the emitted beam [Iga88]. However, such lasers show a complex spatiotemporal behavior finally developing self-focusing, filamentation and spatial hole burning which deteriorate the output beam profile [Oht12, Tar98]. This complex behavior arises from the spatial instability of the homogeneous solution caused by the self-focusing effect. The lack of intrinsic mode selection mechanisms allows the instabilities to multimodal spatiotemporal chaos and turbulence. Therefore, the stabilization of such lasers is an important issue for practical applications.

In literature, great research efforts have been invested to determine the origin of the chaotic behavior and spatial instabilities in laser systems since the late 1970s, but less effort has been devoted so far to propose the solutions to avoid these chaotic instabilities. The reported approaches to control the spatiotemporal dynamics of semiconductor lasers are based on external forcing techniques [Sal85, Reg96, Mun97, Wol99], which reduce the main advantage of VCSELs lasers their compactness and thus limit their applicability. The chaotic spatiotemporal dynamics in VCSELs is originated due to the occurrence of modulation instability (MI), which leads to an ill-focused output beam by breaking the beam profile into filaments. In the conventional VECSELs, external spherical curved mirrors are used to select the fundamental transverse mode (TEM_{00}) and get rid of dynamical instabilities in nonlinear regimes [Tro06]. Such configuration, however, restricts the output power and compactness of the device. Whereas in mm-long cavities, the output power is limited by the small size of the single-

mode focal spot in the amplifying medium, in cm-long cavities, the focal spot size can be larger, but the advantage of compactness is lost. It also introduces several disjoined elements which reduce the robustness of the device. Moreover, long external resonators and external feedback designs in these lasers lead to additional unfavorable temporal effects such as linewidth broadening, coherence collapse and intensity noise enhancement [Ho93, Law98]. The possibility to use a flat output mirror in VECSELs would allow for the realization of relatively compact and robust devices with higher output powers. However, the modulation instability problem remains and, thus should be solved in this case. Therefore, at present, there is a need for finding alternative physical mechanisms to eliminate MI in VCSELs and VECSELs. Recently, a new idea to suppress MI in a broad class of spatially extended nonlinear dynamical systems was proposed [Kum15], relying on the introduction of a simultaneous periodic modulation in space and time. Inspired by this idea, we intend to use a periodic spatiotemporal modulation of the pump current in VECSELs to achieve a suppression of the MI of the system, leading to the stabilization of the output beam. In this section, we demonstrate that a stabilization of flat mirror VECSELs is possible by applying a periodic spatiotemporal modulation of the pump current. We consider three laser characteristic regimes to analyze the stabilization performance of VECSEL, i.e. Class-A, Class-B and intermediate regime. Class-A laser regime, where a cm-long cavity results in a photon lifetime, τ_p , longer than the nonradiative carrier recombination time, τ_N , $\tau_N \ll \tau_p$; Class-B laser regime, with μm-long cavities and shorter photon lifetimes, $\tau_N \gg \tau_p$, and an intermediate laser regime with $\tau_N \approx \tau_p$. The spatial field dynamics of all three cases can be described by the same physical model [Spi98], due to the same nature of the active media. Relaxation oscillations are absent for the relatively long Class-A and

intermediate lasers, characterized by large values of the relative carrier relaxation rate, $\gamma = \tau_p/\tau_N \approx 1 - 10$. On the other hand, few μm-long VCSELs, with τ_p and τ_N of the order of ps and ns, respectively, exhibit the intrinsic relaxation oscillations as typical in Class-B lasers [Uch12]. As a consequence, contrary to the case of VECSELs, relaxation oscillations are inherent in VCSELs due to the small relative relaxation rate, $\gamma \approx 0.01$. Besides, flat mirror VECSELs in all above discussed limits exhibit chaotic oscillations due to MI. The typical far and near field output intensity distributions, showing chaotic dynamics in the intermediate regime, are depicted in Fig. 4.17(b) and 4.17(c), respectively.

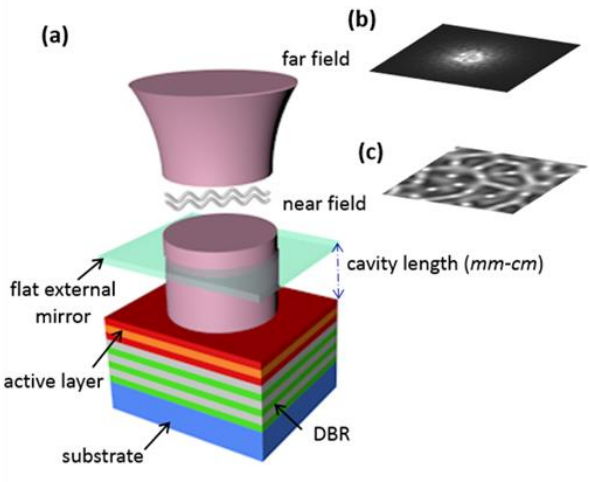

Figure 4.17. (a) Schematic diagram of a VECSEL with a flat external mirror (b) Near-field and (c) far-field distributions showing the typical complex dynamics in intermediate laser regime.

4.4.1 Mathematical model

We consider a well-established model, adopted from [Spi98], to describe the dynamics of flat mirror VECSELs and VCSELs. The coupled paraxial model describes the mean field dynamics of the complex field amplitude, E, and carrier density, N , in active region as:

$$\partial_t E = -\left[1 + i\theta + 2C(i\alpha - 1)(N - 1)\right]E + i\nabla_\perp^2 E \qquad (4.12a)$$

$$\partial_t N = -\gamma\left[N - I_p + |E|^2(N - 1)\right] + \gamma d\nabla_\perp^2 N \qquad (4.12b)$$

where θ is the cavity detuning parameter, α is the linewidth enhancement factor of the semiconductor, and $\gamma = \tau_p/\tau_N$ is the relative relaxation rate. The time, t, is normalized to the photon life-time, $\tau_p = 2L_c/vT_c$, which depends on the transmitivity factor, T_c, velocity of light, v, and cavity length, L_c .The transverse spatial coordinates (x, y) are normalized to $\sqrt{\lambda_0 L_c/2\pi T_c}$, where λ_0 is the central wavelength of the emission. The parameter C represents the interaction between carriers and field, and depends on the laser differential gain and the photon relaxation rate. The transverse Laplacian operator $\nabla_\perp^2$, describes the paraxial diffraction and carrier diffusion in the transverse direction. The pump current, I_p , generates the carriers within the active region, which diffuse in the transverse direction according to the diffusion factor d. The interaction between carriers and the electromagnetic field is either the absorption or stimulated emission depending on the sign of the $(N - 1)$ term in the Eq. (4.12b). The linewidth enhancement factor is a crucial parameter for semiconductor lasers. Note that for usual semiconductors in amplifying regimes $(N - 1) > 0$, the factor $\alpha > 0$, which leads to self–focusing effects.

4.4.2 Linear stability analysis

Similar to BAS amplifier case, we perform a standard linear stability analysis to determine the instability spectrum for the unmodulated 1D system. Following the standard procedure, first, we determine the stationary steady state of the system by setting the spatial and temporal derivatives equal to zero in Eqs. (4.12a) and (4.12b). The resultant homogeneous solution (E_0, N_0) of the system is: $N_0 = 1 + 1/2C$ and $E_0 = ((I_p - N_0)/N_0 - 1)^{1/2}$. Note that the field generally can contain the frequency and phase factors $e^{i\omega t}$ and $e^{i\varphi}$ which can be eliminated by a suitable choice of the reference frequency or detuning, $\theta = -\alpha$. Next we introduce a small perturbation to the stationary state (E_0, N_0) in the form of $E(x,t) = E_0 + e(t)cos(k_x x)$ and $N(x,t) = N_0 + n(t)cos(k_x x)$ where $|e/E_0|, |n/N_0| \ll 1$. The perturbations are assumed to be in the transverse direction, they are modulated by a wavenumber, k_x, and exponentially grow or decay in time. By neglecting higher order harmonics of e ,and n, we derive the following jacobian matrix of the linearized equations:

$$\mathcal{J} = \begin{bmatrix} -\left(A_1 + i(A_2 + k_x^2)\right) & 0 & -2C(i\alpha - 1)E_0 \\ 0 & -\left(A_1 - i(A_2 + k_x^2)\right) & 2C(i\alpha + 1)E_0^* \\ A_3 E_0^* & A_3\, E_0 & -\gamma\,(A_4 + dk_x^2) \end{bmatrix} \quad (4.13)$$

where $A_1 = 1 - 2C(\,N_0 - 1)$, $A_2 = \theta + 2C\alpha(\,N_0 - 1)$, $A_3 = -\gamma(\,N_0 - 1)$ and $A_4 = 1 + |\,E_0|^2$. The eigenvalues of $\mathcal{J}$ can be calculated numerically to determine the unstable growing modes of the system. The real value of such eigenvalues provides the instability spectrum, showing the bandwidth of unstable growing modes that varies from 0 to $k_c = \sqrt{2\alpha\,(\mu - 1)/\mu}$, where $\mu = 2C\left(I_p - 1\right)$ stands for the normalized pump parameter when

the laser threshold is 1 [Pra07b]. The real part of the main eigenvalues for different normalized carrier decay rates, is shown in Fig. 4.18. Note that the range of unstable wavenumbers in instability spectrum doesn't depend on carrier decay rate, resulting in k_c = 0.47 for particular parameters in all three characteristic regimes. These growing unstable modes are responsible for the chaotic spatiotemporal dynamics of the system.

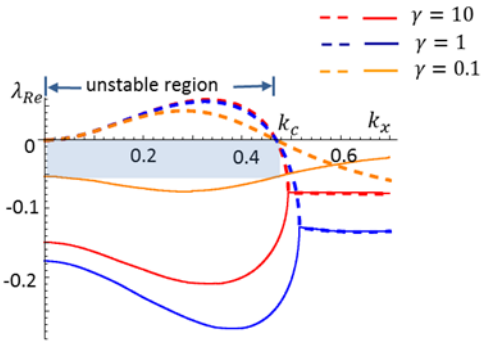

Figure 4.18. Analytically calculated eigenvalues showing the spectra of the main Lyapunov exponents of the linearized system, as a function of the lateral perturbation wavenumber, for different normalized carrier decay rate, γ, corresponding to the three analyzed regimes: Class A ($\gamma = 10$), intermediate ($\gamma = 1$) and Class B ($\gamma = 0.1$). In all cases $\alpha = 1.5$, $C = 0.6$, $\theta = -1.5$, $I_0 = 1.9$, $d = 0.052$. The dashed lines indicate the positive, unstable branch.

4.4.3 Spatiotemporal modulation of the pump

The spatiotemporal modulation can be introduced in the system in several ways. The pump current modulation is considered here for introducing the spatiotemporal periodic modulation in the form:

$$I_p = I_0 + 4mcos(q_x x)\cos(\Omega t) \tag{4.14}$$

where m, q_x and Ω are the amplitude, and the spatial and temporal frequencies of the modulation, respectively. The modulations are assumed on small space and fast time scales, satisfying the conditions: $|q_x| \gg |k_x|$ and $|\Omega| \gg |\lambda|$, with k_x and λ being the typical transversal wavenumber and complex frequency of the growing instabilities, repectively. The modulation amplitude, m, is restricted to $4m < I_0$, in order to keep I_p positive at every instant of time, t, and at each spatial position, x. This restriction, however, can be in principle removed by considering special and unusual designs of VECSELs, e.g. containing additional absorbing (un-pumped) layers of semiconductor material.

4.4.4 1D Stabilization results

The steady-state solution of Eq. (4.12) with pump modulation can be expressed in terms of the spatiotemporal harmonics of the modulation with the constant amplitudes, the so-called spatiotemporal Bloch modes. The resonance between the fundamental mode and the harmonics of the modulation of the pump influences the dispersion profile of the system. The resonance phenomenon is most pronounced when the ratio between the temporal and square of the spatial modulation, $Q = \Omega/q_x^2$, equals, or is close to, 1, where Q is the resonance parameter.

In this section, we numerically analyze the stability of the stationary Bloch mode solution of the pump modulated VECSELs in different regimes, using a modified Floquet and direct integration method. The modified Floquet procedure is the same as we explained in section 4.3.3. The only difference is that here we consider complex perturbation for both complex field, $e_{\pm}(k_x)$ and population, $n_{\pm}(k_x)$. As a result, we obtain (32x32)–dimensional evolution matrix calculated after integration over one temporal period, $T = 2\pi/\Omega$. The eigenvalues of the resulting evolution matrix are the

characteristic multipliers, μ_k, related to the Floquet exponents λ_k by $\mu_k = exp(\lambda_k T)$, and to the Lyapunov exponents, $\lambda_{k,Re}$, which are the real parts of λ_k. The state is modulationally stable only if all Lyapunov exponents are non-positive.

Intermediate VECSELs regime

In case of a mm-long optical cavity, the normalized carrier decay rate is $\gamma \approx 1$ and VECSELs operate in a relaxation free laser regime. In this regime, a periodic spatio-temporal modulation of the pump current can completely stabilize the VECSELs, for appropriate modulation amplitudes and resonance parameters. We find that different sets of parameters may lead to enhancement, partial suppression or complete suppression of the MI. The most representative cases showing the complete suppression as well as different kinds of partial suppression of instabilities are shown in Fig. 4.19.

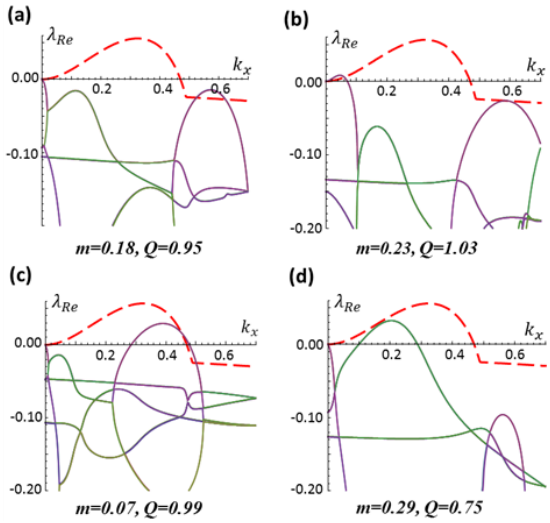

Figure 4.19. Spectrum of the Lyapunov exponents for 1D modulated VECSELs in the intermediate regime as calculated numerically using the modified Floquet

procedure. The parameters used are as in Fig. 4.18 with q_x =1.4. Solid lines display the different branches of the Lyapunov exponents for a given parameter set (Q, m), while the dotted line represents the largest Lyapunov exponent of the non-modulated case for comparison. Complete stabilization (a). Partial stabilization with remaining weak LW (b) and SW (c, d) instabilities.

The red dashed curve in the figures represents the largest Lyapunov exponent of the non-modulated (unstabilized) case for comparison. The case of complete stabilization is shown in Fig. 4.19(a), where all Lyapunov exponents are non-positive. In case of partial stabilization, the largest Lyapunov exponent for k_x from a limited interval is still positive, and weak MI is still present. The spatial instabilities are generally classified [Cro93] as long-wavelength (LW) and short-wavelength (SW) modulation instabilities depending on whether the k_x-unstable range touches [see Fig. 4.19(b)] or does not touch [Fig. 4.19(c, d)] the axis $k_x = 0$, respectively.

In order to identify the regions of complete and partial stabilization, we build a stability map in the parameter space (Q, m) by color encoding the maximal Lyapunov exponent of the linear evolution matrix, $\lambda_{Re,max} = max_{k_x}\lambda_{Re}(k_x)$, as shown in Fig. 4.20(a). In fact, we identify two islands of stabilization in (Q, m) space. One is located close to resonance $Q \approx 1$, and within the physically realistic limit of the modulation depth $4m < I_0$. The other island is located far from resonance, i.e. at $Q \approx 0.3$, and for above the physical limit, i.e. $4m > I_0$. The white areas represent the regions of complete stabilization where all the Lyapunov exponents are non-positive $\lambda_{Re}(k_x) \leq 0$. The light blue areas in the same stability map represent regions of partial stabilization, where weak LW and SW instabilities remain. The parameter sets for complete and partial stabilization discussed in Fig. 4.20 are indicated in the map by solid dots (a, b, c, d). The black

areas in the map represent regions where we were not able to locate stationary Bloch mode solution. This region is obviously excluded from the stability analysis. In order to classify the bifurcations by crossing the boundaries of stability balloon, we explored the remaining weak instabilities: we build another map in the parameter space (Q ,m), for the dominant wavenumber $k_{x,max}$, defined as $\lambda_{Re,max} = \lambda_{Re}\left(k_{x,max}\right)$ [see Fig. 4.20(b)]. The stable region is thus surrounded by the areas of partial stability with remaining LW and SW instabilities.

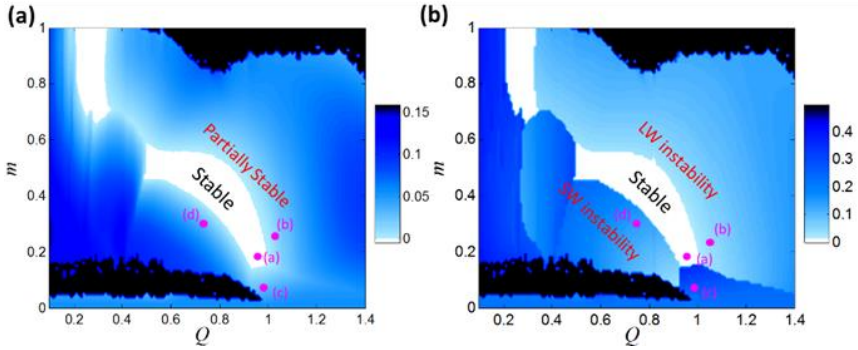

Figure 4.20. (a) Stability map calculated from the largest Lyapunov exponent $\lambda_{Re,max}$ in the (Q, m) parameter space (b) map of the corresponding dominant wavenumber, $k_{Re,max}$. The parameters used are the ones of Fig. 4.18 with q_x =1.4.

To confirm the predictions of the modified Floquet linear stability analysis, we explored the spatiotemporal dynamics of the model by direct numerical integration for the 1D case. The results are presented in Fig. 4.21. For the unmodulated case, the typical chaotic spatiotemporal behavior is observed, as shown in Fig. 4.21(a). On the other hand, we observe that for appropriate pump modulation parameters, the chaotic dynamics is reduced or eliminated, resulting in partial or complete stabilization as shown in Figs. 4.21(b,c,d).

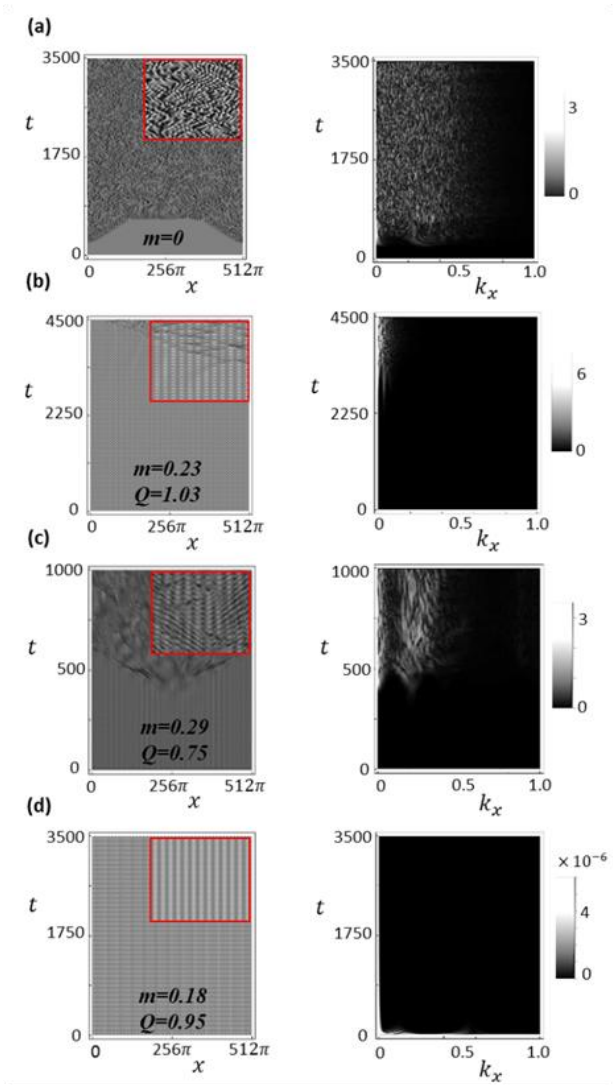

Figure 4.21. Calculated dynamics of spatiotemporally modulated 1D VECSELs in intermediate regime. Time evolutions of Field intensity (left) and spatial spectrum (right). The parameters used are the ones of Fig. 4.18 with q_x =1.4. The plots are for unmodulated (a) and modulated cases (b,c,d). Full stabilization is realized in (d). The small scale modulations are filtered out for clearer representation. The insets in the left column display zoomed-in views of the field intensity.

As expected, no modulation modes appear in the spatial spectrum at complete stabilization [see Fig. 4.21(d)]. Partial stabilization is shown in Fig. 4.21(b) and Fig. 4.21(c), where the instabilities are only partially suppressed, resulting in a narrower spatial spectrum upon propagation. The remaining weak SW and LW instabilities eventually render the dynamics chaotic after a long transient time, depending on the magnitude and spectral width of the remaining instabilities. For a clearer visualization of the spatiotemporal patterns, a magnified view of field dynamics is provided in the insets of Fig. 4.21. We observe that the results obtained from direct integration of the model perfectly agree with the modified Floquet linear stability analysis.

For an extensive comparison of these results with the results of the modified Floquet stability analysis, we analyze the stability of the system at different points in the parameter space (Q, m) by direct integration. The results are summarized in Fig. 4.22. The system's stability is determined by observing the spatiotemporal dynamics and corresponding spatial spectrum. We consider different parameter sets (Q, m) within the specified range, following the long-time dynamics of the modulated system (typically integration time of ~25000 units) from the initial homogenous state, perturbed by weak random δ-correlated in space perturbation. The stable and unstable regimes, obtained by numerical integration, are indicated in the map by a solid dot (•), and a cross (x) respectively. The completely stable regions, blue patches in Fig. 4.22, obtained from the modified Floquet stability analysis are shown in the map for comparison. Again, the stable points (•) from the numerical integration confirm the stable regime determined by stability analysis. We also find a bistable domain inside the blue shaded stabilization region of Fig. 4.22. Two different regimes are possible, depending on the initial conditions: The stable regime predicted

by the modified Floquet analysis and a turbulent regime. To identify the bistable domain we perform simulations of Eq. 4.12 with a fixed amplitude of pump modulation m but scanning the parameter Q in both senses. The comparison of the field dynamics allows us to distinguish a uniquely stable region delimited by the yellow curve and the bistable region located within the blue shaded area but outside the yellow curve. Inside the bistable region and depending on the initial conditions, the calculated solution was attracted either by the stable stationary Bloch mode solution or by a chaotic attractor. Note that bistability between different spatiotemporal dynamical regimes is generally typical for the intermediate regime of VECSELs, for instance as reported in rocked VCSELs in [Oto14].

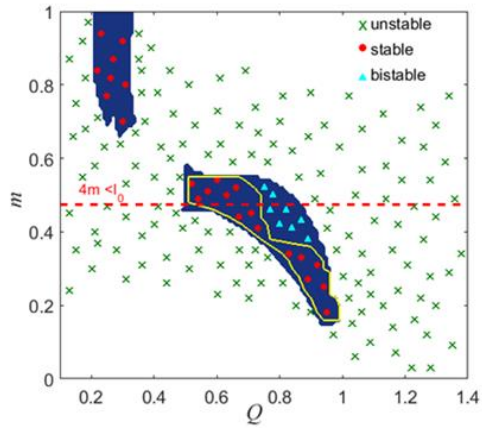

Figure 4.22. Stability map of modulated VECSELs in the intermediate regime as obtained from numerical integration. The parameters used are as in Fig. 4.18 with q_x =1.4. The area outside the yellow contour, but within the central blue region (indicated by triangles) represents bistable region. Symbols: direct numerical simulations of the nonlinear system. Shaded area: stability region according to the modified Floquet analysis. 4. The limit for the modulation amplitude of common VECSEL configurations (i.e. $4m < I_0$) is represented by a horizontal red dashed line.

Class-A regime

Next, we investigate the stability of VECSELs in Class-A limit. In this case, the normalized carrier decay rate reaches $\gamma \approx 10$, belonging to cm-long optical cavities. This is compatible with the general conclusion that unstable spatio-temporal dynamics are more pronounced for Class-B lasers than for Class-A lasers [Sta03]. We find that it is easier to suppress MI in this case. We perform the numerical stability analysis following the procedure as in section IV and explore the parameter space (Q, m) to determine the complete and partial stabilization regions. The results are summarized in Fig. 4.23(a). The stability region is slightly enhanced as compared to the intermediate case of VECSELs. The spectra of the Lyapunov exponents for the most representative points (c,d,e) of the parameter space (Q, m) show either complete or partial suppression of MI, as depicted in Fig. 4.23.

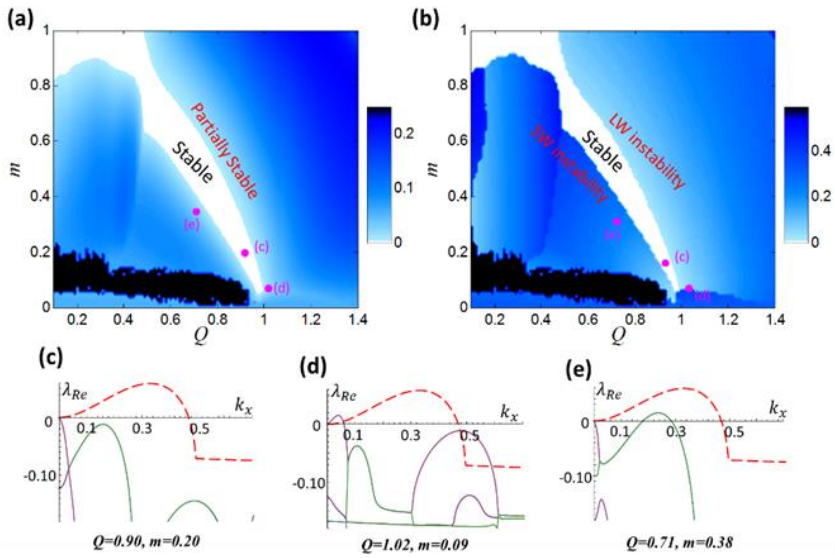

Figure 4.23. (a) Stability map obtained from the largest Lyapunov exponent, $\lambda_{Re,max}$ (b) map of the corresponding dominant wavenumbe, $k_{Re,max}$, in the (Q, m)

parameter space for Class-A VECSELs with γ =10 and q_x=1.8. Other parameters are the ones of Fig. 4.18. Main Lyapunov exponents (solid lines) for each particular parameter set, as compared to the largest exponent (red dashed line) of the unmodulated case. Complete and partial stabilization with remaining weak LW and SW instabilities are shown in panels (c), (d) and (e), respectively.

The dynamical equations for Class-A lasers ($\gamma \approx 10$) can be simplified by adiabatically eliminating the population inversion. Particularly, for small field intensities, a set of model equations (4.12) can be reduced to a single nonlinear field equation:

$$\partial_t E = -\left[1 + i\theta + 2C(i\alpha - 1)\left(I_p - 1\right)(1 - |E_0|^2)\right]E + i\nabla_\perp^2 E \quad (4.15)$$

analog to the well-known complex Ginzburg-Landau equation (CGLE). The complex potential of such CGLE is periodically modulated due to the modulation of the pump current. In this way, the stabilization of modulated VECSEL in Class-A limit is compatible to the stabilization of the modulated CGLE [Kum15]. Different versions of the CGLE have been derived for Class-A and Class-C laser models [Cou89, Opp91, Sta93], in contrast to Class-B lasers where the models are not reducible to a single equation of the CGLE type [Sta03, Opp09].

Class-B regime

The analysis for short cavity Class-B VECSELs shows that the stabilization of VECSELs in this regime is more challenging. However, the results of the stability analysis demonstrate that full stabilization is also possible in Class-B lasers with cavity lengths down to $\sim$100 μm. We consider a normalized carrier decay rate of the order of $\gamma \approx 0.1$, corresponding to the limiting case of a $\sim$100 μm-long cavity. The complete suppression of MI

can still be achieved for $\gamma \approx 0.1$, by an appropriate choice of the modulation parameters. In this case, higher modulation amplitudes are required as compared to Class-A and intermediate VECSELs, due to intrinsic relaxation oscillations. The stabilization region in parameter space is reduced, a tiny island [see Fig. 4.24], as compared to Class-A and intermediate VECSELs. We also note that bistability is obtained in all stabilized regimes for Class-B VECSELs (compare with Fig. 4.22).

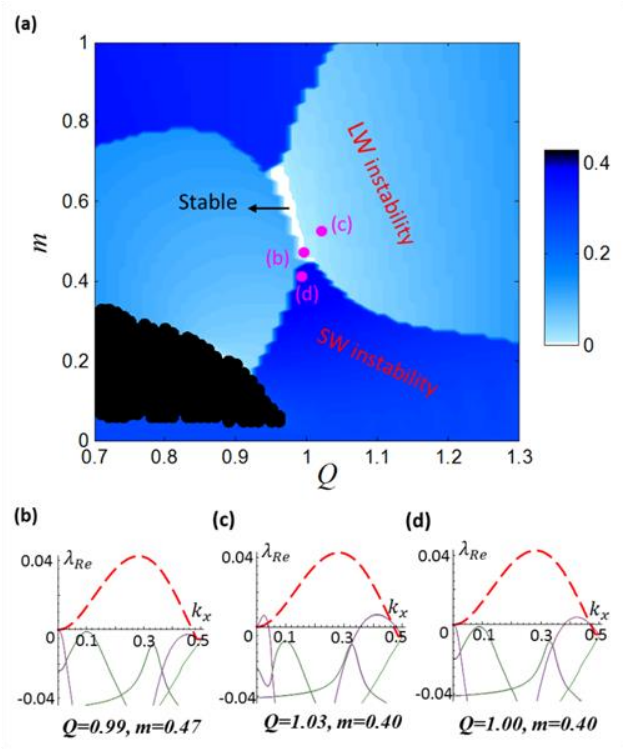

Figure 4.24. (a) Stability map from the largest Lyapunov exponent $k_{Re,max}$ in the (Q, m) parameter space for Class-B VECSELs with γ = 0.1 and q_x=1.0. Other parameters are the ones of Fig. 4.18. The other plots show the main Lyapunov exponents (solid lines) for each particular parameter set, as compared to the largest exponent (red dashed line) of the unmodulated case. Complete stabilization is

obtained in (b), partial stabilization with remaining weak LW and SW instabilities in (c) and SW instability alone in (d).

4.4.5 2D Stabilization results

Finally, we extend our analysis of VECSELs to the 2D space. The modulation of the pump current in two dimensions is of the form:

$$I_p = I_0 + 4\left(m_x cos(q_x x) + m_y cos\left(q_y y\right)\right)\cos(\Omega t) \qquad (4.16)$$

where, m_x, m_y are the modulation amplitudes along x-axis and y-axis and q_x, q_y are the corresponding spatial frequencies of the modulation. Similar to the 1D case, the modulation is also considered on small space and fast time scale, hence satisfying the conditions: $|q_x| \gg |k_x|$, $|q_y| \gg |k_y|$ and $|\Omega| \gg |\lambda|$, where k_x, k_x and λ are the typical transverse wavevectors along *x*- and *y*-axis and the complex frequency of the growing instability, respectively.

In 2D case, we perform the stability analysis only using the direct integration method. The typical results of numerical integration for certain parameter sets are shown in Fig. 4.25. The numerically calculated patterns represent the state of the system after a long transient time (t~400). A snapshot of the chaotic patterns of the system for the unmodulated case is shown in Fig. 4.25(a). The circular disk in the corresponding spatial spectrum indicates the growth of instabilities in the system. When modulation is introduced only in one direction, i.e. $m_x \neq 0, m_y = 0$, we observe, as intuitively expected, the suppression of instabilities in that particular direction only [see Fig. 4.25(b)]. It is evident from the spatial spectrum that the circular disk is fragmented due to the suppression of

instabilities along the modulated axis while the remaining instabilities along the vertical direction generate the resultant partially chaotic pattern. Next, we consider modulation with a square symmetry, i.e. $q_x = q_y$ and $m_x = m_y$. A partial stabilization of the system is achieved for the amplitudes ($m_x = m_y = 0.21$), as shown in Fig. 4.25(c). Here, a weak and slowly growing MI disrupts the square symmetric pattern after a long time of propagation. This weak instability is more clearly seen in the spectrum of Fig. 4.25(c). For the modulation amplitude, $m_x = m_y = 0.15$, we have complete stabilization of the system, as shown in Fig. 4.25(d), where the square pattern remains stable even after a long transient time.

The general conclusion from the 2D results is that the stabilization studied in 1D case works also for 2D cases. However, 2D modulation offer richer possibilities than 1D case: different wavenumbers of q_x and q_y can be considered in case of rectangular modulation pattern, also different geometries of modulations (hexagonal, octagonal etc) can be considered for the generalization of the proposed scheme.

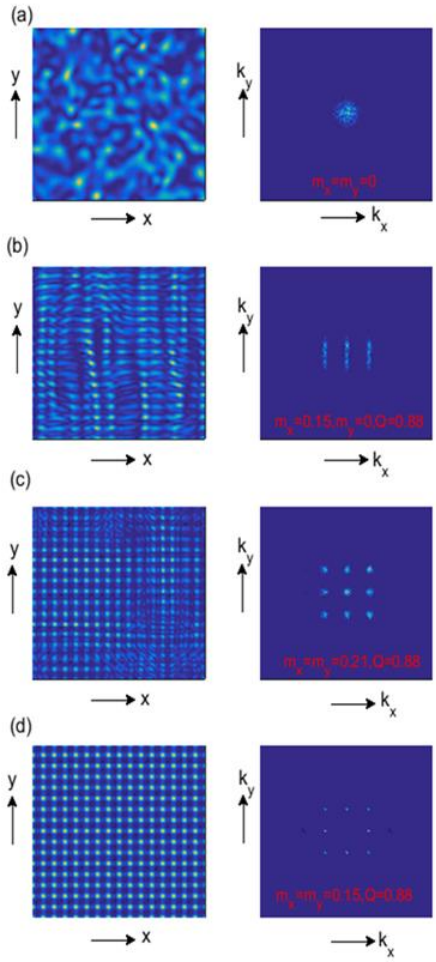

Figure 4.25. Numerically calculated snapshots of the intensity distribution patterns after a long transient time (t~400) for the 2D model, showing field intensity (left) and spatial spectrum (right). The parameters are as in Fig. 1(d) and the size of integration window is 100x100. (a) Chaotic intensity distributions and corresponding spectra for the unmodulated system. (b) Suppression of MI only in the horizontal direction. (c) Partial stabilization in both spatial directions for a weak square symmetric modulation and (d) complete stabilization for a square symmetric modulation of appropriate amplitude.

4.4.6 Summary

We propose a new design for VECSELs with external flat-mirror and theoretically demonstrate that such VECSELs can be efficiently stabilized by introducing a periodic spatiotemporal modulation of the pump current. The interaction of the spatial and temporal modes of the modulation allows suppressing MI in VECSELs which could enhance the stability of such lasers at higher powers and improve the spatial quality of the output beam. By using a modified Floquet analysis and direct integration methods, we calculated the MI free operating regions in the parameter space for VECSELs operating in different characteristic regimes. We paid special attention to the case of intermediate VECSELs, as the stabilization in this regime could have a maximum technological impact. We show that Class-A VECSELs can also be efficiently stabilized, thus making our stabilization technique well suitable for quantum dot VECSELs (which are characterized by significantly large values of carrier decay rate [Sha12]). Short cavity, Class-B laser VECSELs (and VCSELs) limit the stabilization since only lasers with length cavities down to around 100 μm can be completely stabilized by the proposed method. Long cavity VECSELs are not compact light sources and can, therefore, be stabilized by other means, such as by using spherical mirrors, as discussed in section 4.2. On the contrary, VECSELs of $\sim 1\, mm$ cavity, referred to as the intermediate case can be efficiently stabilized by the proposed method. This case is especially relevant and interesting as we need no regularization mechanisms (e.g., curved mirrors) for the improving the beam quality. The estimated frequency and period of the modulation required for the stabilization of VECSELs in such intermediate regimes are still achievable experimentally, being 10 GHz and 100 μm respectively.

4.5 PT-axisymmetric Semiconductor Lasers

In the previous sections, we discuss different stabilization approaches for BALs and VCSELs relying on the simultaneous transverse and longitudinal modulations. Here, we propose another elegant way to control the emission in semiconductor lasers using the concept of PT-axisymmetry. The basic idea of PT-axisymmetry to concentrate the light on the symmetry axis, $r = 0$, is explained in Chapter 2. We observed that light propagation through PT-axisymmetric potentials creates an extreme localization around $r = 0$, accompanied by a strong field enhancement. The localization of light in a central beam with the small width and high intensity opens the possibility to obtain spatially coherent laser light sources. Therefore, we apply the PT-axisymmetry concept in broad aperture microlasers to get bright and narrow beams for practical applications. This new class of semiconductors lasers, which we refer to *PT-axisymmetric lasers*, relies on the index and gain-loss modulations which could be implemented by advanced microfabrication techniques of microchip- and VCSEL lasers. The possible configurations of such lasers are schematically illustrated in Fig. 4.26.

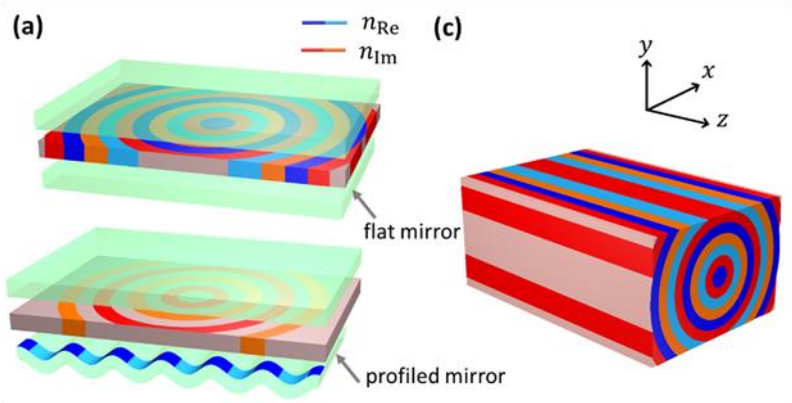

Figure 4.26. (a) 2D realizations in broad aperture microlasers (modified VCSELs)

with a modulated gain-layer and/or a modulated (micro-corrugated) mirror, with asymmetric spatial coupling of the fields evolving in time (d) 2D coaxial index and gain/loss modulations analogs to (a) and (c), with fields propagating along *z* instead of *t*.

4.5.1 Mathematical model

We consider the complex Ginzburg-Landau equation (CGLE), as a mathematical model, to describe the field dynamics of microlasers. In the simplest approximation, the field dynamics with the complex potential profile, $V(r)$, can be described as:

$$\partial_t A(r,t) = i\,\nabla^2 A(r,t) + (p - |A|^2)A(r,t) + iV(r)A(x,t) \qquad (4.17)$$

where $A(r,t)$is the envelope of complex field distributed in space, r, and p is the pump parameter. The main difference with the linear propagation along PT-axisymmetric potentials of Chapter 2 is the nonlinearity that here appears due to gain saturation. The PT-symmetric complex potential is written either in 1D, i.e. $V(x) = n_{Re}\,cos(|x|) - in_{Im}\,sin(|x|)$ or 2D, i.e. $V(r) = n_{Re}\,cos(r) - in_{Im}\,sin(r)$ as discussed in chapter 2.

From chapter 2, we know that light propagation along linear PT-axisymmetric systems exhibits a field localization phenomenon accompanied by an exponential growth in time. However, in case of laser systems above threshold, for $p > 0$, the field growth is limited by the system nonlinearity inducing field saturation at $|A| = \sqrt{p}$. Thus, a uniformly distributed field over the entire space is expected limiting the maximum output intensity. As a consequence, the field cannot be concentrated and localized at axis, and it becomes turbulent with average amplitudes near saturation. To solve this issue, we propose two possible approaches

allowing the field localization and enhancement at the central axis of these lasers. The first proposal, explained in section 4.5.2 is operating the laser with averaged pump below threshold and the second proposal, explained in section 4.5.3, is the inclusion of a linear defect around axis. We analyze these two strategies to evaluate the performance of PT-axisymmetric lasers and preliminary results are provided in next sections.

4.5.2 PT-axisymmetric lasers with averaged pump below the threshold

The first approach to obtain localized beams in PT-axisymmetric lasers is by applying averaged pump below the threshold, i.e. $p < 0$. Even the laser is pumped below the threshold, the additional complex PT-symmetric potential infers an effective modulated pump, with positive values at given laser areas [see Fig. 4.27]. The field generated in these areas is localized at axis by the PT-symmetric potential.

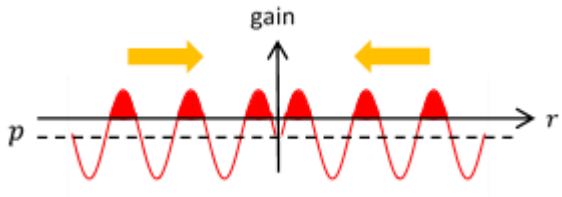

Figure 4.27. PT-axisymmetric laser when the averaged pump is below the threshold, $p < 0$. In this operation regime, the gain areas are generated due to effective pump induced by the PT-axisymmetric potential for field concentration at the axis.

We consider $p = -0.1$ and studied the dynamics of the PT-axisymmetric laser in below threshold regime. The results for a particular modulation parameter set are provided in Fig. 4.28. The spatial field profile showing

the concentration at the center, $r = 0$ reveals that this 2D axisymmetric system efficiently localizes the field.

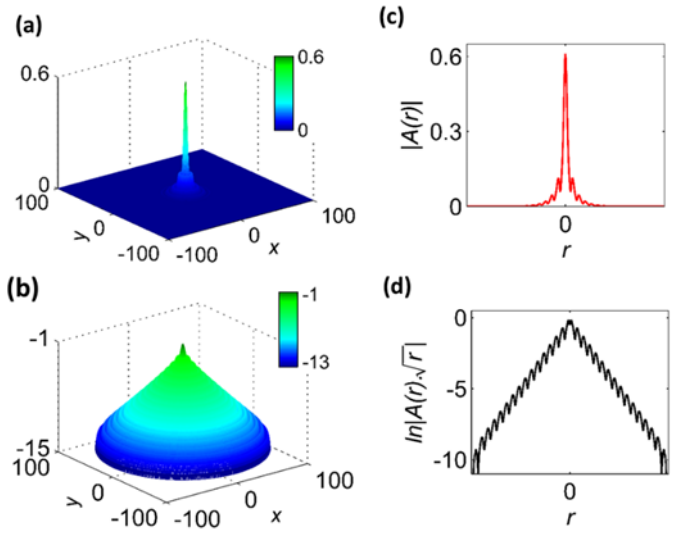

Figure 4.28. Spatial field distributions for a 2D PT-axisymmetric VCSEL, calculated after the steady state (t~150 units) for p = -0.1 and parameter set (0.4, 0.4). 3D visualization of the VCSEL output field profile, concentrated and enhanced at the center, r = 0 in real (a) and logarithmic (b) scales. (c)/(d) Axial cross-sectional profile the field in linear/logarithmic scale.

4.5.3 PT-axisymmetric lasers with central linear defect

When PT-axisymmetric lasers are operated above the threshold, the maximum intensity is limited due to saturation which inhibits the field concentration at the axis. The saturation given by system nonlinearity can be removed at the center, where field concentration is planned, by including a linear central defect of width, w_d, in 1D and 2D PT-symmetric potentials [see Fig. 4.29]. The elimination of the field saturation allows the localization on axis, leading to bright output beams.

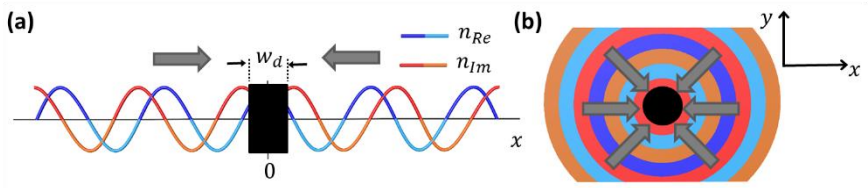

Figure 4.29. (a) 1D PT-axisymmetric complex refractive index, where n_{Re} is the real index modulation, and n_{Im} is the gain-loss modulation with a linear central defect of width w_d. Field concentration is obtained inside the linear defect. (b) 2D analogous PT-axisymmetric configuration where the arrows indicate the inwards coupling given by the PT-symmetry.

First, we investigate the 1D system, by numerically solving Eq. (4.16) with a PT-axisymmetric potential and a linear defect. A Gaussian profile is considered as initial beam in the form $A(x) = e^{-(x^2/w^2)}$, where w is its width, although the final beam profile does not depend on initial conditions. As already explained, in ordinary laser systems the field is uniformly amplified by the gain, and the maximum intensity of the output beam is restricted to the normalized pump intensity, p, due to saturation effect. The inclusion of a central linear defect in the structure avoids saturation around axis and allows a significantly large field localization at this point through the PT-axisymmetric potential. Thus, such PT-axisymmetric systems develop extraordinary field concentration and enhancement on axis after a sufficient evolution time and the field profile is characterized by a central peak with significantly larger intensity than the normalized pump and background.

Mainly, stationary, oscillatory and pulsed regimes are identified scanning the parameter space (n_{Re}, n_{Im}) for a fixed defect width. The different dynamical regimes are characterized by the average intensity of the central peak and the amplitude of the temporal oscillations. Figure 4.30 locates

these different behaviors in the complex refractive index (n_{Re}, n_{Im}) plane for a defect width, $w_d = 2$. The average intensity and oscillations amplitude are respectively plotted in Fig. 4.30(a) and Fig. 4.30(b) as a function of the modulation amplitude of the complex refractive index. We observe that the field is accumulated at the top right and bottom left regions, where the coupling direction enhanced by the PT-symmetry is inward (towards axis). The relative amplitudes of the index and gain-loss modulations are clue parameters to obtain a maximal intensity enhancement for stationary and oscillatory regimes. At the PT-phase transition ($n_{Re} = n_{Im}$), the stationary regime becomes unstable through a supercritical Hopf bifurcation arising the oscillatory regime. The oscillatory and stationary regimes are respectively localized by (c) and (d) points. The intensity profiles and evolution of peak intensity normalized with the mean intensity, I_m , are provided in Fig. 4.30(c) and Fig.4.30(d) for the corresponding points. The periodic oscillations for (c) clearly indicate the pulsating temporal behaviour for $|n_{Re}| < |n_{Im}|$ in top right and bottom left corners.

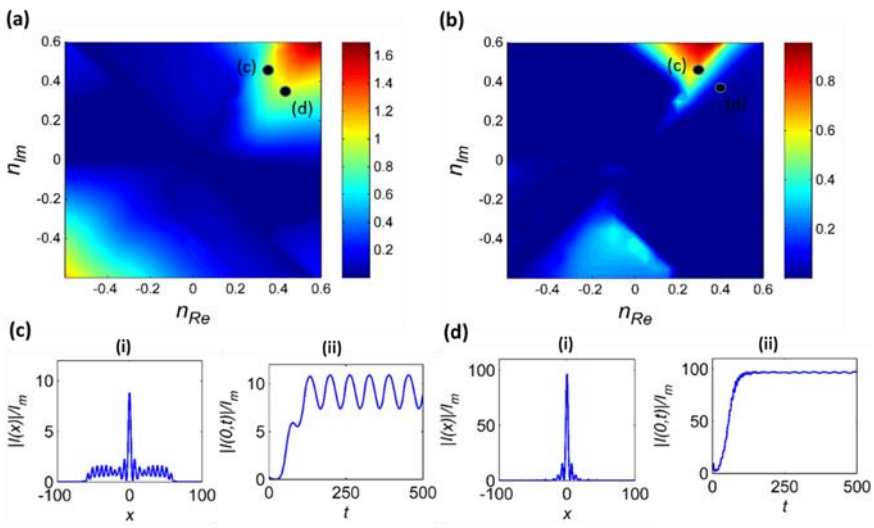

Figure 4.30. (a) Average normalized amplitude of the central peak intensity and (b)

Amplitude of the temporal oscillations for a pump, p=0.01 and a defect width, $w_d = 2$. Stationary regimes correspond to blue, while dark red values correspond to large amplitude oscillations. The two representative points marked as (c) with parameter set (0.35, 0.45), and (d) with parameters (0.4, 0.35), correspond to an oscillatory and to a stationary state, respectively. In both cases, the spatial intensity profiles and evolution of central average peak intensity normalized to the mean intensity, Im, are shown in (i) and (ii), respectively, revealing that intensity is increased by two orders of magnitude.

Finally, we analyze the 2D PT-axisymmetric laser system with a central defect. The 2D transverse space allows different geometries to be studied. In this work, we restrict the analysis to the radial geometry. Numerical results show analogous behaviors to the simple 1D case with similar field enhancement. The results for a particular parameter set are provided in Fig. 4.31. We observe a strong field enhancement at the center, $r = 0$, which can be attributed to the asymmetric radial coupling between inward and outward propagation waves. The axial cross-sectional profile of intensity and temporal evolution of the central peak intensity are show in Fig. 4.31(a) and Fig. 4.31(b), respectively.

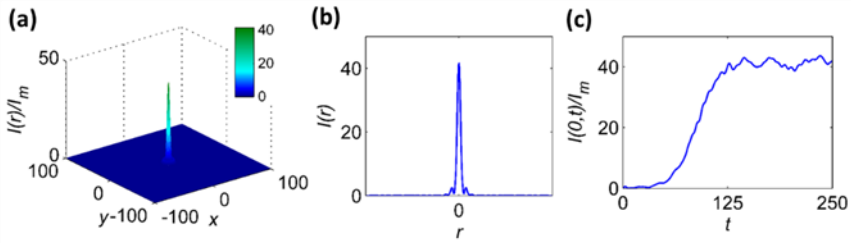

Figure 4.31. (a) Normalized Intensity profile after long time evolution for a normalized pump, p=0.01, and normalized complex modulation amplitude set (0.30, 0.20). (b) Axial cross-section of the intensity. (c) Evolution of the on-axis intensity.

4.5.4 Summary

We propose a novel class of lasers with a PT-axisymmetric potential to regularize the output field and achieve narrow and bright output beams. The directional coupling given by the PT-symmetry allows to concentrate the emitted laser energy in a narrow and bright output beam. In such lasers, the maximum output intensity, typically limited by saturation can be lifted by applying two different approaches, i.e. averaged pump below the threshold and a central linear defect. These approaches avoid saturation and allow an extraordinary field concentration and enhancement on axis. The dependence of output beam intensity on amplitudes of refractive index and gain-loss modulation and width of the central defect is analyzed. We essentially identify two distinct operating regimes, i.e. stationary and oscillatory regimes. Our proposal, based on the PT-axisymmetric geometry, is generic in nature and could be applied to other broad aperture lasers or amplifiers for the regularization of the spatial structure of the output radiation.

4.6 Conclusions

The emerging field of non-Hermitian photonics opens many new avenues for developing novel photonics devices through the interplay between gain-loss and refractive index. In this Chapter, we explore the improvement of the spatial quality of output beams and propose new photonic configurations.

First, we propose novel configurations of 2D PT-symmetric lattices to manage both spatial dispersion and obtain self-collimated beams. We analyze the symmetric and asymmetric energy distributions controlled by transverse-longitudinal PT-symmetry while maintaining self-collimation phenomenon. The coupled mode expansion is used to analytically

determine non-diffusive and non-diffractive conditions PhC-like and GLM-like cases, afterward confirmed by numerical integration.

Second, we propose novel approaches to improve the spatial quality of laser beams. We demonstrate the modulation instabilities suppression in BAS amplifiers, even for strong nonlinearities, by simultaneous 2D periodic modulations of pump and refractive index. The best stabilization occurs around resonance Q=1, as expected. The laser stability is analyzed with a modified Floquet method to identify suitable parameter sets and with direct numerical integration of the BAS model. We also propose a novel flat mirror VECSEL design stabilized by modifying the system dispersion using spatiotemporal modulations of pump profile. We analyze the flat mirror VECSEL in three operating regimes: intermediate, Class-B and Class-A, corresponding to cavity length ranging from μm to mm. The stability region shrinks for very short cavities. Finally, we suggest a new class of PT-axisymmetric lasers to concentrate the light generated in the entire transverse area of the laser in a narrow beam at central axis. A simplified laser model based on the Complex Ginzburg-Landau equation, allows us to analyze two different strategies, i.e. a central linear defect and averaged pump below the threshold. We observe a significant enhancement in the output intensity in such lasers as compared to the laser pump. We explore the 1D and 2D system with the central defect and identify stationary and oscillatory regimes.

Chapter 5
Conclusions and Future Perspectives

Controlling the flow of electromagnetic fields has been the subject of intensive research since last two decades. In this regard, a variety of new methods have been proposed, ranging from flat optics, transformation optics, and conformal mapping to recent realizations of PT-symmetry in optics. PT-symmetric systems provide unexpected features as unidirectional flow, deriving from the asymmetric mode coupling near the exceptional point. Presently, the more general field of non-Hermitian photonics is attracting a significant attention being a field of intense investigation. And this is precisely the field of my research work, where I expect to have contributed. In particular, I have explored the dynamics of such systems, uncovering different interesting spatial effects and proposing potential technological applications in photonic devices. In this chapter, I briefly summarize the main results presented in the thesis and possible future research perspectives.

In the introductory chapter, we overview the fundamental concept of PT-symmetry, initially proposed for non-Hermitian hamiltonians in Quantum Mechanics, and explain how it can be translated into photonics combining

index and gain-loss profiles. Indeed, the analogies between the Schrödinger equation and Helmholtz equation makes optical systems ideal classic analogs for the realization of PT-symmetry. We present the theoretical foundation for wave and beam propagation in periodic PT-symmetric systems, Photonics Crystals (PhCs) to Gain-loss Modulated (GLM) systems. PhCs and GLM systems may be, in fact, regarded as particular extreme cases of PT-symmetry. We describe the mathematical methods used throughout the thesis: Plane Wave Expansion and Coupled Mode Expansion to determine material dispersions and mode coupling, and paraxial approximation for numerical beam propagation simulations.

In Chapter 2, we propose the novel concept of local PT-symmetry for simultaneous field localization and enhancement at a selected point in the spatial domain. The proposed field localization in the local PT-symmetric scheme is conceptually different from conventional localization mechanisms relying on classical index guiding, gain guiding, the presence of defect modes or Anderson localization in and disordered media. In PT-axisymmetric configurations, the inward mode coupling leads to the field localization and enhancement. For a 1D configuration, formed by two symmetric domains holding local PT-symmetry, we perform a comprehensive analysis for such localization depending on three main parameters: gain-loss, and index modulation amplitudes and the relative phase between the two domains. We find regimes of simultaneous localization and enhancement when both index and gain-loss modulations are balanced, and the coupling becomes strongly unidirectional. Besides, we observe that the phase between the two PT-symmetric domains plays a critical role in the localization effect. We show that such PT-symmetric systems may be regarded as belonging to two extreme situations, that is to say as PhC-like and GLM-like systems. The localization regimes can be

characterized by spatial mode competition. We essentially identify three set of spatial modes participating in the different localization regimes: $k_x = 0, \pm 1, \pm 2, \ldots$ correspond to a PhC-like coupling and $k_x \approx \pm 0.3, \pm 0.7, \pm 1.7, \ldots$ and $k_x \approx \pm 0.5, \pm 1.5, \pm 2.5 \ldots$ to a GLM-like case. In PhC-like systems, less significant localization is observed while in GLM-like case, localization is stronger due to inward mode coupling. We further apply the idea of local PT-symmetry to 2D PT-axisymmetric geometries in which the radially incoming waves drive the field to localize at the center, $r = 0$. We would like to highlight that localization in PT-axisymmetric systems is robust against noise and also a generic effect which can be implemented in other complex profiles (not necessarily periodic) holding PT-axisymmetry. Indeed, we show that localization based on inward mode coupling can be observed in quasi-periodic systems with global PT-symmetry.

In Chapter 3, we extend and generalize the idea of local PT-symmetry to generate directionality fields from arbitrary vector fields, an elegant, flexible and robust way to control the field flow in higher dimensional systems. To achieve this, we derive a new mathematical tool, referred as local Hilbert transform, which relates the two quadratures (real and imaginary parts) of the spatial distribution of the refractive index. The main difference from the conventional Hilbert transform is the introduction of a directional vector field. The potentials build from this local Hilbert transform are expected to determine the flow of light following the vector field. For the confirmation of our theory, we study basic directionality fields in the form of a sink, a vortex, and a circular channel flow, with different initial background patterns. In particular, we consider 2D periodic, quasiperiodic, random and generalized Bessel beam patterns to generate the desired directionality fields. The theoretical predictions are further confirmed by numerical simulations of the temporal evolution of a probe

field in paraxial approximation (equivalent to a propagation through a potential with the proposed transverse profile). Besides, we also show the functionality of the scheme for in-plane propagation by integrating the full set of Maxwell equations using finite difference time domain method. In all cases, the field flow control works irrespective of the initial conditions of the probe field. Besides, we show that such directionality fields are also possible to realize with purely lossy media which increase the feasibility for practical implementations.

In Chapter 4, we propose different realizations of non-Hermitian structures for direct application to novel photonic technologies. In the first part, we show how PT-symmetric lattices can manage the diffraction of light beams. We propose three different configurations to obtain narrow and self-collimated beams. The idea is based on the ability of periodic distributions of the refractive index to tailor the dispersion, and therefore the inter-coupling between propagating modes. In such lattices, PT-symmetry is explored in the transverse, longitudinal and simultaneously in both directions, and analytically determine the non-diffractive and non-diffusive conditions. The characteristics of the spatial modulation required for the suppression of diffraction are analytically explored, ranging from the pure PhC limit to the pure GLMM limit. We observe that self-collimation appears only in PhC-like systems while intrinsic diffusion always persists in GLM-like systems. We also numerically confirm the self-collimation predictions for PT-symmetric systems, with the paraxial propagation model. We would like to highlight that the most interesting cases correspond to the transverse and longitudinal PT-symmetric configurations. We also analyze the mode dynamics in these systems. We observe that the symmetric and asymmetric coupling in self-collimated beams may open the way to control the energy distribution among spatial modes by PT-

symmetric potentials. The results hint that the predicted self-collimation effect may be useful to shape the beam profile in PT-symmetric integrated optics.

In the second part of Chapter 4, we investigate the application of non-Hermitian structures for actual photonic devices. The fundamental concept may be easily implemented to find remarkable applications in various linear and nonlinear optoelectronic devices where a high degree of localization is essentially desirable such as optical switching in nanostructures, optical modulators, or broad aperture lasers and microlasers. In particular, we show a possible direct application for In particular, we focus on Broad Area Semiconductor (BAS) amplifiers, Vertical External Cavity Surface Emitting Lasers (VECSELs) and Vertical Cavity Surface Emitting Lasers (VCSELs), suitable even for highly nonlinear regimes. The scheme relies on a simultaneous 2D spatial modulation of the pump and refractive index profiles. The interplay of the gain-loss and index modulations eventually suppresses the pattern forming instabilities. Such stabilization occurs through a resonant mechanism of the transverse and longitudinal spatial periods of both periodic modulations. We convincingly demonstrate the phenomenon by a semi-analytically Floquet stability analysis, which is further confirmed by direct numerical integration. In addition, the proposed configuration is generic and opens the door for its application to other kinds of broad aperture lasers also suffering from a poor spatial quality of the emitted beam — as, for example, VCSELs. We would like to highlight that simultaneous index and pump modulations in such devices provide a more powerful stabilization scheme, as compared to only pump modulation. The proposal could be implemented with actual nanofabrication techniques, being moreover compact, contrary to other suggested approaches to improve the emission from such sources.

We also propose a robust and compact design of a stable VECSEL, to overcome chaotic spatiotemporal dynamics, deriving from modulation instability. Moreover, the scheme uses a flat mirror output coupler instead of the conventional less robust configuration with a spherical mirror, to ensure high output power with a small cavity. We demonstrate that the introduction of a spatiotemporal modulation of the pump profile may suppress the modulation instability. Full stabilization is possible depending on the amplitude, spatial and temporal frequencies of the pump modulation. Complete and partial stabilization are explored for VECSELs operating in different laser regimes, depending the on external cavity length. Thus, we analyze the stability performance for intermediate, Class-A and Class-B regimes. The proposed method can effectively stabilize VECSELs with cavity lengths ranging from millimeters to centimetres. For a practical implementation, the most interesting situation is found to be a spatiotemporal modulated laser operating at the intermediate regime, with millimetre-long cavities.

Finally, we propose another actual direct implementation of PT-axisymmetry to laser systems, referred as PT-axisymmetric semiconductor lasers. We show that such PT-axisymmetric configuration may render VCSELs into bright and narrow laser beams. The effect is demonstrated on a Complex Ginzburg Landau equation (CGLE), as a mathematical model to study the dynamics of such lasers. Typically, the system displays a turbulent behavior above threshold, due to intrinsic intensity saturation at the center which restricts the maximum output intensity; which may be solved in low pump operation regimes, or alternatively introducing a central linear defect. The numerical results show that the field intensity localized at the central part of the laser is enhanced significantly as compared to the saturated laser pump, in stationary and pulsed regimes. We note the

universality of this nonlinear example as based on a general complex Ginzburg-Landau equation, which confirms that the field localization and concentration at the symmetry center may be realized in other different physical systems as Bose-Einstein condensates and acoustics, among others.

Future Work and Perspectives

Probably the most fascinating aspect of human knowledge is its never-ending intrinsic nature. The work presented in this thesis aims at providing a step towards the understanding of the dynamics of non-Hermitian systems and expects to open new directions in possible implementations. Therefore, the direct future perspectives of this thesis fall in the general area of non-Hermitian theory and its applications to real physical systems. Most physical systems in nature are non-Hermitian, due to the dissipation of energy. Non-Hermitian theory has far-reaching applications to physics; ranging from optics, acoustics, Bose-Einstein Condensates, plasmonics or among others.

In this thesis, we propose novel physical ideas to manipulate the fields flow in local PT-symmetric systems, which we expect to have technological relevance. While, the basic concept of PT-axisymmetric lasers is promoted in this thesis, analysis with more realistic and exhaustive laser models may be required. The study should also involve different 2D geometries, ranging from a simple harmonic, periodic to any arbitrarily-shaped profiles. Furthermore, the proposed structure could be optimized using full-wave simulations employing 3D FDTD numerical simulations, envisaging experimental benefits. The successful experimental demonstration of such PT-axisymmetric VCSELs could represent significant contribution to laser technology, increasing the functionality for future nano-optical devices.

Besides, in the thesis we mainly study the field localization effect considering PT-axisymmetry only in the traverse direction. Therefore, a straightforward future generalization is to explore new configurations of non-Hermitian potentials in which the PT-symmetry holds both in the transverse and longitudinal directions. The study of such potentials for light localization may open new opportunities due to different possible couplings between transverse and longitudinal spatial modes. This idea could have a direct application to improve the beam structure of BALs. Aiming to improve the beam quality of BALs, a large variety of such non-Hermitian 3D geometries could be realized, to obtain clean and focused output beams.

Finally, during my stay at European Laboratory for Non-linear Spectroscopy (LENS), I gained experience to deal with random media. The exotic idea of directionality fields may lead to many extensions, generalization, and applications in real physical systems. In particular, an interesting possibility would be exploring non-Hermitian media in random structures for the control of the flow of electromagnetic fields. The idea is to incorporate randomness in the non-Hermitian systems through different kinds of disorder (Gaussian, short-range, hyper-uniform, etc.) and investigate the localization effect varying the strength of disorder. Besides, the local Hilbert transform can also be used to engineer random non-Hermitian structures for different applications. Moreover, necklace states may be explored in such systems to open transmission channels.

Lastly, directionality fields could be flexibly designed for any desired operating wavelength range. For instance, being generalized to Multicolour Hilbert transforms, i.e. engineering simultaneous directionality fields effective at frequency ranges.

In conclusion, I expect the present thesis directly lead or represent a motivation for future new prospects in the control of light flow by non-Hermitian systems, with different actual technological applications.

Bibliography

[Ahm01] Ahmed, Z. Energy band structure due to a complex, periodic. PT invariant potential. *Phys. Lett. A* **286**, 231 (2001).

[Ada93] Adachihara, H., Hess, O., Abraham, E., Ru, P. and Moloney, J. V. Spatiotemporal chaos in broad-area semiconductor lasers. *J. Opt. Soc. Am. B* **10**, 658 (1993).

[Agr84] Agrawal, G. P. Fast Fourier transform based beam propagation model for stripe geometry semiconductor lasers: Inclusion of axial effects. *J. Appl. Phys*. **56**, 3100 (1984).

[Agu08] D'Aguanno, G., Mattiucci, N. and Bloemer, M. J. Influence of losses on the superresolution performances of an impedance-matched negative-index material, *J. Opt. Soc. Am. B* **25**, 236 (2008).

[Bab08] Baba, T. Slow light in photonic crystals. *Nat. Photon*. **2**, 465 (2008).

[Bag01] Bagchi, B., Quesne, C. and Znojil, M. Generalized continuity equation and modified normalization in PT-symmetric quantum mechanics. *Mod. Phys. Lett. A* **16**, 2047 (2001).

[Ban04] Bandres, M. A., Gutiérrez-Vega, J. C. and Chávez-Cerda, S. Parabolic nondiffracting optical wave fields. *Opt. Lett*. **29**, 44 (2004).

[Ben98] Bender, C. M. and Boettcher, S. Real spectra in non-hermitian hamiltonians having PT symmetry. *Phys. Rev. Lett*. **80**, 5243 (1998).

[Ben99] Bender, C. M., Boettcher, S. and Meisinger P. N. PT-symmetric quantum mechanics. *J. Math. Phys*. **40**, 2201 (1999).

[Ben02] Bender, C. M., Brody D. C. and Jones H. F. Complex extension of quantum mechanics. *Phys. Rev. Lett*. **89**, 270401 (2002).

[Ben05] Bender, C. M. Introduction to PT-symmetric quantum theory. *Contemp. Phys*. **46**, 277 (2005).

[Ben07] Bender C. M. Making sense of non-Hermitian Hamiltonians. *Reports Prog. Phys*. **70**, 947 (2007).

[Ben13] Bender, C. M., Berntson, B. K., Parker, D. and Samuel, E. Observation of PT phase transition in a simple mechanical system. *Am. J. Phys.* **81**, 173 (2013).

[Ben10] Bendix, O., Fleischmann, R., Kottos, T. and Shapiro, B. Optical structures with local PT –symmetry. *J. Phys. A: Math. Theor*. **43**, 265305 (2010).

[Ben11] Benisty, H., Degiron, A., Lupu, A., Lustrac, A. D., Forget, S., Besbes, M., Barbillon, G., Bruyant, A., Blaize, S. and Lerondel, G. Implementation of PT symmetric devices using plasmonics: Principle and applications. *Opt. Express* **19**, 3567 (2011).

[Ben15a] Bender, N., Ramezani, H. and Kottos, T. Engineering wavefront caustics trajectories in PT -symmetric lattices. *Opt. Lett*. **40**, 2138 (2015).

[Ben15b] Bender, N., Li, H., Ellis, F.M. and Kottos, T. Wave-packet self-imaging and giant recombinations via stable Bloch-Zener oscillations in photonic lattices with local PT symmetry. *Phys. Rev. A* **92**, 041803 (2015).

[Bit12] Bittner, S., Dietz, B., Gunther, U., Harney, H. L., Miski-Oglu, M., Richter, A. and Schafer, F. PT symmetry and spontaneous symmetry breaking in a microwave billiard. *Phys. Rev. Lett*. **108**, 024101 (2012).

[Bot10] Botey, M., Herrero, R. and Staliunas. K. Light in materials with periodic gain-loss modulation on a wavelength scale. *Phy. Rev. A* **82**, 013828 (2010).

[Cer16] Cerjan, A., Raman, A. and Fan, S. Exceptional contours and band structure design in parity-time symmetric photonic crystals. *Phys. Rev. Lett*. **116**, 203902 (2016).

[Cha14] Chang, L., Jiang, X., Hua, S., Yang, C., Wen, J., Jiang, L., Li, G., Wang, G. and Xiao, M. Parity time symmetry and variable optical isolation in active passive-coupled microresonators, *Nat. Photon.* **8**, 524 (2014).

[Che08] Chen, F., Gindre, D. and Nunzi, J. M. Tunable circularly polarized lasing emission in reflection distributed feedback dye lasers. *Opt. Express* **16**, 16746 (2008).

[Che10] Chen, H. Y., Chen, C.T. and Sheng, P. Transformation optics and metamaterials. *Nat. Mater*. **9**, 387 (2010).

[Chi03] Chigrin, D., Enoch, S., Torres, S. M. C. and Tayeb, G. Self-guiding in two-dimensional photonic crystals, *Opt. Express* **11**, 1203 (2003).

[Cho10] Chong, Y. D., Ge, L., Cao, H. and Stone, A. D. Coherent perfect absorbers: Time-reversed lasers. *Phys. Rev. Lett*. **105**, 053901 (2010).

[Cho11] Chong, Y. D., Ge, L. and Stone, A. D. PT-symmetry breaking and laser-absorber modes in optical scattering systems. *Phys. Rev. Lett*. **106**, 093902 (2011).

[Cou89] Coullet, P., Gil, L., and Rocca, F. Optical vortices. *Opt. Commun*. **73**, 403 (1989).

[Cro93] Cross, M. C. and Hohenberg, P. C. Pattern formation outside of equilibrium. *Rev. Mod. Phys.* **65**, 851 (1993).

[Cub03] Cubukcu, E., Aydin, K., Ozbay, E., Foteinopoulou, S. and Soukoulis, C. M. Negative refraction by photonic crystals. *Nature* **423**, 604-5 (2003).

[Dav00] Davis, J.A., McNamara, D. E., Cottrell, D. M. and Campos, J. Image processing with the radial Hilbert transform: theory and experiments. *Opt. Lett*. **25**, 99 (2000).

[Den10] Deng, H., Haug, H. and Yamamoto, Y. Exciton-polariton Bose-Einstein condensation. *Rev. Mod. Phys*. **82**, 1489 (2010).

[DeT97] DeTienne, D. H., Gray, G. R., Agrawal, G. P. and Lenstra, D. Semiconductor laser dynamics for feedback from a finite-penetration-depth phase-conjugated mirror. *IEEE J. Quantum Electron*. **33**, 838 (1997).

[Dur87] Durnin, J., Miceli, J. J. and Eberly, J. H. Diffraction-free beams. *Phys. Rev. Lett*. **58**, 1499 (1987).

[Esp07] Espinosa, V., Sánchez-Morcillo, V., Staliunas, K., Pérez-Arjona, I. and Redondo, J. Subdiffractive propagation of ultrasound in sonic crystals. *Phys. Rev. B* **76**, 140302(R) (2007).

[Fen13] Feng, L., Xu, Y.-l., Fegadolli, W. S., Lu, M.-h., Oliveira, J. E. B., Almeida, V. R., Chen, Y.-F. and Scherer, A. Experimental demonstration of a unidirectional reflectionless parity-time metamaterial at optical frequencies. *Nat. Mater*. **12**, 108 (2013).

[Fen14] Feng, L., Wong, Z. J., Ma, R.-M., Wang, Y. and Zhang, X. Single-mode laser by parity-time symmetry breaking. *Science* **346**, 972 (2014).

[Fen17] Feng, L., El-Ganainy, R. and Ge, L. Non-Hermitian photonics based on parity–time symmetry, *Nat. Photon*.**11**, 752 (2017).

[Fle15] Fleury, R., Sounas, D. and Alu, A. An invisible acoustic sensor based on parity-time symmetry. *Nat. Commun*. **6**, 5905 (2015).

[Gan07] El-Ganainy, R., Makris, K. G., Christodoulides, D. N. and Musslimani, Z. H. Theory of coupled optical PT-symmetric structures. *Opt. Lett*. **32**, 2632 (2007).

[Gan12] El-Ganainy, R., Makris, K. G. and Christodoulides, D. N. Local PT invariance and supersymmetric parametric oscillators. *Phys. Rev. A* **86**, 033813 (2012).

[Gan18] El-Ganainy, R., Makris, K. G., Khajavikhan, M., Musslimani, Z. H., Rotter, S. and Christodoulides, D. N. Non-Hermitian physics and PT symmetry. *Nat. Phys*. **14,** 11 (2018).

[Gar12] Garanovich, I. L., Longhi, S., Sukhorukov, A. A. and Kivshar, Y. S. Light propagation and localization in modulated photonic lattices and waveguides. *Phys. Rep*. **518**, 1 (2012).

[Ge14] Ge, L. and Stone, A. D. Parity-Time Symmetry Breaking beyond one Dimension: The Role of Degeneracy. *Phys. Rev. X* **4**, 031011 (2014).

[Ger05] Gersen, H., Karle, T. J., Engelen, R. J., Bogaerts, W., Korterik, J. P., Hulst N. F. Van., Krauss T. F. and Kuipers, L. Real-space observation of ultraslow light in photonic crystal waveguides. *Phys Rev. Lett*. **94**, 073903 (2005).

[Gra12] Graefe, E-M. Stationary states of a PT symmetric two-mode Bose-Einstein condensate. *J. Phys. A* **45**, 444015 (2012).

[Guo09] Guo, A., Salamo, G. J., Duchesne, D., Morandotti, R., Volatier-Ravat, M., Aimez, V., Siviloglou, G. A. and Christodoulides, D. N. Observation of PT-Symmetry Breaking in Complex Optical Potentials. *Phys. Rev. Lett*. **103**, 093902 (2009).

[Guo06] Guo Cheng-Shan., Han, Yu-Jing., Xu, Jian-Bo. and Ding, J. Radial Hilbert transform with Laguerre-Gaussian spatial filters. *Opt. Lett*. **31**, 1394 (2006)

[Han96] Hahn, S. C. Hilbert Transforms in Signal Processing, *Boston Anect House*, 1996.

[Has17] Hassan, A. U., Zhen, B., Soljačić, M., Khajavikhan, M. and Christodoulides, D. N. Dynamically Encircling Exceptional Points: Exact Evolution and Polarization State Conversion. *Phys. Rev. Lett.* **118**, 093002 (2017)

[Hay18] Hayran, Z., Herrero, R., Botey, M., Kurt, H. and Staliunas, K. Invisibility on demand based on a generalized Hilbert transform, submitted 2018; https://arxiv.org/abs/1703.09490

[Hei04] Heiss, W. D. Exceptional points of non-Hermitian operators. *J. Phys. A: Math. Gen*. **37**, 2455 (2004).

[Her12] Herrero, R., Botey, M., Radziunas, M. and Staliunas, K. Beam shaping in spatially modulated broad-area semiconductor amplifiers. *Opt. Lett*. **37**, 5253 (2012).

[Her14] Herrero, R., Botey, M. and Staliunas, K. Nondiffractive-nondiffusive beams in complex crystals. *Phys. Rev. A* **89**, 063811 (2014).

[Hes95] Hess, O., Koch, S. W. and Moloney, J. V. Filamentation and beam propagation in broad-area semiconductor lasers. *IEEE J. Quantum Electron*. **31**, 35 (1995).

[Hes96] Hess, O. and Kuhn, T. Spatio-temporal dynamics of semiconductor lasers: Theory, modeling and analysis. *Prog. Quantum Electron*. **20**, 85 (1996).

[Ho93] Ho, K. P., Walker, J. D. and Kahn, J. M. External optical feedback effects on intensity noise of vertical-cavity surface-emitting lasers. *IEEE Photon. Technol. Lett*. **5**, 892 (1993).

[Hod14] Hodaei, H., Miri, M.-A., Heinrich, M., Christodoulides, D. N. and Khajavikhan, M. Parity-time-symmetric microring lasers. *Science* **80**, 346, 975 (2014).

[Hor15] Horsley, S. A. R., Artoni, M. and La Rocca, G. C. Spatial Kramers Kronig relations and the reflection of waves. *Nat. Photon*. **9**, 436 (2015).

[Hor16] Horsley, S. A. R., King, C. G. and Philbin, T. G. J. Wave propagation in complex coordinates. *J. Opt*. **18**, 044016 (2016).

[Hor17] Horsley, S. A. R., and Longhi, S. Spatiotemporal deformations of reflectionless potentials. *Phys. Rev. A* **96**, 023841 (2017).

[Iga88] Iga, K., Koyama, F. and Kinoshita, S. Surface emitting semiconductor lasers. *IEEE J. Quantum Electron*. **24**, 1845 (1988).

[Jia17] Jiang, W., Ma, Y., Yuan, J., Yin, G., Wu, W. and He, S. Deformable broadband metamaterial absorbers engineered with an analytical spatial Kramers-Kronig permittivity profile. *Laser Photon. Rev*. **11**, 1600253 (2017).

[Kin17a] King, C. G., Horsley, S. A. R., and Philbin, T. G. Perfect Transmission through Disordered Media. *Phys. Rev. Lett*. **118**, 163201 (2017).

[Kin17b] King, C. G., Horsley, S. A. R., and Philbin, T. G. Zero reflection and transmission in graded index media. *J. Opt*. **19**, 085603(2017).

[Kla08] Klaiman, S., Günther, U. and Moiseyev, N. Visualization of branch points in PT–symmetric waveguides. *Phys. Rev. Lett*. **101**, 080402 (2008).

[Kog71] Kogelnik, H., and Shank, C. V. Stimulated emission in a periodic structure. *Appl. Phys. Lett*. **18**, 152 (1971).

[Kon16] Konotop,V. V., Yang, J., and Zezyulin,D. A. Nonlinear waves in PT -symmetric systems. *Rev. Mod. Phys*. **88**, 035002 (2016).

[Kos99] Kosaka, H., Kawashima, T., Tomita, A., Notomi, M., Tamamura, T., Sato, T. and Kawakami, S. Self-collimating phenomena in photonic crystals. *Appl. Phys. Lett*. **74**, 1212 (1999)

[Kot10] Kottos, T. Optical physics: Broken symmetry makes light work, *Nat. Phys*. **6**, 166 (2010).

[Kum13] Kumar, N., Botey, M., Herrero, R., and Staliunas, K., Flat lensing by periodic loss-modulated materials. *Opt. Soc. Am. B* **30**, 2684 (2013).

[Kum14] Kumar, S., Herrero, R., Botey, M. and Staliunas, K. Suppression of modulation instability in broad area semiconductor amplifiers. *Opt. Lett*. **39**, 5598 (2014).

[Kum15] Kumar, S., Herrero, R., Botey M. and Staliunas, K. Taming of modulation instability by spatio-temporal modulation of the potential. *Sci. Reports* **5**, 13268 (2015).

[Law98] Law, J. Y. and Agrawal, G. P. Feedback-induced chaos and intensity-noise enhancement in vertical-cavity surface-emitting lasers. *J. Opt. Soc. Am. B* **15**, 562 (1998).

[Lee14] Lee, Y. C., Hsieh, M. H., Flammia, S. T. and Lee, R.-K. Local PT Symmetry Violates The No-Signaling Principle. *Phys. Rev. Lett*. **112**, 130404 (2014).

[Leo06] Leonhardt, U. Optical Conformal Mapping. *Science* **312**, 1777 (2006).

[Li16] Li, J., Yu, R., Ding, C. and Wu, Y. PT-symmetry-induced evolution of sharp asymmetric line shapes and high-sensitivity refractive index sensors in a three cavity array. *Phys. Rev. A*. **93**, 023814 (2016).

[Lie12] Liertzer, M., Ge, Li, Cerjan, A., Stone, A. D., Türeci, H. E., and Rotter, S. Pump-induced exceptional points in lasers. *Phys. Rev. Lett*. **108**, 173901 (2012).

[Lig07] Lignier, H., Sias, C., Ciampini, D., Singh, Y., Zenesini, A., Morsch, O. and Arimondo, E. Dynamical Control of Matter-Wave Tunneling in Periodic Potentials. *Phys. Rev. Lett*. **99**, 220403 (2007).

[Lin11] Lin, Z., Ramezani, H., Eichelkraut, T., Kottos, T., Cao, H. and Christodoulides, D. N. Unidirectional invisibility induced by PT-symmetric periodic structures. *Phys. Rev. Lett*. **106**, 213901 (2011).

[Liu16] Liu, Z.-P. Zhang, J., Ozdemir, S.K., Peng, B., Jing, H., Lü, X.-Y., Li, C.-W., Yang, L., Nori, F. and Liu, Y.-X. Metrology with PT-symmetric cavities: enhanced sensitivity near the PT-phase transition. *Phys. Rev. Lett*. **117**, 110802 (2016).

[Lon06] Longhi, S., Marangoni, M., Lobino, M., Ramponi, R., Laporta, P., Cianci, E. and Foglietti, V. Observation of Dynamic Localization in Periodically Curved Waveguide Arrays. *Phys. Rev. Lett*. **96**, 243901 (2006).

[Lon09] Longhi, S. Bloch oscillations in complex crystals with PT symmetry. *Phys. Rev. Lett*. **103**, 123601 (2009).

[Lon10] Longhi, S. PT-symmetric laser absorber. *Phys. Rev. A* **82**, 031801 (2010).

[Lon15] Longhi, S. Wave reflection in dielectric media obeying spatial Kramers-Kronig relations. *Europhys. Lett*. **112**, 64001 (2015).

[Lon16] Longhi, S. Bidirectional invisibility in Kramers–Kronig optical media. *Opt. Lett*. **41**, 3727 (2016).

[Lu15] Lü, X.-Y., Jing, H., Ma, J.-Y. and Wu, Y. PT-Symmetry-Breaking Chaos in Optomechanics. *Phys. Rev. Lett*. **114**, 253601 (2015).

[Lum13] Lumer, Y., Plotnik, Y., Rechtsman, M. C. and Segev, M. Nonlinearly induced PT-transition in photonic systems. *Phys. Rev. Lett*. **111**, 263901 (2013).

[Lup13] Lupu, A., Benisty, H. and Degiron, A. Switching using PT symmetry in plasmonic systems: positive role of the losses. *Opt. Express* **21**, 21651 (2013).

[Mai10] Maigyte L., Gertus, T., Peckus, M., Trull, J., Cojocaru, C., Sirutkaitis, V. and Staliunas, K. Signatures of light-beam spatial filtering in a three-dimensional photonic crystal. *Phys. Rev. A* **82**, 043819 (2010).

[Mai15] Maigyte, L. and Staliunas, K. Spatial filtering with Photonics crystals, *Appl. Phys. Rev*. **2**, 011102 (2015).

[Mak08] Makris, K. G., El-Ganainy, R., Christodoulides, D. N. and Musslimani, Z. H. Beam Dynamics in PT Symmetric Optical Lattices. *Phys. Rev. Lett*. **10**0, 103904 (2008).

[Mak10] Makris, K. G., El-Ganainy, R., and Christodoulides, D. N. PT-symmetric optical lattices, *Phys. Rev. A* **81**, 063807 (2010).

[Mak11] Makris, K. G., El-Ganainy, R., Christodoulides, D. N. and Musslimani, Z. H. PT-symmetric periodic optical potentials. *Int. J. Theor. Phys*. **50**, 1019 (2011).

[Mak15] Makris, K.G., Musslimani, Z.H., Christodoulides, D.N., and Rotter, S. Constant-intensity waves and their modulation instability in non-Hermitian potentials. *Nat. Commun.* **6**, 7257 (2015).

[Mar96] Marciante, J. R. and Agrawal, G. P. Nonlinear mechanisms of filamentation in broad-area semiconductor lasers. *IEEE J. Quantum Electron.* **32**, 590. (1996).

[Mea91] Meade, R., Brommer, K., Rappe, A. and Joannopoulos, J. Photonic bound states in periodic dielectric materials. *Phys. Rev. B* **44**, 13772 (1991).

[Mor08] Moreno, P. and Ramirez, A., Implementation of the Numerical Laplace Transform: A Review. *IEEE Trans. Power Delivery* **23**, 2599 (2008).

[Mos02] Mostafazadeh, A. Pseudo-Hermiticity for a class of nondiagonalizable Hamiltonians. *J. Math. Phys*. **43**, 6343 (2002).

[Mos03] Mostafazadeh, A. Exact PT-symmetry is equivalent to Hermiticity. *J. Phys. A: Math. Gen.* **36**, 7081 (2003).

[Mos09] Mostafazadeh, A. Spectral singularities of complex scattering potentials and infinite reflection and transmission coefficients at real energies. *Phys. Rev. Lett*. **102**, 220402 (2009).

[Mun97] Munkel, M., Kaiser, F. and Hess, O. Stabilization of spatiotemporally chaotic semiconductor laser arrays by means of delayed optical feedback. *Phys. Rev. E* **56**, 3868 (1997).

[Mus08] Musslimani, Z., Makris, K., El-Ganainy, R. and Christodoulides, D. N. Optical solitons in PT periodic potentials. *Phys. Rev. Lett*. **100**, 030402 (2008).

[Ngu16] Nguyen, B. P. and Kim, K. Transport and localization of waves in ladder-shaped lattices with locally PT-symmetric potentials. *Phys. Rev. A* **94**, 062122 (2016).

[Not10] Notomi, M. Manipulating light with strongly modulated photonic crystals. *Reports Prog. Phys.* **73**, 096501 (2010).

[Oht12] Ohtsubo, J. Semiconductor lasers: stability, instability and chaos *Springer* (2012).

[Opp91] Oppo, G. L., D'Alessandro, G. and Firth, W. J. Spatiotemporal instabilities of lasers in models reduced via center manifold techniques. *Phys. Rev. A* **44**, 4712 (1991).

[Opp09] Oppo, G. L., Yao, A. M., Prati, F. and De Valcárcel, G. J. Long-term spatiotemporal dynamics of solid-state lasers and vertical-cavity surface-emitting lasers. *Phys. Rev. A* **79**, 033824 (2009).

[Oto14] Fernandez-Oto, C., de Valcárcel, G. J., Tlidi, M., Panajotov, K. and Staliunas, K. Phase-bistable patterns and cavity solitons induced by spatially periodic injection into vertical-cavity surface-emitting lasers. *Phys. Rev. A* **89**, 055802 (2014).

[Pak17] Pakhomov, A. V., Arkhipov, R. M. and Molevich, N. E. Stabilization of class-B broad-area laser emission by external optical injection. *J. Opt. Soc. Am. B* **34**, 756 (2017).

[Par03] Parimi, P. V., Lu W. T., Vodo, P. and Sridhar, S. Photonic crystals: imaging by flat lens using negative refraction. *Nature* **426**, 6965, (2003).

[Pen06] Pendry, J. B., Schurig, D. and Smith, D. R. Controlling Electromagnetic Fields. *Science* **312**, 1780 (2006).

[Pen14a] Peng, B., Ozdemir, S. K., Rotter, S., Yilmaz, H., Liertzer, M., Moni, F., Bender, C. M., Nori, F. and Yang, L. Loss-induced suppression and revival of lasing. *Science* **346**, 328 (2014).

[Pen14b] Peng, B., Ozdemir, S. K., Lei, F., Moni, F., Gianfreda, M., Long, G. L., Fan, S., Nori, F., Bender, C. M. and Yang, L. Parity time-symmetric whispering-gallery microcavities. *Nat. Phys*. **10**, 394 (2014).

[Pen16] Peng, B., Ozdemir, S. K., Liertzer, M., Chen, W., Kramer, J., Yılmaz, H., Wiersig, J., Rotter, S. and Yang, L. Chiral modes and directional lasing at exceptional points. *Proc Natl Acad Sci*. **113**, 6845 (2016).

[Per07] Pérez-Arjona, I., Redondo, F., Sánchez-Morcillo, V. J., Espinosa, V. and Staliunas, K. Theoretical prediction of the nondiffractive propagation of sonic waves through periodic acoustic media. *Phys. Rev. B* **75**, 014304 (2007).

[Po111] Pollès, R., Centeno, E., Arlandis, Ju. and Moreau, A. Self-collimation and focusing effects in zero-average index metamaterials. *Opt. Express* **19**, 6149 (2011).

[Pra07a] Prather, D. W., Shi, S., Murakowsk, J., Schneider, G. J., Sharkawy, A., Chen, C., Miao, B. and Martin, R. Self-collimation in photonic crystal structures: a new paradigm for applications and device development. *J. Phys. D* **40**, 2635 (2007).

[Pra07b] Prati, F. and Columbo, L. Long-wavelength instability in broad-area semiconductor lasers. *Phys. Rev. A* **75**, 053811(2007).

[Rad13] Radziunas, M., Botey, M., Herrero, R., and Staliunas, K. Intrinsic beam shaping mechanism in spatially modulated broad area semiconductor amplifiers. *Appl. Phys. Lett.* **103**, 132101. (2013).

[Ram10] Ramezani, H., Kottos, T., El-Ganainy, R. and Christodoulides, D. N. Unidirectional nonlinear PT-symmetric optical structures. *Phys. Rev. A* **82**, 043803 (2010).

[Ram12a] Ramezani, H., Christodoulides, D. N., Kovanis, V., Vitebskiy, I. and Kottos, T. PT-symmetric Talbot effect. *Phys. Rev. Lett*. **109**, 033902 (2012).

[Ram12b] Ramezani, H., Kottos, T., Kovanis. V. and Christodoulides, D. N. Exceptional-point dynamics in photonic honeycomb lattices with PT symmetry. *Phys. Rev. A* **85**, 013818 (2012).

[Ram14] Ramezani, H., Li, H.-K., Wang, Y. and Zhang, X. Unidirectional spectral singularities. Phys. Rev. Lett. 113, 263905 (2014)

[Reg96] Martin-Regalado, J., Van Tartwijk, G. H. M., Balle, S. and San Miguel, M. Mode control and pattern stabilization in broad-area lasers by optical feedback. *Phys. Rev. A* **54**, 5386 (1996).

[Reg12] Regensburger, A., Bersch, C., Miri, M.-A., Onishchukov, G., Christodoulides, D. N. and Peschel, U. Parity-time synthetic photonic lattices. *Nature* **488**, 167 (2012).

[Reg13] Regensburger, A., Miri, M.-A., Bersch, C., Nager, J., Onishchukov, G., Christodoulides, D. N. and Peschel, U. Observation of defect states in PT-symmetric optical lattices. *Phys. Rev. Lett*. **110**, 223902 (2013).

[Rut10] Ruter, C. E., Makris, K. G., El-Ganainy, R. Christodoulides, D. N., Segev, M. and Kip, D. Observation of parity time symmetry in optics. *Nat. Phys*. **6**, 192 (2010).

[Sal85] Salzman, J., Venkatesan, T., Lang, R., Mittelstein, M. and Yariv, A. Unstable resonator cavity semiconductor lasers. *Appl. Phys. Lett*. **46**, 218–220 (1985).

[Sav14] Savoia, S., Castaldi, G., Galdi, V. Tunneling of obliquely incident waves through PT-symmetric epsilon-near-zero bilayers. *Phys. Rev. B* **89**, 085105 (2014).

[Sch11] Schindler, J., Li, A., Zheng, M. C., Ellis, F. M. and Kottos, T. Experimental study of active LRC circuits with PT symmetries. *Phys. Rev. A* **84**, 040101 (2011).

[Sch12] Schindler, J., Lin, Z., Lee, J. M., Ramezani, H., Ellis, F. M. and Kottos, T. PT-symmetric electronics. *J. Phys. A Math. Theor*. **45**, 444029 (2012).

[Ser09] Serebryannikov, A. E., Petrov, A. Y. and Ozbay, E. Toward photonic crystal based spatial filters with wide angle ranges of total transmission. *Appl. Phys. Lett*. **94**, 26 (2009).

[Sha12] Shan, G., Zhao, X., Hu, M., Shek, C. H. and Huang, W. Vertical-external-cavity surface-emitting lasers and quantum dot lasers. *Front. Optoelectron*. **5**, 157 (2012).

[Sie91] Siegman, A. E., Sasnett, M. W. and Johnston, T. F. Choice of clip levels for beam width measurements using knife-edge techniques. *IEEE J. Quantum Electron*. 27, 1098 (1991).

[Spi98] Spinelli, L., Tissoni, G., Brambilla, M., Prati, F. and Lugiato, L. A. Spatial solitons in semiconductor microcavities. *Phys. Rev. A* **58**, 2542 (1998).

[Suk10] Sukhorukov, A. A., Xu, Z. Y. and Kivshar, Y. S. Nonlinear suppression of time reversals in PT-symmetric optical couplers. *Phys. Rev. A* **82**, 043818 (2010).

[Sta03] Staliunas, K. and Sanchez-Morcillo, V. J. Transverse patterns in nonlinear optical resonators (Vol. 183). *Springer* (2003).

[Sta06a] Staliunas, K. and Herrero, R. Nondiffractive propagation of light in photonic crystals. *Phys. Rev. E* **73**, 016601 (2006).

[Sta06b] Staliunas, K., Herrero, R. and de Valcarcel, G. J. Subdiffractive band-edge solitons in Bose-Einstein condensates in periodic potentials. *Phys. Rev. E* **73**, 065603(R) (2006).

[Sta09] Staliunas, K., Herrero, R., and Vilaseca, R. Subdiffraction and spatial filtering due to periodic spatial modulation of the gain-loss profile. *Phys. Rev. A* **80**, 013821 (2009).

[Taf05] Taflove, A. and Hagness, S. C. Computational Electrodynamics: The Finite-Difference Time-Domain Method. Artech House, Incorporated, 2005.

[Tar98] Van Tartwijk, G. H. and Agrawal, G. P. Laser instabilities: a modern perspective. *Prog. Quantum Electron*. **22**, 43 (1998).

[Tur15] Turduev, M., Botey, M., Giden, I., Herrero, R., Kurt, H., Obzay, E. and Staliunas, K. Two-dimensional complex parity-time-symmetric photonic structures. *Phys. Rev. A* **91**, 023825 (2015).

[Tro06] Tropper, A. C. and Hoogland, S. Extended cavity surface-emitting semiconductor lasers. *Prog. Quantum Electron*. **30**, 1. (2006).

[Uch12] Uchida, A. Optical Communication with Chaotic Lasers: Applications of Nonlinear Dynamics and Synchronization. *John Wiley & Sons* (2012).

[Veg00] Gutiérrez-Vega, J. C., Iturbe-Castillo, M. D. and Chávez-Cerda, S. Alternative formulation for invariant optical fields: Mathieu beams, *Opt. Lett*. **25**, 1493 (2000).

[Vys14] Vysloukh, V. A., and Kartashov, Y. V. Resonant mode conversion in the waveguides with unbroken and broken PT-symmetry. *Opt. Lett*. **39**, 5933 (2014).

[Wei03] S. Weigert, Completeness and orthonormality in PT-symmetric quantum systems. *Phys. Rev. A* **68**, 062111 (2003).

[Wes10] West, C. T., Kottos, T. and Prosen, T. PT-symmetric wave chaos. *Phys. Rev. Lett*. **104**, 054102 (2010).

[Wim15] Wimmer, M., Regensburger, A., Miri, M.-A., Bersch, C., Christodoulides, D. N. and Peschel, U. Observation of optical solitons in PT-symmetric lattices. *Nat. Commun*. **6**, 7782 (2015).

[Wit02] Witzens, J., Lonacar, M. and Scherer, A. Self-collimation in planar photonic crystals. *IEEE J. Sel. Top. Quantum Electron*. **8**, 1246 (2002).

[Wol99] Wolff, S. Messerschmidt, D. and Fouckhardt, H. Fourier-optical selection of transverse modes in broad area lasers. *Opt. Express* **5**, 32 (1999).

[Wol00] Wolff, S. and Fouckhardt, H. Intracavity stabilization of broad area lasers by structured delayed optical feedback. *Opt. Express* **7,** 222-227 (2000).

[Xu16] Xu, H., Mason, D., Jiang, L. and Harris J. G. E. Topological energy transfer in an optomechanical system with exceptional points. *Nature*. **80**, 537, (2016).

[Yab91] Yablonovitch, E., Gmitter, T. J., Meade, R. D., Rappe, A. M., Brommer, K. D. and Joannopoulos, J. D. Donor and acceptor modes in photonic band structure. *Phys. Rev. Lett*. **67**, 3380 (1991).

[Yin13] Yin, X. and Zhang, X. Unidirectional light propagation at exceptional points. *Nat. Mater*. **12**, 175 (2013).

[Zen87] Zengerle, R. Light Propagation in Singly and Doubly Periodic Planar Waveguides. *J. Mod. Opt*. **34**, 1589 (1987).

[Zhu14] Zhu, X., Ramezani, H., Shi, C., Zhu, J. and Zhang, X. PT-Symmetric Acoustics. *Phys. Rev. X* **4**, 031042 (2014).

[Zhu15] Xu, L. and Chen, H. Conformal transformation optics. *Nature Photon*. **9**, 15 (2015).

[Zya14] Zyablovsky, A. A., Vinogradov, A. P., Pukhov, A. A., Dorofeenko, A. V. and Lisyansky, A. A. PT-symmetry in optics. *Phys.-Usp*. **57**, 1063 (2014).

List of Publications

Peer reviewed journal articles:

[J1] **Ahmed, W. W**., Kumar, S., Medina, J., Botey, M., Herrero, R. and Staliunas, K. Stablization of broad area semiconductor laser sources using simultaneous index and pump modulations. under review in *Opt. Lett.* https://arxiv.org/abs/1801.03878

[J2] **Ahmed, W. W.,** Herrero, R., Botey, M., Hayran, Z., Kurt, H. and Staliunas, K. Directionality Fields generated by a Local Hilbert Transform. Accepted in *Phys. Rev. A* (https://arxiv.org/abs/1707.04556)

[J3] **Ahmed, W. W**., Herrero, R., Botey, M. and Staliunas, K. Self-collimation in PT-symmetric crystals. *Phys. Rev. A* 95, 053830 (2017)

[J4] **Ahmed, W. W**., Herrero, R., Botey, M. and Staliunas, K. Locally parity-time-symmetric and globally parity-symmetric systems. *Phys. Rev. A* 94, 053819 (2016).

[J5] **Ahmed, W. W**., Kumar, S., Herrero, R., Botey, M., Radziunas, M. and Staliunas, K. Stabilization of flat-mirror vertical-external-cavity surface-emitting lasers by spatiotemporal modulation of the pump profile. *Phys. Rev. A* 92, 43829 (2015).

Book Chapters:

[B1] Kumar, S., **Ahmed, W. W**., Herrero, R., Botey, M., Radziunas, M. and Staliunas, K. Stabilization of Broad Area Semiconductor Amplifiers by Spatially Modulated Potentials. In Nonlinear Dynamics: Materials, Theory and Experiments (pp. 139-151). Springer International Publishing (2016).

Conference Proceedings:

[C1] Ahmed W. W., Herrero, R., Botey, M., Hayran, Z., Kurt, H. and Staliunas, K. PT-vector Fields, SPIE Photonics Europe: Strasbourg, France (accepted). To be presented in 22-26 April (2018).

[C2] **Ahmed, W. W**., Botey, M., Herrero, R. and Staliunas, K. Self-collimated beams in 2D complex periodic lattices from P- to PT-symmetry, 11th International Congress on Engineered Materials Platforms for Novel Wave Phenomena (Metamaterials): Marseille, France, 28-31 Aug 2017 (Oral Presentation).

[C3] **Ahmed, W. W**., Herrero, R., Botey, M. and Staliunas, K. PT-axisymmetric VCSELs with linear central defect. 18th International Conference on Transparent Optical Networks (ICTON 2017): Girona, Spain, 2-6 July 2017 (Invited Talk).

[C4] Botey, M., **Ahmed, W. W**., Herrero, R. and Staliunas, K. PT-axisymmetry for extraordinary field confinement, SPIE OPTO: San Francisco, California, United States, 28 Jan -02 Feb. 2017 (Oral Presentation)

[C5] Kumar, S., **Ahmed, W. W**., Herrero, R., Botey, M. and Staliunas, K. Stabilization of Broad Area Semiconductor lasers. SPIE OPTO: San Francisco, California, United States, 28 Jan -02 Feb. 2017 (Oral Presentation)

[C6] **Ahmed, W.W**., Herrero, R., Botey, M., Radziunas, M. and Staliunas, K. Axisymmetric photonic structures with PT-symmetry. SPIE Nanoscience+

Engineering: San Diego, California, United States, 19 -23 Aug 2016 (Invited Talk).

[C7] **Ahmed, W. W**., Botey, M., Herrero, R. and Staliunas, K. PT-axisymmetric photonic nanostructures. 18th International Conference on Transparent Optical Networks (ICTON 2016): Trento, Italy,10-14 July 2016 (Invited Talk).

[C8] **Ahmed, W. W**., Kumar, S., Herrero, R., Botey, M., Radziunas, M. and Staliunas, K. Suppression of modulation instability in pump modulated flat-mirror VECSELs. SPIE Photonics Europe: Brussels, Belgium, 03-07 Apr 2016 (Oral Presentation).

[C9] Kumar, S., **Ahmed, W. W**., Radziunas, M., Botey, M., Herrero, R., and Staliunas, K. Taming the modulation instability in semiconductor lasers. 17th International Conference on Transparent Optical Networks (ICTON 2015): Budapest, Hungary, 05-09 July 2015 (Invited Talk).

Conferences with Abstracts:

[A1] **Ahmed, W. W**., Botey, M., Herrero, R. and Staliunas, K. PT-axisymmetric VCSELs. Nanophotonics and Micro/Nano Optics International Conference (NANOP): Barcelona, Spain, 12-14 Sept. 2017 (Oral Presentation).

[A2] Botey, M., **Ahmed, W. W**., Herrero, R. and Staliunas, K. Self-collimation in 2D Complex P- and PT-symmetric systems. 8th International conference on Metamaterials, Photonic Crystals and Plasmonics (META'17): Incheon, South Korea, July 2017 (Invited Talk).

[A3] Botey, M., **Ahmed, W. W**., Herrero, R. and Staliunas, K. PT-axisymmetric VCSELs. SPIE Optics + Optoelectronics: Prague, Czech Republic, 24-27 April, 2017 (Invited Talk).

[A4] **Ahmed, W. W**., Botey, M., Herrero, R. and Staliunas, K. Localized field enhancement in PT-axisymmetric systems, 6th International Topical

Meeting on Nanophotonics and Metamaterials (Nanometa): Seefeld (Tirol), Austria, 04-07 Jan. 2017 (Poster Presentation).

[A5] **Ahmed, W. W**., Botey, M., Herrero, R. and Staliunas, K. Field concentration by local PT-symmetry and global P-symmetry. 7th International conference on Metamaterials, Photonic Crystals and Plasmonics (META'16): Malaga, Spain, 25-28 July 2016 (Invited Talk).

Spring Schools Participations:

[S1] Europhotonics Spring School 4th Edition (Paderborn, Germany, 13-16 April, 2015). Spatiotemporal effects in VCSELs (Poster Presentation). http://www.europhotonics.org/wordpress/spring-school

[S2] Europhotonics Spring School 5th Edition (Porquerolles Island, France, 29 March-1 April, 2016). Light localization in PT-axisymmetric systems (Poster Presentation). http://www.europhotonics.org/wordpress/spring-school

[S3] Europhotonics Spring School 6th Edition (Sitges, Barcelona, 22-24 March, 2017). Light Propagation in PT-symmetric potentails (Oral Presentation). http://www.europhotonics.org/wordpress/spring-school